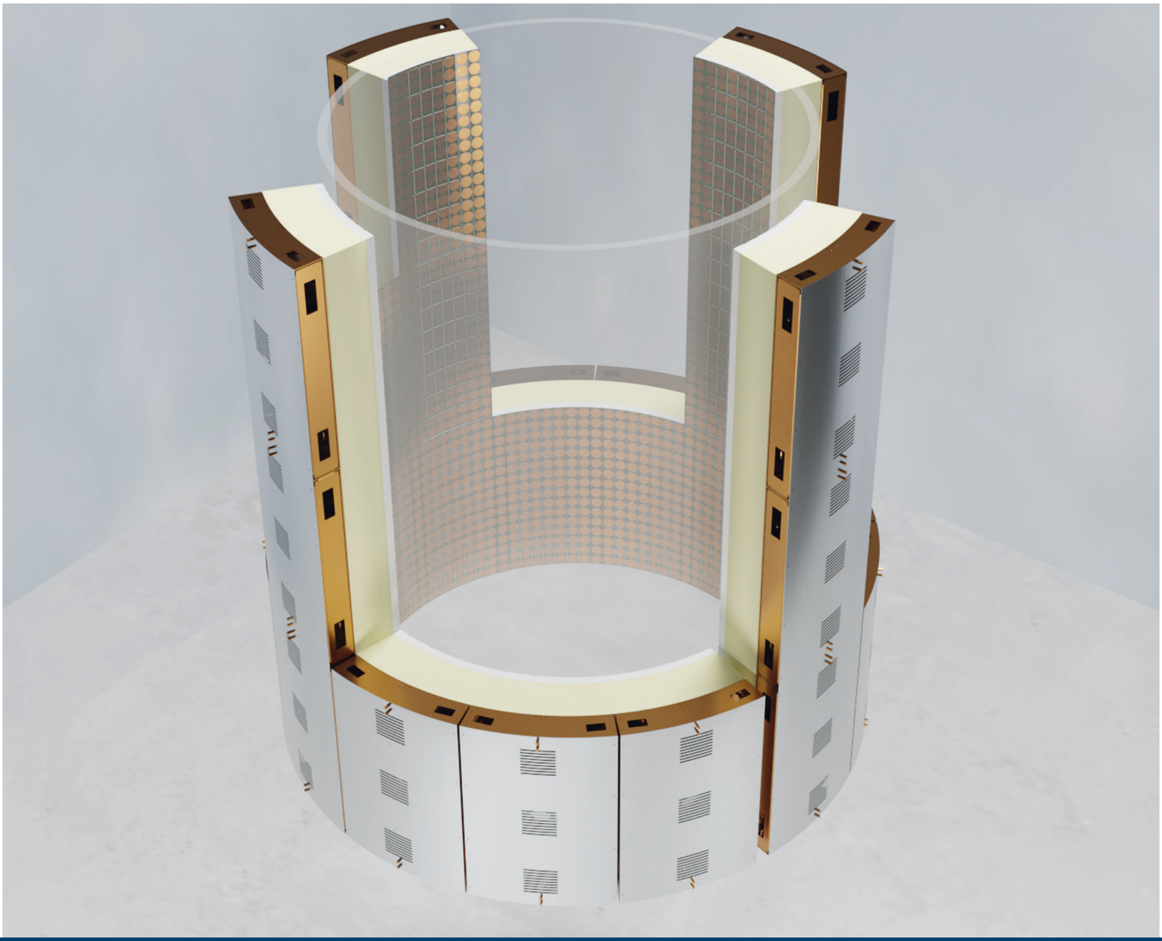

In Situ Time Calibration for Stationary Multichannel GPR Monitoring Systems

Leon Steinbeck

Energie & Umwelt / Energy & Environment
Band / Volume 635
ISBN 978-3-95806-767-7

Mitglied der Helmholtz-Gemeinschaft

JÜLICH
Forschungszentrum

Schriften des Forschungszentrums Jülich
Reihe Energie & Umwelt / Energy & Environment Band / Volume 635

Forschungszentrum Jülich GmbH
Zentralinstitut für Engineering, Elektronik und Analytik (ZEA)
Systeme der Elektronik (ZEA-2)

In Situ Time Calibration for Stationary Multichannel GPR Monitoring Systems

Leon Steinbeck

Schriften des Forschungszentrums Jülich
Reihe Energie & Umwelt / Energy & Environment Band / Volume 635

ISSN 1866-1793 ISBN 978-3-95806-767-7

Bibliografische Information der Deutschen Nationalbibliothek.
Die Deutsche Nationalbibliothek verzeichnet diese Publikation in der Deutschen Nationalbibliografie; detaillierte Bibliografische Daten sind im Internet über http://dnb.d-nb.de abrufbar.

Herausgeber und Vertrieb: Forschungszentrum Jülich GmbH
Zentralbibliothek, Verlag
52425 Jülich
Tel.: +49 2461 61-5368
Fax: +49 2461 61-6103
zb-publikation@fz-juelich.de
www.fz-juelich.de/zb

Umschlaggestaltung: Grafische Medien, Forschungszentrum Jülich GmbH

Druck: Grafische Medien, Forschungszentrum Jülich GmbH

Schriften des Forschungszentrums Jülich
Reihe Energie & Umwelt / Energy & Environment, Band / Volume 635

D 464 (Diss. Duisburg-Essen, Univ., 2023)

ISSN 1866-1793
ISBN 978-3-95806-767-7

Vollständig frei verfügbar über das Publikationsportal des Forschungszentrums Jülich (JuSER) unter www.fz-juelich.de/zb/openaccess.

"Everything must be made as simple as possible. But not simpler."

Albert Einstein

Hiermit versichere ich, die vorliegende Dissertation selbstständig, ohne fremde Hilfe und ohne Benutzung anderer als den angegebenen Quellen angefertigt zu haben. Alle aus fremden Werken direkt oder indirekt übernommenen Stellen sind als solche gekennzeichnet. Die vorliegende Dissertation wurde in keinem anderen Promotionsverfahren eingereicht. Mit dieser Arbeit strebe ich die Erlangung des akademischen Grades Doktor der Ingenieurwissenschaften (Dr.-Ing.) an.

Ort, Datum

Name

Acknowledgments

First and foremost, I'd like to express my sincere gratitude to my supervisor, Prof. Dr. Stefan van Waasen who provided me with the opportunity to work on this thesis at ZEA-2. I also extend my thanks to Prof. Dr. Anja Klotzsche for her willingness to take on the role of the second reviewer.

A special mention goes to my daily mentor, Dr. Achim Mester. We've collaborated closely over the past few years, and I've gained a wealth of knowledge from you. Your open and always supportive approach kept me motivated to drive this work forward. You consistently made me feel comfortable seeking your guidance, especially during challenging times. This work would not have been possible without your invaluable assistance. I'd also like to express my sincere appreciation to Dr. Egon Zimmermann, who seamlessly stepped in during Achim's parental leave and significantly contributed to the successful completion of this thesis.

I want to acknowledge the contributions of my colleagues Ilja Bekman, Christian Roth, Markus Harff, Stefan Heinen, Tom Neubert, and Roger Heil. You provided substantial support throughout my work and were a great source of learning. Thanks to you, I was able to professionally grow during my PhD journey. I'd also like to express my gratitude to Josua Florczak and Martial Tazifor for the enjoyable and enlightening time at the Measurement Systems PhD meetings.

Finally, I'd like to extend my thanks to my fellow office mates from the PhD office. Your positive presence always brightened my workdays. To my friends and family, your unwavering support and belief in me have been a driving force in my career.

Abstract

Advanced and extensive processing of ground penetrating radar (GPR) data, for example needed for full-waveform inversion approaches, requires a reliable temporal calibration of the system. Usually, the calibration of GPR systems is performed with a known medium between transmitting and receiving antennas. Thereby, the observed time difference between expected and measured signal arrival times, termed as time-zero, can be accounted for as a system specific time delay. For measurement configurations where the antennas are permanently positioned around soil samples for monitoring purposes, time-consuming additional measurements would be required where parts of the system need to be removed from the soil sample. For a novel custom GPR monitoring system with about 2500 antennas, this is not feasible. Therefore, novel calibration methods for stationary multichannel monitoring systems are required to capture the temporal drift of time-zero caused by hardware instabilities, hardware aging and temperature dependencies. In this work, novel calibration approaches are presented that make use of both the reciprocity of electromagnetic waves inside the soil and internal signal reflections in the measurement system to derive the system specific time delay without the necessity of knowing the medium between the antennas. The complexity of the system is increased step by step to derive the essential elements of the calibration. First, a numerical simulation is used to show the potential of superpositioned reciprocal measurements which significantly reduce random measurement errors. Afterwards, it is demonstrated that parasitic reflections and coupling signals within the monitoring system are necessary for a complete in situ calibration. The final presented approach is capable of identifying and correcting for differences in the hardware, while also correcting temporal changes of time-zero during experiments. First, the presented approach is tested on a minimal working example that incorporates the analog signal path up to the antenna. These measurements show that the method is capable to reduce the error of time-zero to below 25 ps and that the largest source of error are fabrication differences of the hardware. Subsequently, the method is evaluated on a prototype of the monitoring system. The prototype contains all key components including trigger lines, FPGAs and converters. Due to the resynchronisation of the GPR system, larger time deviations of up to 3 ns occur in the time-zeros, which can be corrected with the in situ calibration. For evaluation, the in situ calibration is compared with the standard calibration procedure and yields a maximum error of 4 ps. The presented approach is characterized by requiring no additional calibration setups or measurements since all the necessary data can be acquired during normal operation of soil measurements.

Zusammenfassung

Eine hochentwickelte und umfassende Verarbeitung von Bodenradardaten, wie sie beispielsweise für die Anwendung von Vollewellenform-Inversionsverfahren erforderlich ist, bedingt eine präzise zeitliche Kalibrierung des Systems. Üblicherweise erfolgt die Kalibrierung von Bodenradarsystemen mithilfe eines bekannten Mediums, das zwischen den Sende- und Empfangsantennen platziert wird. Dabei wird die gemessene Zeitdifferenz zwischen den erwarteten und tatsächlichen Signalankunftszeiten, bezeichnet als Nullzeit, als systembedingte Zeitverzögerung berücksichtigt. In Fällen, in denen die Antennen zu Überwachungszwecken dauerhaft um Bodenproben positioniert werden, erfordert die Kalibrierung zeitaufwendige zusätzliche Messungen, da Teile des Systems von der Bodenprobe entfernt werden müssen. Für ein neuartiges GPR-System mit etwa 2500 Antennen gestaltet sich dieses Vorgehen als nicht praktikabel. Daher sind innovative Kalibrierungsmethoden für stationäre GPR-Mehrkanalsysteme notwendig, um die zeitlichen Veränderungen der Nullzeit zu erfassen, die durch Hardwareinstabilitäten, Alterung der Komponenten und Temperaturabhängigkeiten verursacht werden. In dieser Arbeit werden neuartige Kalibrierungsansätze vorgestellt, die sowohl die Reziprozität elektromagnetischer Wellen als auch interne Signalreflexionen im Messsystem nutzen, um die systemspezifische Zeitverzögerung zu ermitteln, ohne dass das Medium zwischen den Antennen bekannt sein muss. Die Abstraktion des GPR-Systems wird schrittweise angepasst, um die grundlegenden Elemente der Kalibrierung herzuleiten. Zuerst wird mithilfe einer numerischen Simulation das Potenzial von kombinierten reziproken Messungen aufgezeigt, die zufällige Messfehler erheblich reduzieren können. Daraufhin wird demonstriert, dass parasitäre Reflexionen und gekoppelte Signale innerhalb des GPR-Systems für eine vollständige In-situ-Kalibrierung notwendig sind. Der abschließend vorgestellte Ansatz ist dazu in der Lage, Unterschiede in der Hardware zu erkennen und zu korrigieren sowie zeitliche Änderungen der Nullzeit während der Experimente auszugleichen. Zunächst wird dieser Ansatz an einem Minimalbeispiel getestet, das den analogen Signalpfad bis zur Antenne beinhaltet. Diese Versuche zeigen, dass die Methode Fehler in der Nullzeit auf unter 25 ps reduzieren kann, wobei die hauptsächliche Fehlerquelle in den Fertigungsabweichungen der Hardwarekomponenten liegt. Anschließend erfolgt die Evaluierung des Ansatzes anhand eines Prototypen des GPR-Systems. Dieser Prototyp beinhaltet alle essenziellen Komponenten wie Triggerleitungen, FPGAs, Signalgeneratoren und Datenerfassungseinheiten. Durch die Resynchronisation des GPR-Systems treten größere Zeitabweichungen von bis zu 3 ns in den Nullzeiten auf, die mithilfe der In-situ-Kalibrierung korrigiert werden können. Zur Evaluierung wird die In-situ-Kalibration mit dem Standardverfahren zur Kalibration verglichen und weißt dabei einen maximalen Fehler von 4 ps auf. Der vorgestellte

Ansatz zeichnet sich dadurch aus, dass keine zusätzlichen Kalibrierungseinstellungen oder Messungen erforderlich sind, da sämtliche benötigten Daten während des operativen Betriebs der Bodenmessungen erfasst werden können.

Abbreviations and symbols

Abbreviations

Abbreviation	Denomination
ADC	Analog-digital converter
AWG	Arbitrary waveform generator
BAB	Baseboard
CLK	Clock
CMP	Common-midpoint
CRIM	Complex refractive index model
DAC	Digital-analog converter
DFT	Discrete fourier transformation
EM	Electromagnetic
FD	Frequency-Domain
FDTD	Finite differences time domain
FO	Fixed-offset
FT	Fourier-transformation
FWI	Full-waveform inversion
GPR	Ground penetrating radar
GSa/s	Gigasamples per second
IDFT	Inverse discrete fourier transformation
IFFT	Inverse fast fourier transformation
LTI	Linear time-invariant
MAM	Master module
MOG	Multi-offset gather
PCB	Printed circuit board
PGA	Programmable gain amplifier
PLL	Phase-locked loop
PVC	Polyvinyl chloride
Rx	Receiver
SAR	Synthetic aperture radar
SNR	Signal-to-noise ratio
SP3T	1-to-3 switch
SWC	Soil water content
TD	Time-domain
TDR	Time-domain reflectometry

Abbreviation	Denomination
Tx	Transmitter
VNA	Vector network analyzer
VOP	Vertical-offset profiling
WARR	Wide angle reflection and refraction
ZOP	Zero-offset profiling

Symbols

Symbol	Description
c_0	Speed of light in vacuum
E	Electic field strength vector
B	Magnetic flux density vector
H	Magnetic field intensity
J	Electic current density vector
D	Electric displacement vector
ρ	Electric charge density
∇	Nabla operator
ε	Dielectric permittivity ($\varepsilon_0 \approx 8.854 \cdot 10^{-12}$ F/m in free space)
σ	Electrical conductivity
μ	Magnetic permeability ($\mu_0 \approx 1.256 \cdot 10^{-6}$ N/A^2 in free space)
ω	Angular frequency
$\delta(t)$	Dirac pulse
$h(t)$	Impulse response
$H(t)$	Transfer function
$\varphi(\omega)$	Phase
$\psi(t)$	Ricker wavelet
t_0	Time-zero; time reference for measured signals
$t_{0\,i\,j}$	Time-zero for two arbitrary base boards i and j
t_a	Signal arrival time
$\boldsymbol{t}$	Vector of trigger times for n base boards; $\boldsymbol{t} = (t_1, ..., t_n)^\mathrm{T}$
t_Tx	Instrumental delay in Tx circuit
t_Rx	Instrumental delay in Rx circuit
$t_\mathrm{Tx\,Rx}$	Sum of instrumental delays in Tx and Rx circuit
t_p	Propagation time of signal between antennas
$t_{i\,j}$	Trigger offset between two arbitrary base boards i and j
t_offset	Timing offset to identify the antenna feed point reflection within internal reflection measurements (3.48)

Symbol	Description
$\overline{t}_{\text{offset}}$	Mean timing offset for a fix antenna combination over multiple measurements (3.49). A distinction is made between the mean timing offset for Tx and Rx mode
$\hat{t}_{\text{offset}}$	Mean timing offset for multiple antenna combinations and over multiple measurements (3.50). As for $\overline{t}_{\text{offset}}$, a distinction is made between the timing offset for Tx and Rx mode
$\overline{\epsilon}$	Average error for time-zero when using the channel dependent $\overline{t}_{\text{offset}}$
$\hat{\epsilon}$	Average error for time-zero when using the universal offset $\hat{t}_{\text{offset}}$
ξ	Normal distributed random error variable
$R(t_{\text{shift}})$	Cross correlation of two signals for a given time shift t_{shift}
ζ	Instability index used to quantitatively assess the stability of internal reflection measurements
$\mathcal{H}$	Hilbert transformation
$\psi_{\text{a}}(t)$	Analytical signal of Ricker wavelet

Contents

Chapter 1

Introduction

1.1 Motivation

Feeding a growing world population is a central challenge of today [1, 2, 3]. Especially in view of climate change, it is becoming increasingly important to identify and improve the understanding of factors influencing efficient and climate-friendly agriculture [4]. Here, soil processes and soil-plant interactions play a crucial role. To investigate these processes non-invasively, various measurement techniques are used. One of these measurement techniques is the ground penetrating radar (GPR). GPR is a non-invasive electromagnetic (EM) geophysical technique to investigate the shallow subsurface of soils by emitting radio frequency EM waves into the soil and receiving a response signal via antennas [5]. GPR fills the gap between point-scale measurement techniques, such as time-domain reflectometry (TDR) and large scale remote sensing techniques, such as synthetic aperture radar (SAR). Most commercial GPR systems operate at frequencies between 50 MHz and 3.6 GHz [6]. GPR systems either operate in time-domain (TD) by emitting short broadband pulses or in the frequency-domain (FD) by sweeping over a range of frequencies. The propagation of emitted EM waves depends on the relative dielectric permittivity ε_r and the electrical conductivity σ of the subsurface. Dipole polarization is the predominant effect for GPR frequencies and dominates the conductive properties for many geophysical materials [7]. Typical permittivity values vary in the range of $\varepsilon_\mathrm{r} \approx 1$ for air and $\varepsilon_\mathrm{r} \approx 80$ for water, making the permittivity highly sensitive to soil water content (SWC). The correlation between the propagation of EM waves and the soil permittivity allows to observe SWC variations using appropriate petrophysical models [8]. E.g., Paz et al. (2017) [9] provide an overview of GPR uses for groundwater-related ecosystem research with over 90 worldwide GPR case studies. Especially in agriculture, monitoring the SWC with fast and accurate measurement techniques, such as GPR, is of importance [10, 11, 12]. Bolten et al. (2010) [13] use remotely sensed surface soil moisture to enhance predictions of the root-zone and, thus, of agricultural yields. Benedetto et al. (2019) [14] combine electromagnetic induction and GPR data to improve the SWC estimation on an agricultural field and, thereby, enhance the understanding of soil degradation. Also, the determination of soil parameters for land rearrangement is crucial [15], as land rearrangement has among other things the objective of creating suitable conditions for crop growth. The determination of SWC via GPR can also be used to detect leaks in water pipes [16, 17, 18]. In general, a better understanding of soil parameters helps to develop more sophisticated soil-plant-atmosphere models [19].

One of the most widely used relationships between SWC and the soil's permittivity is introduced by Topp et al. (1980) [20]. The empirical model was determined by performing laboratory measurements up to 1 GHz with the TDR method. The model is independent of other soil parameters such as the soil type, density, temperature and soluble salt content. Another common used relationship between permittivity and SWC is the one introduced by Roth et al. (1990) [21]. Their work builds on the findings of Dobson et al. (1985) [22] who use a three-phase system to describe the wet soil. This model takes the dielectric number of the solid, aqueous, and gaseous phase and the soil's porosity into account and is applicable to measurement frequencies of up to 18 GHz. The results in [21] show a relative uncertainty in the volumetric water content of 1.2% for wet soils. These soil-mixing models are also referred to as complex refractive index model (CRIM). While soil permittivity correlates with SWC, the conductivity provides information about clay content and fracture fluid salinity [6]. In natural media, conductivity varies between 10^{-4} and 0.1 S m^{-1} [23]. Looms et al. (2018) [24] use GPR to map sand lenses, i.e., clayey till with macropores leading to strong transport pathways, and find that sand lenses are best characterized by their conductivity. Tsoflias et al. (2008) [25] investigate the relation between GPR signal responses and the fracture fluid salinity inside the soil. They determine that low frequency systems, i.e., around 50 MHz, are well suited for conductivity and, hence, salinity measurements.

Due to its efficient measurement procedure, GPR is not only used to investigate soil properties, but also for the non-invasive inspection of roads [26, 27, 28], concrete bridges [29, 30] as well as railways [31], the assessment of contaminated areas [32, 33], and the detection of landmines [34, 35]. GPR is also widely used for measuring of permafrost areas, e.g., on the Tibetan Plateau [36, 37], the Swiss Alps [38], or the Antarctica [39].

Three GPR measurement configurations are used in practice, namely on-ground, off-ground, and borehole measurements. In on-ground measurements, the antennas are in direct contact with the ground, allowing large penetration depths. Depending on the used frequencies and investigated soils, penetration depth of multiple thousand meters can be reached [40]. In off-ground measurements, the antennas are positioned above the ground. In this setup, the EM waves penetrate less deeply into the ground due to losses at the air-soil interface, but large surface areas can be covered quickly. Additionally, the influence of antenna near-field effects caused by the soil are reduced. Wu et al. (2019) [41] install an FD GPR system on a drone to map the soil moisture of agricultural fields ($\approx$ 1 ha) with measurement times of less than 15 minutes per field. For both on-ground and off-ground configurations, common-midpoint (CMP) and wide angle reflection and refraction (WARR) measurements can be performed in addition to fixed-offset (FO) measurements, where the distance between the antennas remains the same during the measurement. In CMP measurements the transmitting and receiving antennas are moved away from each other simultaneously in a straight line, while for WARR measurements the position of one antenna remains fixed while the other antenna is moved away in a straight line. Both CMP and WARR measurements allow to identify the depth of boundary layers or buried objects in addition to soil permittivity and conductivity, but are more time consuming than FO measurements when measuring large areas. E.g., Liu et al. (2012) [42] use a self-designed bowtie GPR system to simultaneously determine the permittivity and thickness of the grouting layer in a tunnel using CMP measurements. Longer data acquisition times for CMP and WARR surveys can be overcome by using multi-channel systems with multiple antennas as in, e.g., [43] or [44]. The third GPR measurement configuration is the borehole setup. Here, GPR systems either operate in one borehole, between two boreholes to perform crosshole measurements via zero-offset profiling (ZOP) or multi-offset gathers (MOG), or from a borehole to the surface via vertical-offset profiling (VOP) [40]. Sato et al. (1991) [45] derive an analytical description of the current distribution on a borehole-antenna and of the received crosshole signal. The crosshole setup in combination with acquiring MOG enables the GPR operator to determine a tomographic image of ε_r and σ and, therefore, the SWC between the boreholes with a higher spatial resolution in deeper soil areas compared to on-ground or off-ground surveys. The drawback of this measurement setup is the great time effort to perform measurements as the antennas are repeatedly re-positioned in the boreholes. In addition, the boreholes must initially be drilled. E.g., Binley et al. (2001) [46] perform transmission measurements between boreholes to characterize the change of SWC in sandstone over 18 month with a high spatial resolution, while Liu et al. (2019) [47] use single-hole and crosshole measurements to identify leakage paths in dam foundations. To analyze the crosshole data, different inversion schemes can be applied. Qin et al. (2021) [48] implement a probabilistic inversion based on a straight-ray model and test their approach on synthetic data. Especially in the last decade, crosshole GPR full-waveform inversion (FWI) [49]) has shown a high potential to derive high decimeter scale images of the subsurface. The FWI for GPR data is mainly derived from Tarantola et al. (1984) [50], who introduce a nonlinear inversion method for seismic reflection data. Ernst et al. (2007) [51] and Meles et al. (2010) [52] adapt this approach for TD GPR crosshole data. Klotzsche et al. (2010) [53] and Klotzsche et al. (2013) [54] apply the FWI to crosshole measurements for the characterization of gravel aquifer at different locations. Gueting et al. (2017) [55] also use the FWI for aquifer characterization and find that the FWI yields higher spatial resolutions than standard ray-based inversions which is important to identify small-scale aquifer structures. Further, Zhou et al. (2020) [56] improve the FWI results of a Belgian test-site by compromising an amplitude analysis prior to the FWI. The interested reader is referred to Klotzsche et al. (2019) [49], who give an extensive review of the theory and applications of crosshole FWI.

1.2 GPR calibration

GPR systems derive the soil's permittivity by determining the propagation time and, hence, the velocity of EM waves in the soil. In order to determine the signal propagation time between transmitting (Tx) and receiving (Rx) antennas, a time reference for the measured signals has to be defined, termed as time-zero, t_0 [57]. Any point within the signal can be used as a reference point, as long as all time information in the following refers to this reference point. Typical reference points are for example the first onset of the signal, termed as arrival time, or the first break point, i.e., the first maximum/minimum within the signal. The time-zero correction aims to find a reliable time reference and ensures that no parasitic signal instrumental delays from within the measuring instruments, e.g., caused by system timing and cables [58], is included in the data [59, 60]. Beyond that, the time-zero correction monitors changes in time-zero due to, e.g., thermal drifts, damaged cables or electronic instability [8] and is, therefore, time dependent. Furthermore, Klotzsche et al. (2019) [49] point out that the accurate time-zero correction is a crucial step in the pre-processing to accurately apply an FWI to the data. Time-zero is commonly defined as

$$t_0 := t_\mathrm{a} - \frac{d}{c_0}\,, \tag{1.1}$$

where t_a is the arrival time of the direct air wave between Tx and Rx, d is the propagation distance of the direct air wave and c_0 is the speed of light in vacuum [61]. Note that the air wave always arrives first at Rx under a line of sight condition, where the shortest path between Tx and Rx runs through air. Due to antenna near-field effects and an interference of the air wave and ground wave, the direct air wave can have a velocity that differs from the assumed c_0 ([62]), resulting in an erroneous time-zero when using (1.1). Thus, it is advised to use a linear regression to deduce time-zero and the signal's velocity v from multiple measurements with different distances d between Tx and Rx, where

$$t_\mathrm{a}(d) = t_0 + \frac{d}{v}\,. \tag{1.2}$$

The calibration data required to use (1.2) is acquired either by performing CMP or WARR measurements or by sequentially lifting Tx and Rx above a known reflector and measuring the two-way propagation time [63]. Schmalholz et al. (2004) [64] on the other hand repeatedly place the antennas directly next to each other to perform and update the calibration but it is not specified if this approach has an influence on time-zero due to near-field effects. Instead of measuring time-zero directly via (1.1) or (1.2), another approach is to determine time-zero via an inversion. Gerhards et al. (2008) [62] implement a multipoint inversion that minimizes an objective function which contains the air wave propagation time as a free parameter to calibrate a multichannel GPR system. This approach suffers from numerical instabilities. The authors, therefore, recommend to exclude time-zero from the inversion. Kaufmann et al. (2020) [65] present a novel time-zero calibration method to calibrate the WARR-machine [44], a GPR on-ground system that utilizes one transmitting antenna and seven receiving antennas. Each receiving antenna has its own data acquisition hardware, making a time-zero correction for each receiving antenna necessary. The final calibration scheme yields precise time-zero by finding the minimum of a defined objective function, while the calibration measurement itself takes measurement times of about 40 minutes. In this study, it is observed, while the setup is always exactly the same, that the time-zero difference of each Tx-Rx pair to the first pair was stable and only an overall time-zero shift needs to be determined. Radzevicius et al. (2015) [66] use a combined least-squares and grid search algorithm to determine time-zero along with further model parameters. Directly including time-zero in the objective function was not successful due to the ill-posedness of the inverse problem. Viriyamentanont et al. (2008) [67] conduct an effective time-zero correction based on the direct wave propagating inside concrete instead of using the direct air wave. This method requires known reflector depths inside the concrete. All of these approaches have in common, that either a direct air wave must be measurable, or that there must be a well-specified object in the medium. For crosshole measurements, neither of these requirements is fulfilled if Tx and Rx antennas are placed in separate boreholes with an unknown soil between the boreholes. Therefore, the antennas are repeatedly placed in air after several crosshole acquisitions, e.g., after 10 measurements [68, 24], to conduct time-zero correction measurements according to (1.1) or (1.2) and to capture the time variability of time-zero. Afterwards, time-zero values from successive time-zero correction measurements are linearly interpolated to obtain an individual time-zero for each crosshole measurement. This approach is very time consuming as calibration measurements have to be performed repeatedly. Oberröhrmann et al. (2012) [68] introduce a cross correlation method to enhance the time-zero accuracy for crosshole measurements by linking traces that are measured at comparable Tx-Rx positions. This is especially important due to the sensitivity of the FWI to small time-zero errors [49]. Generally, errors in time-zero directly transfer to errors of the soil permittivity, or, e.g., the depth and diameter of buried objects [69].

1.3 Novel GPR applications and systems

Until now the TD crosshole GPR FWI was mainly applied to investigate aquifers and related processes within decimeter scale. Within the last years, a need to detect smaller structures and to map more detailed and faster processes like preferential flow paths or root zones becomes more and more important to enhance model predictions. To achieve this, higher frequency antennas that provide a higher resolution and faster measurement techniques are essential. First synthetic studies are carried out to show the potential of high frequency GPR measurements for 3D soil studies [70]. Currently, a novel TD GPR monitoring system is investigated that extends the crosshole setup. The monitoring system will allow to radiate EM waves into a soil column from all spatial directions, similar to, e.g., Stoffregen et al. (2002) [71] and Schmalholz et al. (2004) [64]. Instead of placing single hand-held Tx/Rx antennas at the soil, the approach comprises to permanently mount up to 2500 antennas on the outside of a lysimeter (a cylindrical shell, used by, e.g., Hannes et al. (2005) [72] and Pütz et al. (2016) [73]). This allows for extremely fast tomography measurements of large soil columns to, e.g., investigate flow processes. The aforementioned TD FWI is then used to analyze the measured GPR data. Other multichannel GPR systems are developed and/or used, e.g., by Wollschläger et al. (2010) [36], Xu et al. (2014) [74], Viberg et al. (2020) [75], or Garcia-Fernandez et al. (2020) [76]. These systems use a maximum of a few dozen antennas and differ significantly in complexity from the monitoring system presented in this work. Such a permanently installed monitoring setup prevents the use of existing calibration approaches that utilize the air wave for an accurate time-zero correction since there is always unknown soil between the antennas. Additionally, the large amount of possible Tx/Rx combinations requires a novel automated in situ approach for the time-zero correction, because a manual time-zero correction for each of the approximately 9 million Tx/Rx combinations is not feasible. Performing the calibration at an empty lysimeter could be done, but this would prevent to identify temporal changes of time-zero. Therefore, the novel method must be able to perform the time-zero correction periodically to capture possible changes.

Approaches to calibrate systems using antenna arrays can be found in the field of digital beamforming. Hoffman et al. (2012) [77] implement calibration circuits within the system to calibrate the transmit circuit, the receive circuit and the clock timing of different channels. The behaviour of these calibration circuits over temperature has to be known very well. Harter et al. (2016) [78] applies a self calibration procedure which uses the response of target elements positioned in the far field of the antenna array. Kim et al. (2019) [79] use a calibration signal to determine relative time shifts between antenna channels. The absolute signal propagation times required for the time correction are determined once after fabrication. Jäger et al. (2019) [80] introduce an approach for the calibration of propagation direction dependent effects to improve SAR data quality. This approach also needs a well-defined target response. Further approaches to calibrate antenna arrays involve using the mutual signal coupling between individual antennas of the array as it is assumed that this coupling is constant [81, 82, 83]. The approaches used in digital beamforming have disadvantages regarding the application within the developed GPR monitoring system, as (i) additional calibration hardware causes additional cost and the system design would have to be adapted, (ii) no measurements with well-specified targets in the far field are possible and (iii) the mutual coupling between neighboring antennas determine relative time shifts but no absolute time-zero.

1.4 Structure of this work

All introduced calibration methods, both from GPR and digital beamforming, require measurement information that is not available for the stationary multichannel GPR monitoring system. Therefore, the aim of this work is to develop a novel in situ calibration procedure that allows to generate both spatially and temporally highly resolved GPR images with the monitoring system. For this purpose, chapter 2 first presents the essential physical principles that are necessary to derive the calibration approach. This includes an introduction to the theory of electromagnetic wave propagation and the theory of linear systems. In chapter 3, the monitoring system is presented in detail as a detailed understanding of the timings within the GPR system is crucial to develop the calibration approach. This chapter then presents the considerations up to the final calibration procedure. In chapters 4 and 5, the approach is analyzed on the basis of numerical models and laboratory experiments, and finally tested as well as verified on a prototype system in chapter 6.

Chapter 2

Fundamentals

This chapter describes all theoretical basics that are relevant for the understanding of this work. First, a derivation of electromagnetic waves including their most important properties is given, since these form the basis of the measurement principle in ground penetrating rader (GPR). Then, the behavior of electromagnetic waves in linear media is discussed to derive the reciprocity theorem. The second section of this chapter covers the theory for the analysis of linear systems, such as the soil, in the time and frequency domain.

2.1 Electromagnetic wave properties

2.1.1 Derivation

The foundation of electromagnetism, and thereby also of GPR, are mathematically described by the Maxwell equations. The Maxwell equations according to Heaviside [84] are given by

$$\nabla \times E = -\frac{\partial B}{\partial t} \tag{2.1}$$

$$\nabla \times H = J + \frac{\partial D}{\partial t} \tag{2.2}$$

$$\nabla \cdot D = \rho \tag{2.3}$$

$$\nabla \cdot B = 0\,, \tag{2.4}$$

where E is the electric field strength vector, B is the magnetic flux density vector, H is the magnetic field intensity, J is the electric current density vector, D is the electric displacement vector, ρ is the electric charge density and ∇ is the nabla operator. The constitutive equations for electomagnetic properties are given as

$$J = \sigma E \tag{2.5}$$
$$D = \varepsilon E \tag{2.6}$$
$$B = \mu H\,, \tag{2.7}$$

where σ is the electrical conductivity, ε is the dielectric permittivity and μ is the magnetic permeability. The proportionality quantities σ, ε and μ are usually assumed to be scalar quantities, but can also be in tensor form to describe directional dependency. This will be briefly discussed in the discussion of reciprocity in section 2.1.2. For the rest of this subsection, scalar quantities are assumed. Applying ∇ to (2.1) and using the constitutive equations yields

$$\nabla \times (\nabla \times E) = \nabla \times (-\frac{\partial B}{\partial t}) = -\frac{\partial}{\partial t}(\nabla \times B) = -\mu\sigma\frac{\partial E}{\partial t} - \mu\varepsilon\frac{\partial^2 E}{\partial^2 t}\,.$$

With $\nabla \times (\nabla \times E) = -\nabla^2 E$, it follows that in free space ($\varepsilon = \varepsilon_0 \approx 8.854 \cdot 10^{-12}$ F/m, $\mu = \mu_0 \approx 1.256 \cdot 10^{-6}$ N/A^2, $\sigma = 0$)

$$\mu_0\varepsilon_0\frac{\partial^2 E}{\partial^2 t} - \nabla^2 E = 0 \tag{2.8}$$

and analogously for the magnetic field

$$\mu_0\varepsilon_0\frac{\partial^2 B}{\partial^2 t} - \nabla^2 B = 0\,. \tag{2.9}$$

The last two equations are called the transverse vector wave equations and show that E- and B-fields propagate as waves with the plane wave solution

$$E(r,t) = E_0 e^{j(\omega t - k r)}\,, \tag{2.10}$$

where r is the position, t is the time, E_0 is the peak amplitude, and $k = 2\pi/\lambda$ is the wave number or spatial frequency in free space with λ as the wavelength. The velocity of this wave, also known as the speed of light in free space, c_0, is defined as

$$\frac{1}{c_0^2} = \mu_0\varepsilon_0 \Leftrightarrow c_0 = \frac{1}{\sqrt{\mu_0\varepsilon_0}} = 299792458\,\frac{\mathrm{m}}{\mathrm{s}}\,. \tag{2.11}$$

In any other medium with permittivity $\varepsilon = \varepsilon_0\varepsilon_\mathrm{r}$ and permeability $\mu = \mu_0\mu_\mathrm{r}$ the velocity is given by

$$v = \frac{1}{\sqrt{\mu_0\mu_\mathrm{r}\varepsilon_0\varepsilon_\mathrm{r}}} = \frac{c_0}{\sqrt{\mu_\mathrm{r}\varepsilon_\mathrm{r}}}\,. \tag{2.12}$$

For non magnetic and non dispersive media, the relative permittivity ε_r is the only parameter which determines the velocity of electromagnetic (EM) waves in a medium [5]:

$$\varepsilon_\mathrm{r} = \left(\frac{c_0}{v}\right)^2 = \left(\frac{c_0}{d/t_\mathrm{p}}\right)^2 , \tag{2.13}$$

where d is the distance that the EM wave travels inside the medium and t_p is the propagation time that the EM wave needs to travel that distance. This is one of the fundamental equations that is used in GPR. Knowing d and t_p gives an average relative permittivity of the travel path in the soil. For the measurement of t_p, a time reference is needed, because measured GPR signals are always corrupted by signal propagation times outside the ground or inside the GPR system itself. This time reference is called time-zero and is defined in (1.1). In the general case and for soils with $\sigma \neq 0$, a complex relative dielectric permittivity is defined as

$$\varepsilon_\mathrm{r} = \varepsilon_\mathrm{r}^{'} - j\varepsilon_\mathrm{r}^{''} = \varepsilon_\mathrm{r}^{'} - j\frac{\sigma}{\varepsilon_0\omega} , \tag{2.14}$$

where the real part equals the dielectric permittivity for non conductive media, while the imaginary part represents the loss term associated with losses due to current flow. The quotient of imaginary and real part of the complex permittivity is termed as loss tangent

$$\tan\delta = \frac{\varepsilon_\mathrm{r}^{''}}{\varepsilon_\mathrm{r}^{'}} = \frac{\sigma}{\varepsilon\omega} . \tag{2.15}$$

Most soils that are investigated by GPR fulfill the low-loss criterion, i.e., $\tan\delta \ll 1$. Thus, (2.13) can be used as an approximation to determine the relative permittivity (e.g., [23]). When substituting the plane wave solution into the transverse vector wave equation, one gets $k^2 - \varepsilon\mu\omega^2 - j\omega\mu\sigma = 0$ and rearranging yields the propagation constant $k = \alpha + j\beta$ with

$$\alpha = \omega\sqrt{\frac{\varepsilon\mu}{2}\left(\sqrt{1+\tan^2\delta} - 1\right)} \tag{2.16}$$

and

$$\beta = \omega\sqrt{\frac{\varepsilon\mu}{2}\left(\sqrt{1+\tan^2\delta} + 1\right)} . \tag{2.17}$$

α is termed the attenuation constant and shows that EM waves experience stronger attenuation for higher frequencies in conductive media. β is termed the phase constant and describes the distortion of the EM wave while traveling through a medium [85]. An overview of typical values for ε_r, σ and $\tan\delta$ in soils is given in Tab. 2.1.

Table 2.1: Relative permittivity, conductivity and loss tangent of common soil materials measured at 100 MHz [85], [57].

Material	ε_r / –	σ / S/m	$\tan\delta$ / –
Air	1	0	0
Freshwater	81	$10^{-6} - 10^{-2}$	$2 \cdot 10^{-6} - 2 \cdot 10^{-2}$
Clay, dry	2 - 6	$10^{-3} - 10^{-1}$	$3 \cdot 10^{-2} - 9 \cdot 10^{-0}$
Clay, wet	5 - 40	$10^{-1} - 10^{-0}$	$5 \cdot 10^{-1} - 4 \cdot 10^{1}$
Sand, dry	2 - 6	$10^{-7} - 10^{-3}$	$3 \cdot 10^{-6} - 9 \cdot 10^{-2}$
Sand, wet	10 - 30	$10^{-3} - 10^{-2}$	$6 \cdot 10^{-3} - 2 \cdot 10^{-1}$

2.1.2 Reciprocity

The reciprocity of electromagnetic waves is crucial for the calibration approach, which will be derived later in the thesis. Therefore, all basics and prerequisites needed to ensure reciprocity in a medium are presented here. Generally speaking, reciprocity of electromagnetic fields refers to the fact that interchanging the source location of a signal and the measurement location of the signal generated by the signal at the source location leads to the same measured signal [86]. For the derivation, the case of two source currents J_1 and J_2 at arbitrary locations, e.g., r_1 and r_2, generating the electric fields E_1 and E_2, respectively, and the magnetic fields H_1 and H_2, respectively, is considered. According to Maxwell's equations

$$\nabla \times E_1 = -\frac{\partial B_1}{\partial t} \tag{2.18}$$

$$\nabla \times H_1 = J_1 + \frac{\partial D_1}{\partial t} \tag{2.19}$$

and

$$\nabla \times E_2 = -\frac{\partial B_2}{\partial t} \tag{2.20}$$

$$\nabla \times H_2 = J_2 + \frac{\partial D_2}{\partial t} \tag{2.21}$$

is valid. Multiplying (2.18) by H_2 and (2.19) by E_2 and, analogously, (2.20) by H_1 and (2.21) by E_1 yields

$$H_2 \nabla \times E_1 = -H_2 \frac{\partial B_1}{\partial t} \tag{2.22}$$

$$E_2 \nabla \times H_1 = E_2 J_1 + E_2 \frac{\partial D_1}{\partial t} \tag{2.23}$$

$$H_1 \nabla \times E_2 = -H_1 \frac{\partial B_2}{\partial t} \tag{2.24}$$

$$E_1 \nabla \times H_2 = E_1 J_2 + E_1 \frac{\partial D_2}{\partial t} \,. \tag{2.25}$$

Subtracting (2.23) from (2.24) and (2.25) from (2.22) yields

$$H_1 \nabla \times E_2 - E_2 \nabla \times H_1 = -H_1 \frac{\partial B_2}{\partial t} - E_2 J_1 - E_2 \frac{\partial D_1}{\partial t} \tag{2.26}$$

$$H_2 \nabla \times E_1 - E_1 \nabla \times H_2 = -H_2 \frac{\partial B_1}{\partial t} - E_1 J_2 - E_1 \frac{\partial D_2}{\partial t} \,. \tag{2.27}$$

At this point, the last term $E_2 \frac{\partial D_1}{\partial t}$ in (2.26) and $E_1 \frac{\partial D_2}{\partial t}$ in (2.27) are compared. Substituting the constitutive equations yields $E_2 \frac{\partial}{\partial t} \varepsilon_0 \varepsilon_\mathrm{r} E_1$ and $E_1 \frac{\partial}{\partial t} \varepsilon_0 \varepsilon_\mathrm{r} E_2$, where ε_r is now the permittivity tensor of rank 2, i.e., a 3x3 matrix. This takes into account the general case of a directional medium, even though the directionality is often negligable. Equality for the two expressions holds exactly when $\varepsilon_\mathrm{r} = \varepsilon_\mathrm{r}^T$, i.e., when the permittivity tensor is symmetric. A medium for which $\varepsilon_\mathrm{r} = \varepsilon_\mathrm{r}^T$ holds is called linear. This includes, for example, the soils studied in this thesis. If ε_r is assumed to be a scalar, the equality holds trivially. Furthermore, if the permeability tensor μ is also symmetric, it follows from (2.27) - (2.26) that

$$\nabla(E_1 \times H_2 - E_2 \times H_1) = -E_1 J_2 + E_2 J_1 \,. \tag{2.28}$$

In integral form and after application of Gauss' theorem, the reciprocity theorem results as

$$\int E_1 \, J_2 \, dV = \int E_2 \, J_1 \, dV \,. \tag{2.29}$$

Thus, if a current J_1 is applied at position r_1, an E-field $E_1(r_2)$ results at position r_2. If now the current J_2 with the same amplitude is applied at position r_2, an E-field $E_2(r_1)$ results at position r_1 [86]. According to the reciprocity theorem, $E_1(r_2)$ and $E_2(r_1)$ are equal. This is essential for the calibration approach presented later.

2.2 Time- and frequency-domain analysis

2.2.1 Linear time-invariant system analysis

The soil can be considered as a linear system as the soil responds linearly to GPR signals. Further, when the soil, i.e., the permittivity and conductivity, are constant in time during a measurement, the soil is considered as time-invariant. Thus, the soil is considered as a linear time-invariant (LTI) system [40]. The theory for the analysis of LTI systems is presented in the following sections based on Unbehauen (2002) [87] and Westermann

(2011) [88]. For the analysis of LTI systems, the Dirac pulse $\delta(t)$, defined as

$$\delta(t) = \begin{cases} \infty & \text{if } t = 0 \\ 0 & \text{else}, \end{cases} \tag{2.30}$$

and with the property

$$\int_{-\infty}^{\infty} \delta(t)\, dt = 1 \tag{2.31}$$

plays a decisive role, since the impulse response $h(t)$ results at the output of an LTI system when excited with the Dirac pulse $\delta(t)$. The impulse response fully specifies an LTI system [87]. The output signal $y(t)$ of an LTI for any input signal $x(t)$ is calculated by the convolution integral

$$y(t) = \int_{-\infty}^{\infty} x(\tau)\, h(t-\tau)\, d\tau = x(t) * h(t)\,. \tag{2.32}$$

Consequently, the output signal can be calculated for a known $h(t)$. For an exponential input signal $x(t) = e^{j\omega t}$, it follows with the impulse response of the LTI system that $y(t) = H(\omega)e^{j\omega t}$, where $H(\omega) = |H(\omega)|\, e^{j\varphi(\omega)}$ is the transfer function of the LTI system and the Fourier transformation (FT) of $h(t)$. This illustrates that $H(\omega)$ is the response of the LTI system and describes both the amplitude $|H(\omega)|$ and the phase $\varphi(\omega)$ of an exponential input signal when passing the system. For general signals $f(t)$ the FT is defined as

$$F(\omega) = \int_{-\infty}^{\infty} f(t)\, e^{-j\omega t}\, dt \tag{2.33}$$

with the inverse transformation

$$f(t) = \frac{1}{2\pi} \int_{-\infty}^{\infty} F(\omega)\, e^{j\omega t}\, d\omega \tag{2.34}$$

with shortened notation $f(t) \,\Delta\, F(\omega)$ [87]. At this point, several important time signals with their corresponding Fourier transformations are listed as well as calculation rules with the FT, since these are important for calculations within this work. The Fourier transformation of the Dirac impulse is

$$\delta(t) \,\Delta\, 1\,. \tag{2.35}$$

In addition to the Dirac impulse, the rectangular function $\text{rect}(t)$

$$\text{rect}\left(\frac{t - T_0}{\Delta T}\right) = \begin{cases} 1 & \text{if } |t - T_0| \leq \frac{\Delta T}{2} \\ 0 & \text{else}, \end{cases} \tag{2.36}$$

where T_0 and ΔT are the time shift and duration of the signal, is important for reconstructing measured signals and deriving interpolation formulas. the rectangular function has the corresponding FT

$$\operatorname{rect}\left(\frac{t}{\Delta T}\right) \Delta\, \Delta T \operatorname{si}\left(\frac{\omega \Delta T}{2}\right) \tag{2.37}$$

with $\operatorname{si}(t) = \sin(x)/x$. In general, the symmetry property exists between a function in the time domain and the corresponding FT:

$$F(t) \,\Delta\, 2\pi f(-\omega)\,. \tag{2.38}$$

The differentiation in the time domain leads to a multiplication with ω in the frequency domain:

$$\frac{\delta^n}{\delta^n t} f(t) \,\Delta\, (j\omega)^n\, F(\omega)\,. \tag{2.39}$$

The convolution of signals in the time domain corresponds to a multiplication of the corresponding FTs:

$$f_1(t) * f_2(t) \,\Delta\, F_1(\omega) \cdot F_2(\omega)\,. \tag{2.40}$$

For the infinite sum of time-shifted Dirac functions holds

$$\sum_{n=-\infty}^{\infty} \delta(t - nT) \,\Delta\, \omega_0 \sum_{n=-\infty}^{\infty} \delta(\omega - n\omega_0) \tag{2.41}$$

and, further, the sampling theorem yields

$$f_s(t) = f(t) \cdot T_s \sum_{n=-\infty}^{\infty} \delta(t - nT_s) \,\Delta\, F_s(\omega) = \sum_{n=-\infty}^{\infty} F(\omega - n\omega_s)\,, \tag{2.42}$$

so that the spectrum repeats with period ω_s with ω_s as the sampling frequency. For a bandlimited signal $\omega_s \geq 2\omega_c$, where ω_c is the cutoff frequency of the bandlimited signal, i.e., $F(\omega) = 0$ for $|\omega| \geq \omega_c$, and $\omega_s = 2\pi f_s = 2\pi(1/T_s)$ is the sampling frequency, an ideal low-pass filter $H_{LP}(\omega) = \operatorname{rect}(\omega/\omega_s)$ can be used to completely reconstruct the original spectrum $F(\omega)$ from the sampled signal:

$$\begin{aligned} F(\omega) = F_s(\omega) \cdot H_{LP}(\omega) \bullet\!\!-\!\!\!-\!\!\circ f(t) &= f_s(t) * \frac{1}{T_s} \operatorname{si}(\frac{\pi}{T_s} t) \\ &= \sum_{n=-\infty}^{\infty} f(nT_s) \cdot \operatorname{si}\left(\frac{\pi}{T_s}(t - nT_s)\right)\,. \end{aligned} \tag{2.43}$$

This is a direct consequence of (2.37), (2.38), and (2.40). Equation (2.43) provides a formula for interpolating the signal in the time domain for any t and is called the Whittaker-

Kotelnikow-Shannon sampling theorem, who developed this formula independently [89]. The condition that $\omega_s \geq 2\omega_c$ is called the Nyquist criterion [88]. In practice, this form of interpolation is error-prone because (i) no ideal low-pass filter can be realized, (ii) the sampling of the signal is done via sample and hold stages of an analog-digital converter (ADC) and not with a dirac impulse and (iii) the sampling period is finite. To apply the FT to discrete and finite signals, the discrete Fourier transformion (DFT) is used. Here it is assumed that the signal $f(t)$ is non-zero only in the range $[0, T]$ and repeats with the frequency $\omega_0 = 2\pi/T$. Consequently, ω_0 is the lowest contained frequency in the periodic signal. Then, via a Fourier series expansion of the periodic signal, it can be shown that $F(k\,\omega_0) = \int_0^T f(t)\ \exp(-ik\omega_0 t)\,dt$ with $k \in \mathbb{Z}$. Thus, a large T results in a finer frequency resolution. In the transition from the continuous signal to the discrete measurement signal, the integral is approximated by the sum

$$F(k\,\omega_0) \approx \sum_{n=0}^{N-1} f(t_n)\exp(-ik\omega_0 t_n)\frac{T}{N} \tag{2.44}$$

with $t_n = nT/N, n = 0, ..., N-1$. Further, with $\omega_0 t_n = n2\pi/N$ the DFT follows as

$$\hat{F}(k\,\omega_0) = \frac{T}{N}\sum_{n=0}^{N-1} f(t_n)\exp\left(-2\pi i\frac{k\,n}{N}\right) \tag{2.45}$$

for any $k \in \mathbb{Z}$. However, it can be shown that for $k \geq N$, $\hat{F}(k\,\omega_0) = \hat{F}((N+k)\,\omega_0)$ so that the spectrum of the DFT repeats. Further, it can be shown that $\hat{F}((N-k)\,\omega_0) = \overline{\hat{F}(k\omega_0)}$ (conjugate complex), so that the DFT contains information only about the frequency spectrum from ω_0 to $\omega_0 N/2$ which is in accordance to the Nyquist criterion. The inverse DFT (IDFT) is found to be:

$$f(t_n) = \frac{1}{T}\sum_{k=0}^{N-1}\hat{F}(k\,\omega_0)\exp\left(2\pi i\frac{k\,n}{N}\right)\,. \tag{2.46}$$

To interpolate a discrete signal in the time domain, the DFT signal $\hat{F}(k\,\omega_0)$ can be expanded using zero-padding before the IDFT:

$$\tilde{F}(k\,\omega_0) = \begin{cases}\hat{F}(k\,\omega_0), & n = 0, ..., N-1\\ 0, & n = N, ..., M-1\end{cases} \tag{2.47}$$

and then substitute $\tilde{F}(k\,\omega_0)$ for $\hat{F}(k\,\omega_0)$ and M for N in (2.46). Note that the interpolation can reveal useful information about a signal but not create information.

2.2.2 Ricker wavelet

In the previous subsection it was shown that an LTI system, and thus also the soil, is completely described by its impulse response $h(t)$. However, since $\delta(t)$ is an unrealisable input signal in the time domain, an input signal other than $\delta(t)$ must be used. A first approach would be to approximate $\delta(t)$ by a Gaussian function $g(t)$, as

$$\delta(t) = \lim_{\epsilon\to\infty} \frac{1}{\sqrt{\pi}\epsilon} \exp\left(-\left(\frac{t}{\epsilon}\right)^2\right) = \lim_{\epsilon\to\infty} g_\epsilon(t)\,, \tag{2.48}$$

where the Gaussian curve can be realised in hardware. For a normalized Gaussian function

$$g(t) = \frac{1}{\sigma\sqrt{2\pi}} \exp\left(\frac{-t^2}{2\sigma^2}\right) \tag{2.49}$$

the FT is calculated to be

$$g(t) \,\Delta\, G(\omega) = \exp\left(-\frac{1}{2}\omega^2\sigma^2\right) \tag{2.50}$$

so that $G(\omega)$ is also a Gaussian function. The Ricker wavelet commonly used in GPR [90] is defined as the normalised second derivative of $g(t)$, i.e.,

$$\psi(t) = (1 - 2\pi^2(tf_\mathrm{c} - \sqrt{2})^2)\exp\left(-\pi^2(tf_\mathrm{c} - \sqrt{2})^2\right). \tag{2.51}$$

According to (2.39), a twofold derivative with respect to time implies a multiplication by ω^2 for the spectrum $\Psi(\omega) \bullet\!\!-\!\!\circ\, \psi(t)$. Thus, the Ricker wavelet has a wider coverage of the frequency range than the Gaussian function and is thus a better approximation to $f(t) = \delta(t) \,\Delta\, F(\omega) = 1$. Fig. 2.1 illustrates the Ricker wavelet for different f_c in time domain and the corresponding amplitude spectra.

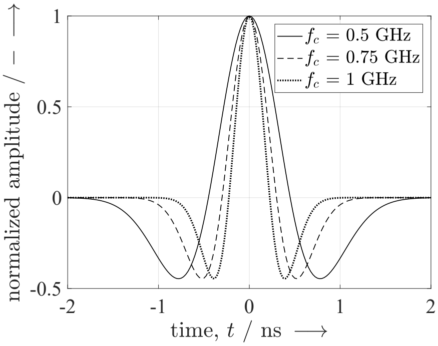

(a) Time domain

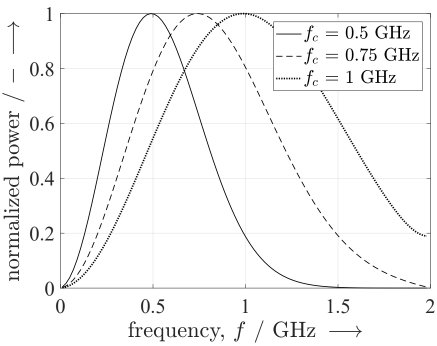

(b) Amplitude spectrum

Figure 2.1: Ricker wavelet in time domain and corresponding amplitude spectrum.

Chapter 3

Materials and Methods

In this chapter the monitoring system is presented with the necessary level of detail to develop methods for calibrating the system. First, an introduction to the AgraSim project is given, followed by a context of the GPR monitoring system within AgraSim. The main part of this chapter contains the developed approaches for the calibration of the GPR monitoring system. For first approaches, the complexity of the monitoring system is reduced. Afterwards, a sophisticated calibration for the actual monitoring system is presented. The chapter also includes model-based studies on the reciprocity of soils that have waveguide structures. The chapter concludes with analyses on methods for picking signal arrival times, as these are essential for the accuracy of the permittivity determination.

3.1 AgraSim

The Agricultural Simulator (AgraSim) project is a large-scale experiment with the objective of enhancing the utilization of nutrients and water within agricultural production systems [91]. This objective is pursued through a meticulous analysis of pivotal processes within the soil-plant-atmosphere system under both current and future environmental circumstances. The system comprises an experimental platform featuring entirely manageable mesocosms, alongside a numerical simulator reliant on high-performance computing capabilities. The experimental platform is comprised of a plant chamber, a climate chamber, and a lysimeter (Fig. 3.1). The crops, for example wheat or potato, are located directly in the plant chamber, where solar radiation, temperature, humidity and CO_2 concentration, among other isotopes, can be measured and regulated. The solar radiation can be up to 2500 μmol m^{-2} s^{-1} for wavelength between 400 nm and 700 nm corresponding to approximately 550 W m^{-2}, the temperature between -5°C and 40°C, the humidity up to 80% and the CO_2 concentration up to 2000 ppm. Note that the plant lighting provides no infrared radiation, which makes up about 50% of the solar radiation power. The plant chamber itself is located in a climate chamber that prevents condensation inside the plant chamber. Altogether, different climatic conditions

(a) (b) (c)

Figure 3.1: AgraSim setup with (a) the plant chamber, (b) the climate chamber and (c) the lysimeter. Copyright: Ralf Limbach, Forschungszentrum Jülich GmbH

and their effects on the crops can be analyzed. In addition to the plant chamber, the soil and the roots of the plants play a decisive role in understanding the effects of climate on crop yields. Therefore, AgraSim also includes a lysimeter. The lysimeter has a height of 1.5 m, a diameter of 1 m and is made of polyvinyl chloride (PVC). To avoid de-compactization of the soil when filling the lysimeter, the empty lysimeter is pressed into the soil with the help of an excavator, thus punching out a large unperturbed soil sample and is then brought to the laboratory facilities. The lysimeter is also temperature regulated and the weight of the lysimeter can be specified with an accuracy of better than 10 g. The non-invasive analysis of the soil inside the lysimeter is done via a GPR monitoring system, which is presented in section 3.2. The aim will be to monitor fast soil processes in soils, e.g., flow and transport of water and nutrients. The estimated acquisition time of a complete tomogram is 10 seconds where a complete tomogram comprises more than 6 million measurement series. The combination of measured data and the numerical simulator finally will allow a high spatial resolution of about 5 cm, which is an unprecedented resolution in the GPR field.

3.2 GPR monitoring system

This section starts with a detailed description of the GPR monitoring system. All relevant times within the system are defined. For the derivation of first calibration approaches, the complexity of the monitoring system is reduced by adding assumptions regarding the system. These assumptions are derived from initial design considerations

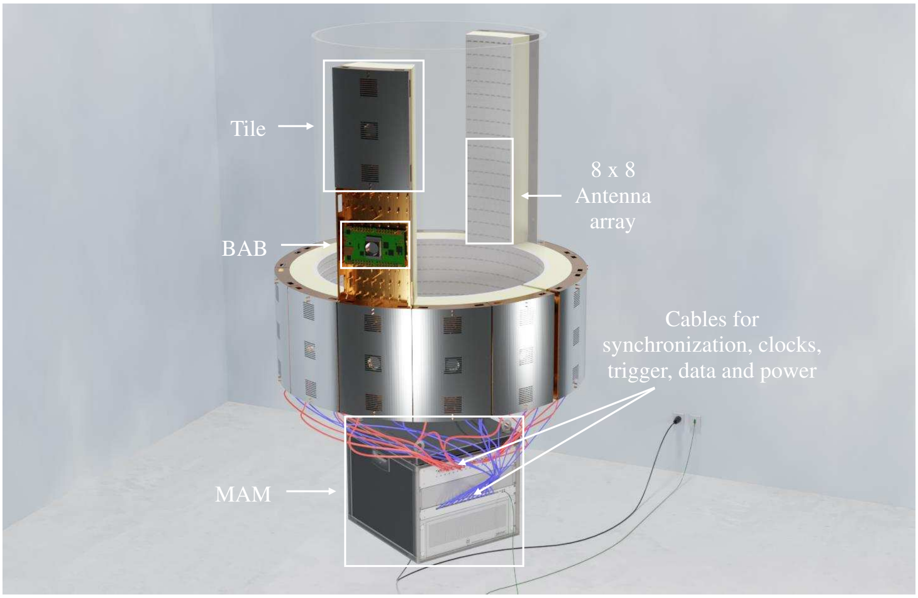

Figure 3.2: Schematic representation of GPR monitoring system positioned around a lysimeter.

regarding the monitoring system. The final calibration is then derived from the preliminary considerations of the simplified system.

3.2.1 Tile GPR system

The proposed stationary GPR monitoring system consists of about 2500 antennas that are placed around a soil-filled lysimeter (Fig. 3.2). Each antenna of the monitoring system is foreseen to transmit and receive signals. This is possible by connecting each antenna to an 1-to-3 switch (SP3T) switch. The antennas are arranged in an array structure, where $8 \times 8 = 64$ antennas together with a base board (BAB) are combined to an antenna tile. A BAB contains the hardware components to generate and digitize signals in the Tx and Rx channels, respectively. Each BAB contains 8 analog-digital converters (ADCs) that are multiplexed to the 64 antennas and one digital-analog converter (DAC) that is used for all 64 antennas. The previously mentioned SP3T is programmed to connect an antenna to either the Tx or Rx channel. More details on the specific hardware components are given later in this work. In total, 39 antenna tiles are placed around the lysimeter. The 39 antenna tiles are divided into 13 columns and three rings (the lowest

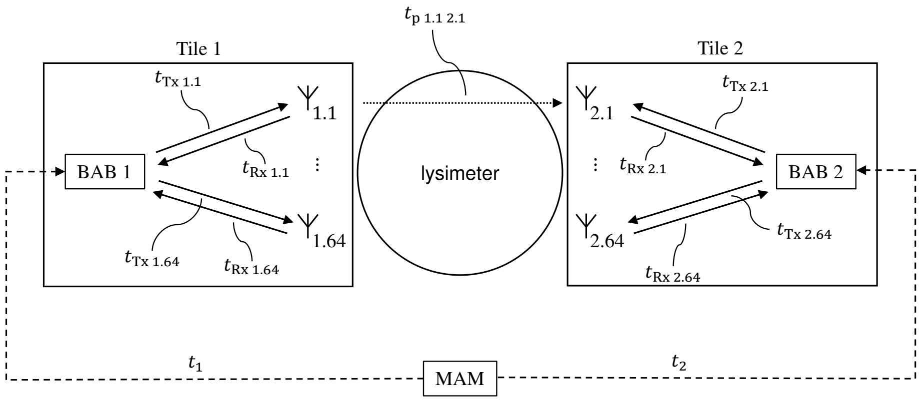

Figure 3.3: Trigger offsets and instrumental delays within the monitoring system.

ring is shown in Fig. 3.2). Each tile is connected to the main module (MAM) via individual trigger, clocking, data and power cables. The tiles on the lowest ring are radially connected to the MAM while the tiles on the upper two rings are chained to the first tile per column. The MAM is responsible for controlling measurements, synchronizing the tiles, collecting data from the BABs and triggering of the tiles to start measurements. To measure a complete tomogram, each of the $39 \cdot 64 = 2496$ antennas once transmits while the other antennas can be used to receive the signal. It will take approximately 10 seconds to complete a tomogram. To derive the calibration for the system in sections 3.3 and 3.4, a detailed understanding of the times within the system is essential (Fig. 3.3). First, the trigger times are defined. The trigger time specifies the time of a digital trigger signal to travel from the MAM to one of the BABs (dashed lines in Fig. 3.3). The trigger signal initializes the corresponding BAB to start a measurement by either activating the transmit (Tx) or receive (Rx) circuit. The trigger times can differ for all 39 BABs due to different cable lengths from MAM to BABs as well as due to manufacturing tolerances of the hardware. Thus, the 39 trigger times are defined as $\boldsymbol{t} = (t_1, ..., t_{39})^{\mathrm{T}}$. Furthermore, within each antenna tile, a distinction is made between Tx and Rx instrumental delays t_{Tx} and t_{Rx} (solid lines). For each of the 64 antennas per antenna tile these instrumental delays can be different. The differences in these instrumental delays come from (i) different micro strip lengths on the printed circuit boards (PCBs), (ii) different cables connecting the BAB to the individual antennas, and from (iii) hardware tolerances of the analog components such as ADCs, amplifiers, connectors and antennas. As notations, $t_{\mathrm{Tx}\,i.n}$ and $t_{\mathrm{Rx}\,i.n}$ are used in the following, where i is the index of the corresponding BAB or tile (1 to 39) and n is the index of the corresponding antenna (1 to 64). The dotted line in Fig. 3.3 marks the signal propagation time $t_{\mathrm{p}\,1.1\,2.1}$ between two antennas, here between antennas 1.1 and 2.1.

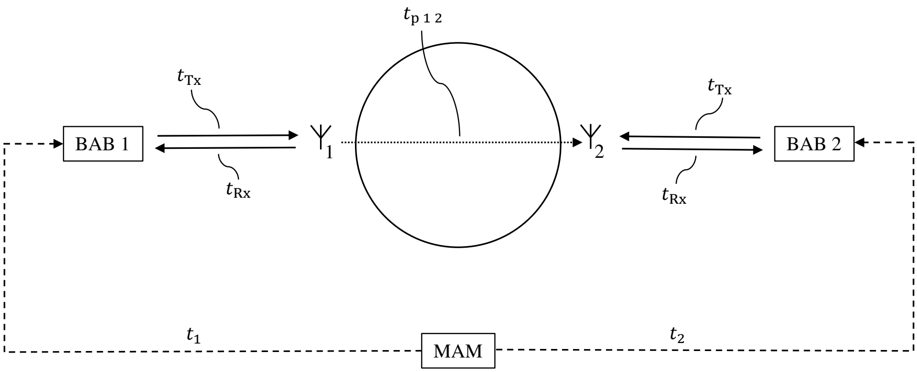

Figure 3.4: Schematic representation of simplified monitoring setup and corresponding instrumental delays.

3.2.2 Simplifications

The system design presented in the previous section proved to be the most flexible solution during the planning phase of the GPR monitoring system. At the beginning of this work, planning was done with an alternative system design consisting of 3000 separate BABs, where each BAB comprises exactly one DAC, one ADC and one antenna. The difference between the originally planned 3000 antennas and the current system with 2500 antennas results from slightly changed system requirements. For this initial system it was assumed that the instrumental delays within the BABs are identical for all BABs. Thus, the previous definition of Tx and Rx instrumental delays simplifies to $t_{\text{Tx}} = t_{\text{Tx}\,i.n}$, $t_{\text{Rx}} = t_{\text{Rx}\,i.n}\,\forall\, i, n$, with no differentiation between the instrumental delays for different BABs. Note that there is only one antenna per BAB ($n = 1$), but a total of $i \leq 3000$ BABs are considered compared to 39 BABs in the current design. For 3000 BABs, $\boldsymbol{t} = (t_1, ..., t_{3000})^T$ defines the trigger times of all BABs. For the following investigations, it is assumed that the 3000 BABs are equally distributed into 120 BABs per ring with 25 rings stacked on top of each other. As before, for an entire tomographic measurement, each BAB is used once to transmit, while the remaining BABs are used to receive the signal.

3.3 Calibration of simplified GPR system

To derive the calibration of the final monitoring system, this thesis starts by developing a calibration approach for the simplified system. This approach will then be extended to be applicable for the final GPR monitoring system.

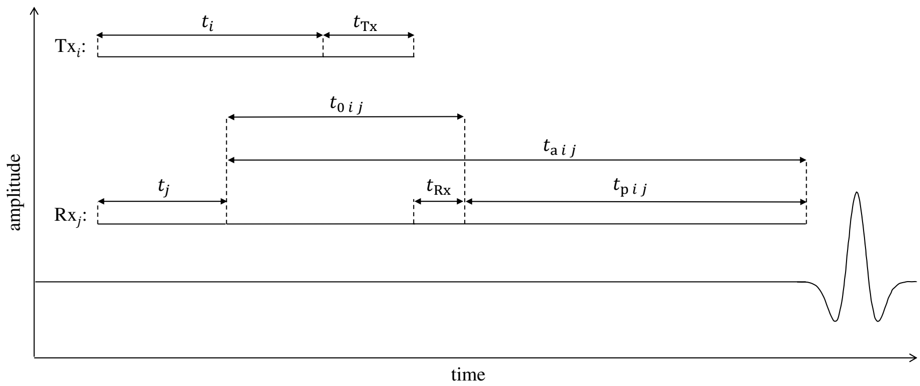

Figure 3.5: Illustration of important times within one measurement.

3.3.1 Preliminary considerations

The fundamental challenge in calibrating the GPR monitoring system is that, on the one hand, the medium between any two antennas is unknown and, on the other hand, the antennas are permanently mounted and cannot be removed from the lysimeter. Therefore, standard calibration procedures as described in section 1.2 cannot be applied. To derive a method for the time-zero correction, a general understanding of the important time segments for a measurement between two BABs i and j is necessary (Fig. 3.5). The time axis starts with the emission of the trigger signal at the MAM. The signal generator of the transmitting BAB i starts at time t_i, while the ADC of the receiving BAB j starts at time t_j. t_{Tx} and t_{Rx} are the instrumental delays and describe the times that a pulse needs to propagate within the complete Tx and Rx circuit, respectively. In Fig. 3.5 the times are rearranged to illustrate the context between time-zero, the trigger times and the instrumental delays of the corresponding BABs. $t_{\mathrm{a}\,i\,j}$ describes the arrival time of the signal when i transmits and j receives. $t_{\mathrm{p}\,i\,j}$ is the propagation time of the signal from the transmitting antenna of BAB i to the receiving antenna of BAB j. Note that the propagation time $t_{\mathrm{p}\,i\,j}$ is initially unknown and cannot be determined without a proper calibration. The gap between t_j and t_{Rx} exemplary illustrates that the data acquisition of BAB j may start before the signal is emitted by BAB i. Note that changing the order of t_{Rx} and $t_{\mathrm{p}\,i\,j}$ does not change the arrival time. Finally, $t_{0\,i\,j}$ is time-zero when i transmits and j receives. Using the definition of $t_0 = t_{\mathrm{a}} - t_{\mathrm{p}}$ with t_{p} as the arbitrary propagation time of the signal between the antennas, it is readily observed from Fig. 3.5 that

$$
\begin{aligned}
t_{0\,i\,j} &= t_i - t_j + t_{\mathrm{Tx}} + t_{\mathrm{Rx}} \\
&= t_{i\,j} + t_{\mathrm{Tx\,Rx}}\,,
\end{aligned}
\tag{3.1}
$$

where

$$t_{ij} := t_i - t_j \tag{3.2}$$

defines the trigger offset of BABs i and j and

$$t_{\mathrm{Tx\,Rx}} := t_{\mathrm{Tx}} + t_{\mathrm{Rx}} \tag{3.3}$$

defines the sum of Tx and Rx instrumental delays. In this equation, time-zero is directly determined by the sum of trigger offsets and instrumental delays instead of derived from a known signal propagation time between any two antennas. The determination of time-zero for any BAB pair requires the knowledge of the difference between the trigger times of the corresponding BABs. The trigger times primarily differ due to different cable lengths to the BABs. For a first calibration approach, the crosstalk of signals between neighboring antennas is used. Between any two antennas, the medium between these antennas is unknown. However, for neighboring BABs, it can be assumed that the signal crosstalk is independent of the ground in the lysimeter and, thus, constant since the antennas are close to each other. If the signal propagation time between neighboring antennas were known, then the classical formula for time-zero correction can be applied to determine time-zero for neighboring BABs. If it is further assumed that t_{Tx} and t_{Rx} are equal and stable for all 3000 BABs, respectively, these times just have to be calibrated once. This is reasonable because within the simplified system design, the BABs are modelled with negligible differences in t_{Tx} and t_{Rx} compared to the trigger times. Then, according to (3.1),

$$t_{ij} = t_{0\,ij} - t_{\mathrm{Tx\,Rx}}$$

yields the trigger offset for neighboring BABs i and j. Furthermore, when k is another neighboring BAB of BAB j, then

$$t_{jk} = t_{0\,jk} - t_{\mathrm{Tx\,Rx}}$$

and finally

$$\begin{aligned} t_{ik} &= t_{ij} + t_{jk} \\ &= t_{0\,ij} + t_{0\,jk} - 2t_{\mathrm{Tx\,Rx}}\,, \end{aligned} \tag{3.4}$$

where i and k are no neighboring BABs. Therefore, for arbitrary BAB pairs, the trigger offsets can be determined via a forward calculation as

$$\boldsymbol{A} \cdot \begin{pmatrix} t_0 \\ t_{\mathrm{Tx\,Rx}} \end{pmatrix} = \boldsymbol{t}\,, \tag{3.5}$$

where $\boldsymbol{A}$ is a suitable matrix to combine the measured time-zeros t_0 of neighboring BABs to calculate any trigger offsets $\boldsymbol{t}$. This calibration concept is also feasible for systems with varying instrumental delays, i.e., $t_{\mathrm{Tx}\,i} \neq t_{\mathrm{Tx}\,j}$ or $t_{\mathrm{Rx}\,i} \neq t_{\mathrm{Rx}\,j}$, as long as these delays are known and stable over time. This allows to connect multiple antennas to the same data acquisition channel as in the tile GPR system. However, in the following, the simplified system is discussed with equal instrumental delays t_{Tx} and t_{Rx} and one Tx/Rx unit per antenna. The approach described by (3.5) has multiple disadvantages. First, the propagation time t_{p} between neighboring BABs needs to be known. This is a challenging task as neighboring antennas operate in each others near-field, which is dominated by capacitive coupling and, therefore, exhibits nonlinear effects. Further, (3.5) suffers from error propagation. BABs that are placed further apart will have larger error variances for the calculated trigger offset. To avoid these disadvantages, a more sophisticated approach termed as pairwise calibration is presented in section 3.3.2.

3.3.2 Pairwise calibration

The pairwise calibration aims to determine the signal propagation time between any two antennas directly. The approach is based on the ability to use any BAB either as Tx or Rx. This allows to conduct reciprocal measurements between any two BABs i and j, yielding

$$\mathrm{Tx}_i, \mathrm{Rx}_j:\; t_i + t_{\mathrm{Tx}} + t_{\mathrm{p}\,i\,j} + t_{\mathrm{Rx}} - t_j = t_{\mathrm{a}\,i\,j} \tag{3.6}$$

$$\mathrm{Tx}_j, \mathrm{Rx}_i:\; t_j + t_{\mathrm{Tx}} + t_{\mathrm{p}\,j\,i} + t_{\mathrm{Rx}} - t_i = t_{\mathrm{a}\,j\,i}\,. \tag{3.7}$$

The term reciprocal measurement always refers to a pair of two measurements as in (3.6) and (3.7). The advantage of reciprocal measurements between two antennas is that the signal propagation time in the time-invariant soil is exactly the same in both directions. This is a direct consequence of the reciprocity of electromagnetic waves (section 2.1.2). As a consequence, the two signal propagation times $t_{\mathrm{p}\,i\,j}$ and $t_{\mathrm{p}\,j\,i}$ to be determined originally can be simplified into one propagation time t_{p}, i.e., $t_{\mathrm{p}} := t_{\mathrm{p}\,i\,j} = t_{\mathrm{p}\,j\,i}$. With this notation, the number of unknown variables is reduced in relation to the number of independent measurements, enabling to uniquely determine the remaining unknown t_{p}. Adding (3.6) and (3.7) and rearranging results in

$$t_{\mathrm{p}} = \frac{t_{\mathrm{a}\,i\,j} + t_{\mathrm{a}\,j\,i}}{2} - t_{\mathrm{Tx\,Rx}}\,. \tag{3.8}$$

This demonstrates that the unknown signal propagation time between i and j through the unknown medium, which usually can only be determined via a calibrated time-zero, is directly determined by conducting a reciprocal measurement as long as the signal delay within the analog circuit, $t_{\mathrm{Tx\,Rx}}$, is known. The advantage of this method is that each individual BAB pair can be calibrated regardless of their position and that $t_{\mathrm{Tx\,Rx}}$ only has to be calibrated once, assuming that it is a constant value for all BAB pairs. Next, an in situ measurement approach to test this prerequisite is established. To detect systematic timing errors, (3.8) is used. This is possible under the condition that t_p is equal for all coupling signals. The term coupling signals is used to refer to signals that propagate between adjacent BABs, more specifically between their respective antennas. If it holds that t_p is equal for all coupling signals, then $t_{\mathrm{a}\,i\,j} + t_{\mathrm{a}\,j\,i}$ in (3.8), where i and j are now adjacent BABs, is equal for all reciprocal measurements as long as $t_{\mathrm{Tx\,Rx}}$ is equal for all BABs. This means that $t_{\mathrm{a}\,i\,j} + t_{\mathrm{a}\,j\,i}$ is a measure to control whether $t_{\mathrm{Tx\,Rx}}$ is equal for all BABs. If, e.g., coupling measurements between BABs 1-2 and 2-3 are conducted, then

$$\frac{t_{\mathrm{a}\,1\,2} + t_{\mathrm{a}\,2\,1}}{2} - t_{\mathrm{Tx\,Rx}} = \frac{t_{\mathrm{a}\,2\,3} + t_{\mathrm{a}\,3\,2}}{2} - t_{\mathrm{Tx\,Rx}} \tag{3.9}$$

as long as t_p is the same for both measurements. A deviation of $t_{\mathrm{a}\,1\,2}+t_{\mathrm{a}\,2\,1}$ and $t_{\mathrm{a}\,2\,3}+t_{\mathrm{a}\,3\,2}$ indicates a violation of the calibration requirement that $t_{\mathrm{Tx\,Rx}}$ is equal for the BABs. This calculation is only valid if the coupling signal propagation time t_p does not depend on the lysimeter filling. This will be further analyzed in subsection 4.2.3. Note that a distinction must be made between three propagation times for coupling signals, namely for horizontal, vertical and diagonal coupling signals. Similar approaches are used in mutual coupling calibrations for phased-array antennas, where phase differences between active antenna elements are of interest [81, 82, 83].

To visualize fast soil changes, fastest possible tomographic measurements are required. In these cases, the pairwise calibration has the disadvantage that each signal trace needs to be included twice in the measurement data to obtain reciprocal measurements. If static soil conditions throughout the measurement are assumed, the reciprocal trace is redundant and increases the measurement time for a complete tomogram. In addition, dynamic irrigation processes might disturb the time invariance of the soil ($t_{\mathrm{p}\,i\,j} \neq t_{\mathrm{p}\,j\,i}$) and would, therefore, lead to erroneous calculations when using (3.8). In contrast, the pairwise calibration is well suited for passive linear time-invariant (LTI) systems that show a reciprocal behavior. In these scenarios, the pairwise calibration should be the method of choice. However, if fast measurements are required, the calibration should be extended or replaced by the following mesh calibration approach.

3.3.3 Mesh calibration

The mesh calibration aims to determine t_p via calibrated time-zero values and is based on a superposition of reciprocal measurements between adjacent BABs. Thereby, the influence of the nearby soil on the signal is minimized in the lysimeter setup. The reciprocal measurements ensure that t_Tx, t_Rx and t_p are eliminated from the following equations and, as described in section 3.3.2, reduce the number of unknown variables. The trigger offset $t_{i\,j}$ between any two BABs is calculated via a superposition of the coupling signals between adjacent BABs. To illustrate this, (3.7) is subtracted from (3.6), which yields

$$t_{i\,j} = \frac{t_{\mathrm{a}\,i\,j} - t_{\mathrm{a}\,j\,i}}{2} \tag{3.10}$$

so that the sought value in (3.1) is obtained by subtracting the known arrival times. Note that only the reciprocity of the medium between the antennas allows to eliminate the unknown signal propagation times between any two antennas. If, e.g., $t_{1\,3}$ should be determined then a first reciprocal measurement is conducted between BABs 1 and 2, whereby 2 is a direct neighbor of 1. Using (3.10), it follows that

$$t_{1\,2} = t_1 - t_2 = \frac{t_{\mathrm{a}\,1\,2} - t_{\mathrm{a}\,2\,1}}{2}\,. \tag{3.11}$$

Continuing the same way with a reciprocal measurement between BABs 2 and 3 yields

$$t_{2\,3} = t_2 - t_3 = \frac{t_{\mathrm{a}\,2\,3} - t_{\mathrm{a}\,3\,2}}{2}\,. \tag{3.12}$$

Adding (3.11) and (3.12) results in

$$t_{1\,3} = t_{1\,2} + t_{2\,3} = t_1 - t_2 + t_2 - t_3 = t_1 - t_3\,. \tag{3.13}$$

This procedure is repeated until any delay time is calculated. Care should be taken that each additional BAB that is used to determine the trigger offset for any two BABs might lead to an error amplification due to inaccurate measurements as already discussed for (3.5). A more sophisticated approach is to define a matrix $\boldsymbol{A}$ such that

$$\boldsymbol{A}\,\boldsymbol{t} = \boldsymbol{t}_{\mathrm{obs}}\,, \tag{3.14}$$

where $\boldsymbol{t}$ are the trigger times of the 3000 BABs, and $\boldsymbol{t}_{\mathrm{obs}}$ is a vector containing the observed trigger offsets of neighboring BABs as in (3.11) and (3.12). Note that $\boldsymbol{A} \in \mathbb{R}^{m\times n}$, where m is the number of measurements and n is the number of BABs. Bold symbols are used to describe matrices and vector quantities. For

$$\boldsymbol{B}\,\boldsymbol{t} = \boldsymbol{t}_{\mathrm{searched}}\,, \tag{3.15}$$

where $\boldsymbol{B}$ defines the sought BAB combinations and $\boldsymbol{t}_{\mathrm{searched}}$ is the vector containing the searched trigger offsets (e.g., $t_{1\,3}$), it follows that

$$\boldsymbol{t}_{\mathrm{searched}} = \boldsymbol{B}\,\boldsymbol{A}^{+}\boldsymbol{t}_{\mathrm{obs}}\,. \tag{3.16}$$

$\boldsymbol{A}^{+}$ denotes the pseudoinverse of $\boldsymbol{A}$, which can be calculated by a QR factorization or singular value decomposition. In general, the aim is to determine

$$\min_{\boldsymbol{t}} ||\boldsymbol{A}\,\boldsymbol{t} - \boldsymbol{t}_{\mathrm{obs}}||_2^2 = \min_{\boldsymbol{t}} r_2^2 \tag{3.17}$$

with $r = ||\boldsymbol{A}\,\boldsymbol{t} - \boldsymbol{t}_{\mathrm{obs}}||$. One solution of 3.17 is given by the normal equation as

$$\frac{\delta r_2^2}{\delta \boldsymbol{t}} = 0 \iff \boldsymbol{A}^{\mathrm{T}}\boldsymbol{A}\,\boldsymbol{t} = \boldsymbol{A}^{\mathrm{T}}\boldsymbol{t}_{\mathrm{obs}} \tag{3.18}$$

which suffers from numerical instabilities when inverting $\boldsymbol{A}^{\mathrm{T}}\boldsymbol{A}$. For the QR factorization, $\boldsymbol{A}$ is written as $\boldsymbol{A} = \boldsymbol{Q}\begin{pmatrix}\boldsymbol{R}\\ \boldsymbol{0}\end{pmatrix}$, where $\boldsymbol{Q}^{\mathrm{T}} = \boldsymbol{Q}^{-1}$ is an orthogonal matrix with $\boldsymbol{Q} \in \mathbb{R}^{m\times m}$, $\boldsymbol{R}$ is an upper triangular matrix with $\boldsymbol{R} \in \mathbb{R}^{n\times n}$, and $\boldsymbol{0}$ is the null matrix to match dimensions. Then, (3.17) is solved as

$$\boldsymbol{Q}^{\mathrm{T}}\, r = \boldsymbol{Q}^{\mathrm{T}}\,\boldsymbol{Q}\begin{pmatrix}\boldsymbol{R}\\ 0\end{pmatrix}\boldsymbol{t} - \boldsymbol{Q}^{\mathrm{T}}\,\boldsymbol{t}_{\mathrm{obs}} = \begin{pmatrix}\boldsymbol{R}\\ 0\end{pmatrix}\boldsymbol{t} - \boldsymbol{Q}^{\mathrm{T}}\,\boldsymbol{t}_{\mathrm{obs}} \tag{3.19}$$

and further

$$r_2^2 = r^{\mathrm{T}}\, r = r^{\mathrm{T}}\,\boldsymbol{Q}\,\boldsymbol{Q}^{\mathrm{T}}\, r = \left(\begin{pmatrix}\boldsymbol{R}\\ 0\end{pmatrix}\boldsymbol{t} - \boldsymbol{Q}^{\mathrm{T}}\,\boldsymbol{t}_{\mathrm{obs}}\right)^{\mathrm{T}}\left(\begin{pmatrix}\boldsymbol{R}\\ 0\end{pmatrix}\boldsymbol{t} - \boldsymbol{Q}^{\mathrm{T}}\,\boldsymbol{t}_{\mathrm{obs}}\right), \tag{3.20}$$

which is minimized with respect to $\boldsymbol{t}$ when

$$\boldsymbol{R}\,\boldsymbol{t} = (\boldsymbol{Q}^{\mathrm{T}})_n\,\boldsymbol{t}_{\mathrm{obs}}\,, \tag{3.21}$$

where $(\boldsymbol{Q}^{\mathrm{T}})_n$ denotes the first n rows of $\boldsymbol{Q}^{\mathrm{T}}$. Consequently, $\boldsymbol{A}^{+} = \boldsymbol{R}^{-1}\,(\boldsymbol{Q}^{\mathrm{T}})_n$. Note that $\boldsymbol{R}^{-1}$ and $(\boldsymbol{Q}^{\mathrm{T}})_n$ only have to be calculated once if A keeps constant for multiple measurements of $\boldsymbol{t}_{\mathrm{obs}}$. The calculation of (3.17) via the QR decomposition has the advantage that it is numerically more stable than the calculation via (3.18).

Using the matrices $\boldsymbol{A}$ and $\boldsymbol{B}$ allows to determine any trigger offsets based on coupling measurements. This approach is similar to the approach of Xu et al. (1993) [92], who use the superposition of a primary data set to synthesize resistivity data for arbitrary measurement configurations. The innovative part here is that only the reciprocal measurements allow the setup of a solvable system of equations. Finally, the signal propagation time between any BABs i and j is determined as

$$\begin{aligned} t_{\mathrm{p}} &= t_{\mathrm{a}\,i\,j} - \boldsymbol{B}\,R^{-1}\,(\boldsymbol{Q}^{\mathrm{T}})_n\,\boldsymbol{t}_{\mathrm{obs}} - t_{\mathrm{Tx\,Rx}} \\ &= t_{\mathrm{a}\,i\,j} - t_{0\,i\,j}. \end{aligned} \tag{3.22}$$

with corresponding matrix $\boldsymbol{B}$. Note that the usage of coupling signals for the calibration does not require additional measurements to be performed during a tomography, since every BAB is once used as Tx for a complete tomography. The only additional effort is to use neighboring BABs of a transmitter as receivers. The mesh calibration can be performed before irrigation processes to obtain a time-zero correction based on (3.1) for any two BABs. When the soil then experiences fast changes, it is sufficient to use a reduced number of receivers to speed up the measurement. In contrast to the pairwise calibration method, calibration data for the mesh calibration, i.e., trigger offsets, only need to be determined once or after a specific period of time to re-calibrate the system. Lastly, this approach does not rely on coupling measurements between neighboring BABs. The system of linear equations can be constructed using any combination of reciprocal measurements as long as all BABs are connected. However, if the assumption from section 3.3.1 is correct that for adjacent antennas t_0 can be calculated directly with a known t_p, the following approach is also possible: it is assumed that i and j are adjacent BABs, while k can be at any position on the lysimeter. Since $t_{0\,i\,j} = t_{i\,j} + t_{\mathrm{Tx\,Rx}} = t_i - t_j + t_{\mathrm{Tx\,Rx}}$, it follows that

$$t_{0\,i\,k} = t_i - t_j + t_j - t_k + t_{\mathrm{Tx\,Rx}} = t_{0\,i\,j} + t_{i\,k}\,. \tag{3.23}$$

Thus, if $t_{0\,i\,j}$ can be determined from a direct measurement, again (3.16) can be used to calculate $t_{i\,k}$. In this case, the instrumental delays $t_{\mathrm{Tx\,Rx}}$ would not need to be known, but only identical for all BABs to determine any time-zero.

3.3.4 Random timing errors

The consideration of timing errors is important for both, the pairwise and mesh calibration. A distinction is made between two kinds of timing error sources, namely systematic and random differences between t_Tx and t_Rx for different BABs. The impact of random errors is reduced by stacking the signals, i.e.,

$$\frac{1}{n}\sum_{i=1}^{n} \xi_i \sim N(0, \frac{\eta^2}{n})\,, \tag{3.24}$$

where ξ_i is the normal distributed random error variable for measurement i with zero mean and standard deviation η and the ξ_i's are independent and identically distributed. Systematic differences are unaffected by stacking. The ability to measure the trigger offsets of BABs based on reciprocal measurements as in (3.10) relies on equal instrumental delays t_Tx and t_Rx. Any inequalities of instrumental delays would result in systematic errors for both, the pairwise and mesh calibration. Here, the effects of random timing errors on the trigger offsets are analyzed by means of simulations. Three possible measurement topologies for reciprocal measurements between adjacent BABs to construct

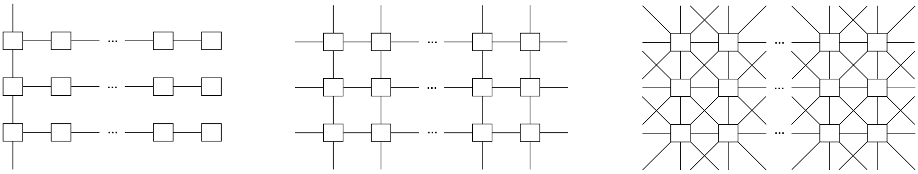

(a) Mesh2 (b) Mesh4 (c) Mesh8

Figure 3.6: Three possible topologies to perform reciprocal measurements only between adjacent BABs.

the matrix $\boldsymbol{A}$ are depicted in Fig. 3.6. Each square represents one BAB and each line connecting two squares represents a measured trigger offset between the corresponding BABs. For Mesh2, each BAB performs a reciprocal measurement with its left and right neighbor (except for the last BAB per ring), creating rows of connected BABs. To connect two rows, two vertical neighboring BABs perform a reciprocal measurement (Fig. 3.6a). For Mesh4, each BAB performs a reciprocal measurement with its left, right, upper and lower adjacent BAB (Fig. 3.6b). For Mesh8, the four diagonal neighbors are used additionally to those of Mesh4 (Fig. 3.6c). While the usage of Mesh2 is sufficient to solve (3.16), Mesh4 and Mesh8 are introduced to reduce the influence of jitter by utilizing a larger system of linear equations. The 3000 BABs are separated into 120 columns around the lysimeter and 25 rings on top of each other (see section 3.2.2). Equations (3.25) and (3.26) are used to implement random error effects:

$$t_i + t_{\mathrm{Tx}} + \xi_{i\,\mathrm{Tx}} + t_{\mathrm{p}\,i\,j} + t_{\mathrm{Rx}} + \xi_{j\,\mathrm{Rx}} - t_j = t_{\mathrm{a}\,i\,j} \tag{3.25}$$

and

$$t_j + t_{\mathrm{Tx}} + \xi_{j\,\mathrm{Tx}} + t_{\mathrm{p}\,j\,i} + t_{\mathrm{Rx}} + \xi_{i\,\mathrm{Rx}} - t_i = t_{\mathrm{a}\,j\,i}, \tag{3.26}$$

where ξ_i and $\xi_j \sim N(0, \eta^2)$ represent random errors that are introduced by BABs i and j either as Tx or as Rx. Subtracting the erroneous measurements (3.25) and (3.26) and rearranging yields

$$t_{i\,j} + \underbrace{\frac{\xi_{i\,\mathrm{Tx}} - \xi_{j\,\mathrm{Tx}} + \xi_{j\,\mathrm{Rx}} - \xi_{i\,\mathrm{Rx}}}{2}}_{\xi_{i\,j}} = \underbrace{\frac{t_{\mathrm{a}\,i\,j} - t_{\mathrm{a}\,j\,i}}{2}}_{\tilde{t}_{i\,j}} \tag{3.27}$$

where $\xi_{i\,j}$ is a new random variable with $\xi_{i\,j} \sim N(0, \eta^2)$ following the properties of normal distributed random variables. Therefore, the true trigger offsets $\boldsymbol{t}_{\mathrm{obs}}$ in (3.16) are replaced by measures

$$\tilde{\boldsymbol{t}}_{\mathrm{obs}} = \boldsymbol{t}_{\mathrm{obs}} + \boldsymbol{\xi}\,. \tag{3.28}$$

Elements in the error vector $\boldsymbol{\xi} \sim N(0, \Sigma_\xi)$ are not necessarily independent, because when one BAB transmits and multiple BABs receive, then an error in t_{Tx} affects all receivers. Equation (3.28) is used as the right-hand side in (3.21) to implement the mathematical model of the simulation (sections 4.1.1 and 4.2.1). The same calculation can be done for the summation of erroneous reciprocal measurements as it is required for the pairwise calibration, which again leads to an error term $\xi_{ij} \sim N(0, \eta^2)$:

$$t_{\mathrm{p}} = \frac{t_{\mathrm{a\,ij}} + t_{\mathrm{a\,ji}}}{2} - t_{\mathrm{Tx\,Rx}} - \underbrace{\frac{\xi_{i\,\mathrm{Tx}} + \xi_{j\,\mathrm{Tx}} + \xi_{i\,\mathrm{Rx}} + \xi_{j\,\mathrm{Rx}}}{2}}_{\xi_{ij}} . \tag{3.29}$$

It follows that the pairwise calibration exhibits the standard deviation of a single measurement η, which can be reduced by repetitive measurements, i.e., stacking. A stacking factor s would finally reduce the random errors standard deviation by a factor of $\sqrt{s}$ which is also true for the mesh calibration. Besides stacking the data by repeating the measurements to obtain $\tilde{\boldsymbol{t}}_{\mathrm{obs}}$, random errors are furthermore reduced by performing reciprocal measurements between as many neighboring BABs as possible. This can be seen in the condition number $\kappa_2(\boldsymbol{A})$, where $\kappa_2(\boldsymbol{A})$ is defined as

$$\kappa_2(\boldsymbol{A}) = \frac{\sigma_{\max}(\boldsymbol{A})}{\sigma_{\min}(\boldsymbol{A})}$$

with $\sigma_{\max}(\boldsymbol{A})$ and $\sigma_{\min}(\boldsymbol{A})$ as the largest and smallest singular value of $\boldsymbol{A}$, respectively. The condition number can be used to estimate the effect of measurement error on the optimal solution of (3.17), since the following relationship holds:

$$\frac{||\tilde{\boldsymbol{t}} - \boldsymbol{t}||_2}{||\boldsymbol{t}||_2} \leq \kappa_2(\boldsymbol{A}) \frac{||\xi||_2}{||\boldsymbol{t}_{\mathrm{obs}}||_2}$$

where $\tilde{\boldsymbol{t}}$ is the optimal solution with respect to the used norm for disturbed input values $\tilde{\boldsymbol{t}}_{\mathrm{obs}}$. For the three sample meshes A_2, A_4, and A_8 from Fig. 3.6 one gets

$$\kappa_2(\boldsymbol{A}_2) = 260.47$$
$$\kappa_2(\boldsymbol{A}_4) = 53.97$$
$$\kappa_2(\boldsymbol{A}_8) = 38.69$$

which shows that for the largest of the three meshes, measurement errors have the least impact on the optimization result. For the theoretically largest possible mesh A_{2999}, each BAB would perform a reciprocal measurement with the remaining 2999 BABs, resulting in a condition number close to 1. However, due to the large memory requirements of A_{2999} and the computationally intensive QR decomposition, other solution approaches for (3.16) would have to be used such as the iterative LSQR algorithm [93]. However, this will not be pursued further in this work. Finally, an estimate for the covariances of $r = \boldsymbol{t}_{\text{obs}} - \tilde{\boldsymbol{t}}_{\text{obs}} = \boldsymbol{A}^{+}\xi$ is given. For the covariance matrix Σ_r of r holds

$$\begin{aligned}\Sigma_r &= \mathrm{E}[(r-\bar{r})(r-\bar{r})^T] \\ &= \mathrm{E}[(\boldsymbol{A}^{+}\xi)(\boldsymbol{A}^{+}\xi)^T] \\ &= \mathrm{E}[\boldsymbol{A}^{+}\xi\xi^T A^{+^T}] \\ &= \boldsymbol{A}^{+}\Sigma_\xi \boldsymbol{A}^{+^T}. \end{aligned} \tag{3.30}$$

As previously mentioned, the elements of ξ are not necessarily independent and, therefore, $\Sigma_\xi \neq \eta^2 \boldsymbol{I}$ where $\boldsymbol{I}$ denotes the identity matrix. However, for this analysis, it is assumed that $\Sigma_\xi \approx \eta^2 \boldsymbol{I}$. Then, $\Sigma_r \approx \eta^2 \boldsymbol{A}^{+}\boldsymbol{A}^{+^\mathrm{T}}$, i.e., $\boldsymbol{A}^{+}\boldsymbol{A}^{+^\mathrm{T}}$ determines how the single measurement error variance η^2 transfers to the error of the obtained trigger times. With the singular value decomposition $\boldsymbol{A} = \boldsymbol{U}\,\boldsymbol{S}\,\boldsymbol{V}^\mathrm{T}$ holds $\boldsymbol{A}^{+} = \boldsymbol{V}\,\boldsymbol{S}^{+}\,\boldsymbol{U}^\mathrm{T}$ and, therefore,

$$\boldsymbol{A}^{+}\boldsymbol{A}^{+^\mathrm{T}} = \boldsymbol{V}\,\boldsymbol{S}^{+}\,\boldsymbol{U}^\mathrm{T}\,(\boldsymbol{V}\,\boldsymbol{S}^{+}\,\boldsymbol{U}^\mathrm{T})^T = \boldsymbol{V}\,\boldsymbol{S}^{+}\,\boldsymbol{S}^{+^\mathrm{T}}\,\boldsymbol{V}^\mathrm{T}, \tag{3.31}$$

where the pseudoinverse $\boldsymbol{S}^{+}$ can be computed by inversing the diagonal elements of $\boldsymbol{S}$. The approximated covariance matrices $\boldsymbol{A}^{+}\boldsymbol{A}^{+^\mathrm{T}}$ for the three meshes are shown in Fig. 3.7a, 3.7c, 3.7e. Values less than 1 indicate that the original error variance η^2 is reduced by the inversion. In addition, the diagonal elements of $\boldsymbol{A}^{+}\boldsymbol{A}^{+^\mathrm{T}}$, i.e., the variances of r are shown (Fig. 3.7b, 3.7d, 3.7f). For Mesh2 all approximated covariances on the main diagonal are greater than 1, so that the error variance is not reduced by the inversion. While for Mesh4 the BABs in the top four and bottom four rings still have an error variance greater than 1, for Mesh8 a continuous variance less than 1 can be achieved.

3.4 Calibration of tile GPR system

For the simplified system design, it was assumed that $t_{\text{Tx Rx}}$ is identical for all BABs. However, based on the system design presented in section 3.2.1, it must be assumed that these times differ for different antennas. Therefore, approaches are presented in this section with which the calibration can also be performed with varying instrumental delays. Hence, (3.1) becomes

$$t_{0\,i.m\,j.n} = t_{i\,j} + t_{\text{Tx}\,i.m} + t_{\text{Rx}\,j.n}\,, \tag{3.32}$$

where variations between the Tx and Rx instrumental delays $t_{\text{Tx}\,i.m}$ and $t_{\text{Rx}\,j.n}$ are taken into account. The indices i and j indicate the corresponding BABs ($1 \leq i, j \leq 39$), while m and n denote the corresponding antennas within the antenna arrays ($1 \leq m, n \leq 64$).

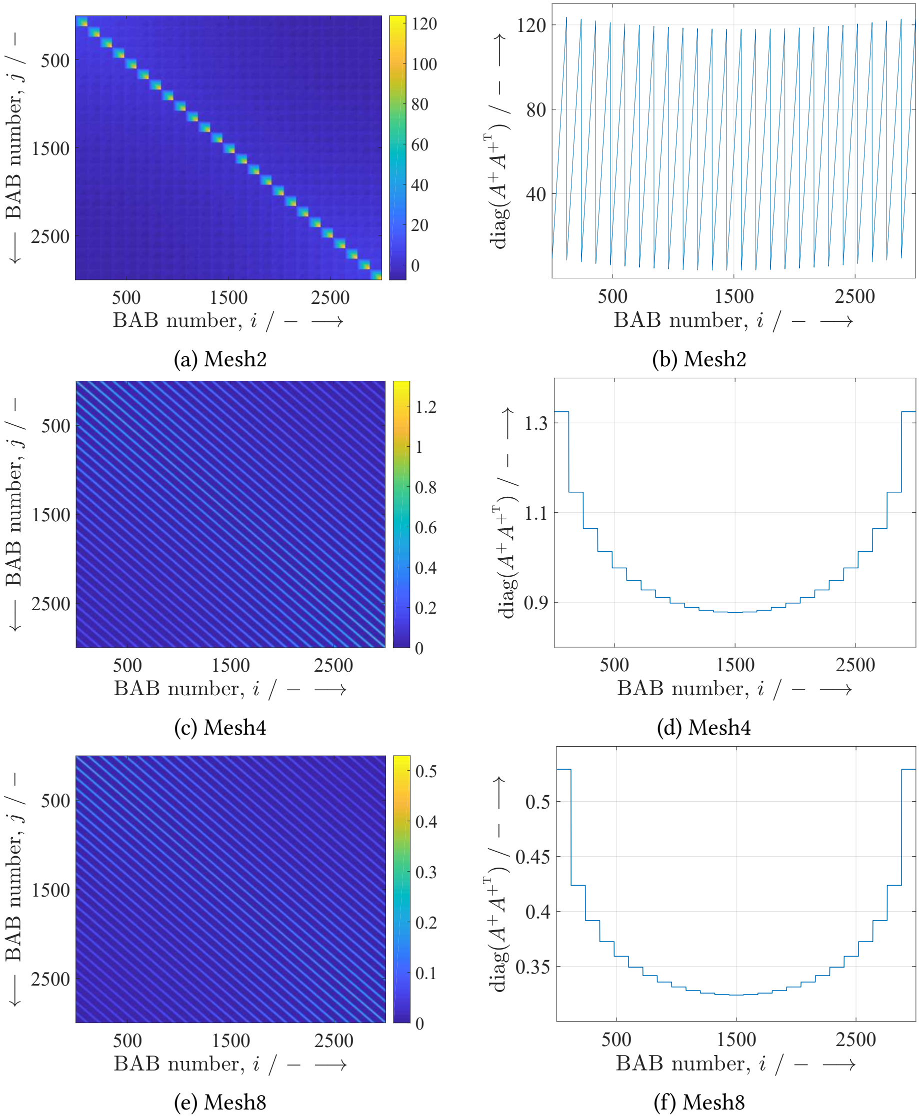

Figure 3.7: Covariance matrices for mesh topologies ((a), (c) and (e)) and diagonal covariance elements ((b), (d), (f)).

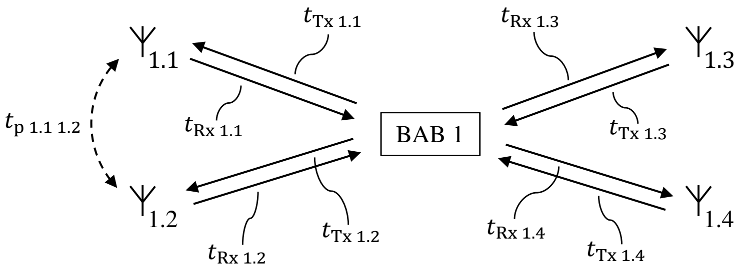

Figure 3.8: Reduced 2x2 array to illustrate the calibration concept.

3.4.1 Preliminary considerations

For a first approach, an attempt is made to determine the instrumental delays $t_{\mathrm{Tx}\,i.m}$ and $t_{\mathrm{Rx}\,j.n}$ on each BAB, so that in a second step the approach according to (3.21) can be applied. To calculate the trigger offsets of two BABs, either a reciprocal measurement between any two antennas on the respective BABs can be performed, or multiple reciprocal measurements between multiple antennas can be performed to achieve an averaging of the trigger offset. First, it is investigated whether all instrumental delays on a BAB can be determined by measurements between the antennas on this BAB. For this purpose, a minimal example is used, where only four antennas are arranged in a 2×2 array (Fig. 3.8). The approaches can then be scaled to the actual 8×8 array. The aim is to determine the eight instrumental delays $t_{\mathrm{Tx}\,1.1}, \ldots, t_{\mathrm{Tx}\,1.4}, t_{\mathrm{Rx}\,1.1}, \ldots, t_{\mathrm{Rx}\,1.4}$. For this purpose, measurements are first performed between adjacent antennas, e.g.,

$$t_{\mathrm{Tx}\,1.1} + t_{\mathrm{p}\,1.1\,1.2} + t_{\mathrm{Rx}\,1.2} = t_{\mathrm{a}\,1.1\,1.2} \Leftrightarrow t_{\mathrm{Tx}\,1.1} + t_{\mathrm{Rx}\,1.2} = t_{\mathrm{a}\,1.1\,1.2} - t_{\mathrm{p}\,1.1\,1.2} \tag{3.33}$$
$$t_{\mathrm{Tx}\,1.2} + t_{\mathrm{p}\,1.2\,1.1} + t_{\mathrm{Rx}\,1.1} = t_{\mathrm{a}\,1.2\,1.1} \Leftrightarrow t_{\mathrm{Tx}\,1.2} + t_{\mathrm{Rx}\,1.1} = t_{\mathrm{a}\,1.2\,1.1} - t_{\mathrm{p}\,1.2\,1.1} \tag{3.34}$$

for antennas 1 and 2 on BAB 1. For a known t_{p} between neighboring antennas, it follows that

$$\underbrace{\begin{pmatrix} 1 & 0 & 0 & 1 \\ 0 & 1 & 1 & 0 \end{pmatrix}}_{M_1} \begin{pmatrix} t_{\mathrm{Tx}\,1.1} \\ t_{\mathrm{Tx}\,1.2} \\ t_{\mathrm{Rx}\,1.1} \\ t_{\mathrm{Rx}\,1.2} \end{pmatrix} = \begin{pmatrix} t_{\mathrm{a}\,1.1\,1.2} - t_{\mathrm{p}\,1.1\,1.2} \\ t_{\mathrm{a}\,1.2\,1.1} - t_{\mathrm{p}\,1.2\,1.1} \end{pmatrix} \tag{3.35}$$

with $\mathrm{rank}(M_1) = 2$. Without the assumption of a known t_{p} between neighboring antennas, according to reciprocity and for (3.33) - (3.34) it holds that

$$\underbrace{\begin{pmatrix} 1 & -1 & -1 & 1 \end{pmatrix}}_{M_2} \begin{pmatrix} t_{\mathrm{Tx}\,1.1} \\ t_{\mathrm{Tx}\,1.2} \\ t_{\mathrm{Rx}\,1.1} \\ t_{\mathrm{Rx}\,1.2} \end{pmatrix} = \begin{pmatrix} t_{\mathrm{a}\,1.1\,1.2} - t_{\mathrm{a}\,1.2\,1.1} \end{pmatrix} \tag{3.36}$$

with $\mathrm{rank}(M_2) = 1$. If the approach from (3.36) is applied to all six possible reciprocal measurements between pairs of antennas, it follows that

$$\underbrace{\begin{pmatrix} 1 & -1 & 0 & 0 & -1 & 1 & 0 & 0 \\ 1 & 0 & -1 & 0 & -1 & 0 & 1 & 0 \\ 1 & 0 & 0 & -1 & -1 & 0 & 0 & 1 \\ 0 & 1 & -1 & 0 & 0 & -1 & 1 & 0 \\ 0 & 1 & 0 & -1 & 0 & -1 & 0 & 1 \\ 0 & 0 & 1 & -1 & 0 & 0 & -1 & 1 \end{pmatrix}}_{M_3} \begin{pmatrix} t_{\mathrm{Tx}\,1.1} \\ t_{\mathrm{Tx}\,1.2} \\ t_{\mathrm{Tx}\,1.3} \\ t_{\mathrm{Tx}\,1.4} \\ t_{\mathrm{Rx}\,1.1} \\ t_{\mathrm{Rx}\,1.2} \\ t_{\mathrm{Rx}\,1.3} \\ t_{\mathrm{Rx}\,1.4} \end{pmatrix} = t_{\mathrm{a}} \tag{3.37}$$

with $\mathrm{rank}(M_3) = 3$ for eight unknown instrumental delays. This shows that the exclusive use of reciprocal measurements provides not enough information to uniquely determine the instrumental delays on a BAB. Consequently, additional information is needed, which can be obtained, for example, by direct measurement of instrumental delays, similar to the calibration of synthetic aperture radar (SAR) systems [77]. However, this approach requires additional hardware, which in turn must be very well characterized. Instead, at this point we shall first assume that the system is capable of performing so-called internal reflection measurements. For antenna 1.1 this would lead to the measurement of

$$t_{\mathrm{Tx}\,1.1} + t_{\mathrm{Rx}\,1.1} = t_{\mathrm{a}\,1.1\,1.1}\,, \tag{3.38}$$

where the measurement is not made between different antennas, but where a reflection from the transmitting antenna is measured. When such internal reflection measurements for all four antennas on the minimal example are combined with reciprocal measurements between the antenna pairs 1.1-1.2, 1.1-1.3 and 1.1-1.4, one gets

$$\underbrace{\begin{pmatrix} 1 & -1 & 0 & 0 & -1 & 1 & 0 & 0 \\ 1 & 0 & -1 & 0 & -1 & 0 & 1 & 0 \\ 1 & 0 & 0 & -1 & -1 & 0 & 0 & 1 \\ 1 & 0 & 0 & 0 & 1 & 0 & 0 & 0 \\ 0 & 1 & 0 & 0 & 0 & 1 & 0 & 0 \\ 0 & 0 & 1 & 0 & 0 & 0 & 1 & 0 \\ 0 & 0 & 0 & 1 & 0 & 0 & 0 & 1 \end{pmatrix}}_{M_4} \begin{pmatrix} t_{\mathrm{Tx}\,1.1} \\ t_{\mathrm{Tx}\,1.2} \\ t_{\mathrm{Tx}\,1.3} \\ t_{\mathrm{Tx}\,1.4} \\ t_{\mathrm{Rx}\,1.1} \\ t_{\mathrm{Rx}\,1.2} \\ t_{\mathrm{Rx}\,1.3} \\ t_{\mathrm{Rx}\,1.4} \end{pmatrix} = t_{\mathrm{a}}\,. \tag{3.39}$$

Here $\mathrm{rank}(M_4) = 7$, so it is still an underdetermined system of equations. In general, for n antennas and consequently $2n$ unknown instrumental delays, n internal reflection measurements and $n-1$ linearly independent reciprocal measurements can be performed, so that a rank deficit of 1 always results. Thus, the instrumental delays cannot be determined uniquely. Nevertheless, to obtain realistic values for the analog times, two approaches can be followed: (i) use of a numerical optimization method with a-priori information about the instrumental delays or (ii) one instrumental delay must be known exactly to resolve the rank deficit. For (i), it must be argued how this a-priori information might look like, e.g., whether suitable starting parameters can be determined and how further restrictions might look like. For example, it could be assumed that the Tx and Rx instrumental delays may only differ from each other within a certain range. However, this would require more information about the temporal stability of the system.

For (ii), a possible approach could be that, in addition to the internal reflection measurement, further measurements are performed with additional microstrip lines with known propagation times. For this purpose, the analogue part of the system consisting of ADC, DAC, components in the Tx and Rx channel and an antenna is considered as an example with $t_{\mathrm{Tx}} = t_{\mathrm{DAC}} + \hat{t}_{\mathrm{Tx}}$ and $t_{\mathrm{Rx}} = t_{\mathrm{ADC}} + \hat{t}_{\mathrm{Rx}}$ (Fig. 3.9, $\hat{t}_{\mathrm{Tx}}$ and $\hat{t}_{\mathrm{Rx}}$ in grey). Low-noise amplifier (LNA) and multiplexer (MUX), among other components in the actual Tx and Rx channels, are active components with potentially changing characteristics and variations between individual components, respectively. Thus, t_{Tx} is composed of all internal DAC times and the signal propagation time between DAC output and, e.g., a directional coupler, whereas t_{Rx} is composed of all internal ADC times and the signal propagation time between antenna input and directional coupler. Then

$$t_{\mathrm{DAC}} + t_{\mathrm{known\,1}} + t_{\mathrm{ADC}} = t_{\mathrm{a\,1}} \Leftrightarrow t_{\mathrm{DAC}} + t_{\mathrm{ADC}} = t_{\mathrm{a\,1}} - t_{\mathrm{known\,1}} \tag{3.40}$$

and

$$t_{\mathrm{DAC}} + \hat{t}_{\mathrm{Tx}} + t_{\mathrm{known\,2}} + t_{\mathrm{ADC}} = t_{\mathrm{a\,2}} \Leftrightarrow \hat{t}_{\mathrm{Tx}} \overset{(3.40)}{=} t_{\mathrm{a\,2}} - t_{\mathrm{known\,2}} - (t_{\mathrm{a\,1}} - t_{\mathrm{known\,1}}) \tag{3.41}$$

where the times $t_{\mathrm{known\,1}}$ and $t_{\mathrm{known\,2}}$ are assumed to be known and are implemented, for example, via directional couplers together with microstrip lines or cables of known length, width and permittivity. In addition, these runtimes would have to be well characterised to be able to react appropriately to changing environmental conditions such as temperature changes. Then, this setup makes $\hat{t}_{\mathrm{Tx}}$ directly available by bypassing the Rx channel of an arbitrary antenna. However, the true t_{Tx} is still not identifiable as the internal DAC times remain unknown. Only if $t_{\mathrm{DAC}} + t_{\mathrm{ADC}}$ is identical for all BABs, this approach can be utilized as the measured time can be used for all antenna combinations. Consequently, in the previous equations t_{Tx} and t_{Rx} could be substituted by $\hat{t}_{\mathrm{Tx}}$ and $\hat{t}_{\mathrm{Rx}}$. In addition, another directional coupler would have to be positioned as close as possible to the antenna to cover as much signal path from the Tx and Rx channels as possible. In summary, for this approach, additional hardware would have to be installed for calibration and a laborious characterisation of the signal propagation times on specific lines would have to be carried out. The internal reflection measurements can nevertheless be

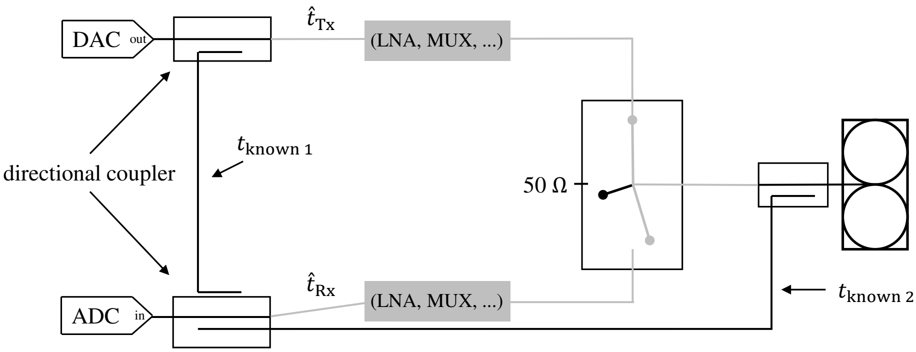

Figure 3.9: Illustration of known signal propagation times for one antenna on a BAB.

used to determine a unique time-zero. A complete description of this approach and how the internal reflection measurements can be implemented in detail will be presented in section 3.4.2.

3.4.2 Internal reflection measurements

So far, attempts have been made to apply the mesh calibration of the simplified GPR system (section 3.3.3) to the tile GPR system (section 3.4.1). This implies that the instrumental delays t_{Tx} and t_{Rx} must be determined for each antenna. However, without considerable additional effort for the characterisation of individual propagation times not enough information can be provided via measurements to uniquely determine the instrumental delays. Instead, in the following, the pairwise calibration introduced in section 3.3.2 is extended for the calibration of the tile GPR system. For illustration of this extended pairwise calibration approach, the following equations are simplified for a distinct antenna combination (antennas 1.1 and 2.1) that is shown in Fig. 3.3. Note that all other antenna combinations can be calibrated in the same way. The signal arrival time for this setup from the point of view of the ADC connected to antenna 1 on BAB2, i.e. $t_{a\,1.1\,2.1}$, is determined by adding all partial times of a measurement:

$$t_1 + t_{Tx\,1.1} + t_{p\,1.1\,2.1} + t_{Rx\,2.1} - t_2 = t_{a\,1.1\,2.1}\,, \tag{3.42}$$

where $t_{p\,1.1\,2.1}$ represents the signal propagation time between the antennas through the soil. Subsequently, when a reciprocal measurement is performed, i.e., antenna 1 on BAB1 is Rx and antenna 1 on BAB2 is Tx, it follows that

$$t_2 + t_{Tx\,2.1} + t_{p\,2.1\,1.1} + t_{Rx\,1.1} - t_1 = t_{a\,2.1\,1.1}\,, \tag{3.43}$$

where $t_{\mathrm{a}\,2.1\,1.1}$ is now the relative arrival time of the signal at the ADC on BAB1. Subtracting (3.42) and (3.43) and rearranging for the trigger offset $t_{1\,2}$ yields

$$t_{1\,2} = \frac{t_{\mathrm{a}\,1.1\,2.1} - t_{\mathrm{a}\,2.1\,1.1}}{2} + \frac{t_{\mathrm{Rx}\,1.1} - t_{\mathrm{Tx}\,1.1} + t_{\mathrm{Tx}\,2.1} - t_{\mathrm{Rx}\,2.1}}{2} \tag{3.44}$$

and eliminates the unknown signal propagation time between the antennas due to the reciprocity of electromagnetic waves in an LTI medium. Substituting (3.44) in (3.32) finally gives

$$t_{0\,1.1\,2.1} = \frac{t_{\mathrm{a}\,1.1\,2.1} - t_{\mathrm{a}\,2.1\,1.1}}{2} + \frac{t_{\mathrm{Tx}\,1.1} + t_{\mathrm{Rx}\,1.1}}{2} + \frac{t_{\mathrm{Tx}\,2.1} + t_{\mathrm{Rx}\,2.1}}{2}\,. \tag{3.45}$$

Equation (3.45) shows that the sum of Tx and Rx instrumental delays for the involved antennas, i.e., $t_{\mathrm{Tx}\,1.1} + t_{\mathrm{Rx}\,1.1}$ and $t_{\mathrm{Tx}\,2.1} + t_{\mathrm{Rx}\,2.1}$, together with reciprocal measurements yields the necessary information to perform the time-zero calibration. The sum of Tx and Rx instrumental delays is obtained by utilizing internal parasitic reflections from the antenna back into the system as described by (3.38). These measurements yield, e.g.,

$$t_{\mathrm{Tx}\,1.1} + t_{\mathrm{Rx}\,1.1} = t_{\mathrm{a}\,1.1\,1.1} \tag{3.46}$$

and

$$t_{\mathrm{Tx}\,2.1} + t_{\mathrm{Rx}\,2.1} = t_{\mathrm{a}\,2.1\,2.1} \tag{3.47}$$

which are the arrival times of signals passing through the complete Tx and Rx circuit up to an individual antenna. Hence, time-zero can directly be determined by combining (3.45), (3.46) and (3.47). To understand the functionality of internal reflection measurements, the design of an antenna tile is described in detail (Fig. 3.10). The main elements of an antenna tile are a DAC for signal generation, amplifiers, two 1-to-8 switches (SP8T, Fig. 3.10 just shows one), one SP3T for each antenna to control the mode of an antenna (Tx, Rx or terminated), the antennas and finally an ADC for digitizing measured signals. The Tx circuit includes the DAC, one amplifier and switches, whereas the Rx circuit includes the ADC, two amplifiers and switches. Numbers (3) and (4) mark the Tx and Rx signal ports, respectively. For illustration, only one Tx/Rx circuit (numbers (1) and (2)) with SP3T (5a) and antenna port (6a) is shown entirely. The operation of the presented method is explained exemplary with the SP3T in Tx mode as in Fig. 3.10. Arrows indicate the signal propagation channels. When an antenna is used for transmission, a signal, i.e., a Ricker wavelet with f_c = 750 MHz, is generated in a DAC. Once the

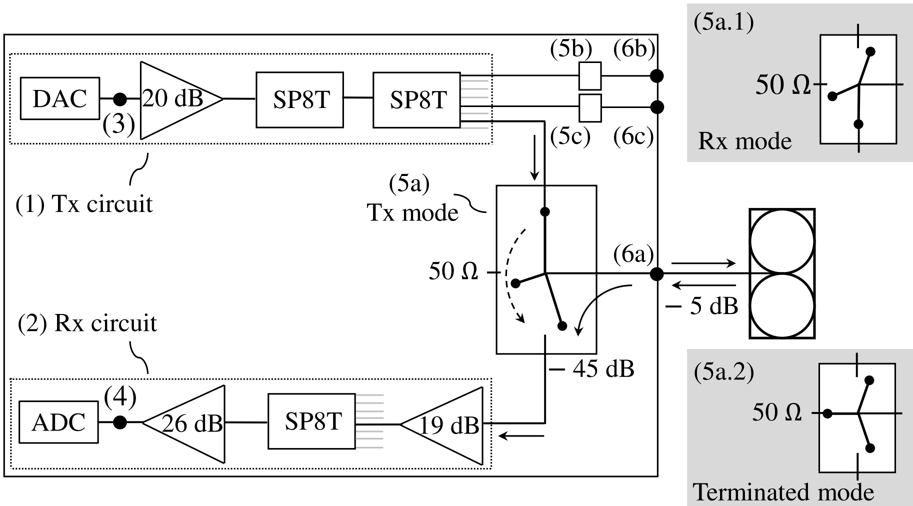

Figure 3.10: Simplified layout of an antenna tile with BAB and antenna in Tx mode.

generated signal reaches the SP3T, most of the energy is directed to the antenna. Due to a limited isolation of the switch (about -45 dB), a coupling onto the deactivated Rx circuit of the antenna tile occurs at the same time. Most of the signal traveling further to the antenna is radiated into the lysimeter. Due to the broadband characteristics of the transmitted Ricker wavelet and the limited impedance matching of the antenna for that broad frequency range, portions of the signal are reflected at the antenna, specifically at the antenna feed point, and travel back to the SP3T. Thereby, a second coupling over to the Rx circuit occurs. Both coupling signals are amplified and finally measured at the ADC. The relevant signal for this work is the second coupling, since this signal contains information about the propagation times to the antenna. The grey insets show the Rx mode (5a.1) and terminated mode (5a.2) of the SP3T, respectively. Exemplary, numbers (5b) and (5c) mark the switches of two additional antennas and (6b) and (6c) mark the ports of these antennas, respectively. For the second coupling to be measured reliably, it must be ensured that the signal amplitudes are large enough. For this, the isolation of the switch and the reflection parameters of the antenna, i.e., S11, are considered (Fig. 3.11). In the relevant frequency range from 440 MHz to 1050 MHz (-3 dB bandwidth of the Ricker wavelet with center frequency f_c = 750 MHz), the isolation is between -45 dB and -55 dB in Tx mode and between -40 dB and -50 dB in Rx mode (Fig. 3.11 left axis). The antenna exhibits reflections of about -5 dB in this frequency range (Fig. 3.11 right axis). Consequently, the expected signal attenuation for the second coupling is about -45 dB to -60 dB. A total of three amplifiers are used in the signal chain, which together allow a gain of about 65 dB, wherein one of the amplifiers in the Rx circuit is a pro-

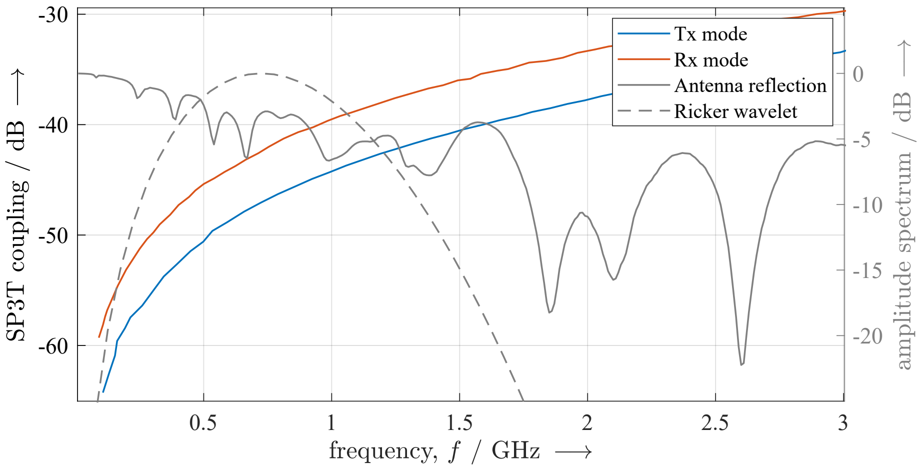

Figure 3.11: Isolation of SP3T switch, scattering parameter of antenna and frequency spectrum of Ricker wavelet.

grammable gain amplifier (PGA). Considering the dynamic range of the ADC, it can be guaranteed that the second crosstalk becomes measurable even when considering further losses within the Tx and Rx circuits (≈ -11 dB). Note that the amplifier circuits have been designed to amplify the 'normal' GPR signal that is transmitted through the soil and are not specifically chosen for the calibration approach presented here. The reflection from the antenna feed point is superimposed by further reflections from components on the antenna PCB such as cable connectors and baluns. These overlaps prevent the determination of the arrival time of the needed antenna feed point reflection. To determine the arrival time of the antenna feed point anyway, an alternative approach is presented. With (1.1) and (3.45), two approaches exist to determine time-zero, where (1.1) can only be used for a known medium between antennas. To determine the correct arrival time of the feed point reflection, a characteristic point within the second coupling is chosen, e.g., local minima/maxima or zero-crossings, and a timing offset t_{offset} to the arrival time is determined so that (3.45) yields the same time-zero as (1.1):

$$t_{\text{offset}} = -t_{0\,\text{ref}} + \frac{t_{\text{a}\,1.1\,2.1} - t_{\text{a}\,2.1\,1.1}}{2} + t_{\text{min}\,1.1} + t_{\text{min}\,2.1}\,, \tag{3.48}$$

where $t_{0\,\text{ref}}$ is the known time-zero from the calibration performed with a known medium between antennas, the fraction is the time offset of the reciprocal measurements and $t_{\text{min}\,1.1}$ and $t_{\text{min}\,2.1}$ are the known minima times within the second coupling. It is important that t_{offset} is constant and identical for all antenna combinations to be used universally. In general, the experimental determination of such a temporal offset is common practice and is used, e.g., by Yelf et al. (2004) [63] to determine the arrival time of signals in pavement measurements. In chapter 5 this offset is experimentally determined for different antenna channels via an evaluation board. Even though t_{offset} should ideally be identical for all antenna combinations, there are certain differences between the exact values for t_{offset} per antenna combination. Therefore, in addition to t_{offset}, first

$$\bar{t}_{\mathrm{offset}} = \frac{1}{n}\sum_{i=1}^{n} t_{\mathrm{offset}\,i}\,, \tag{3.49}$$

is defined where $t_{\mathrm{offset}\,i}$ is the calculated offset for one WARR measurement consisting of n individual measurements and for a fixed antenna combination. Thus, an average $\bar{t}_{\mathrm{offset}}$ can be calculated for each antenna combination. In the next step, the $\bar{t}_{\mathrm{offset}}$ are additionally averaged over all measured antenna combinations to obtain a general timing offset:

$$\hat{t}_{\mathrm{offset}} = \frac{1}{m}\sum_{j=1}^{m} \bar{t}_{\mathrm{offset}\,j}\,, \tag{3.50}$$

where m is the number of measured channel combinations and $\bar{t}_{\mathrm{offset}\,j}$ is the average offset for a specific antenna combination. Only if $\hat{t}_{\mathrm{offset}}$ does not have a large standard deviation, i.e. is smaller than 25 ps, the timing offset can be used reasonably for all antenna combinations.

3.5 Reciprocity analysis with synthetic soil model

In the previous section an approach is presented how to calibrate the tile ground penetrating rader (GPR) system. An essential requirement for this approach is the reciprocity of the electromagnetic waves in the ground between two antennas. For linear, passive and time-invariant systems, such as the ground, the reciprocity is always given (section 2.1.2). Nevertheless, recently the suspicion arose that reciprocity might be disturbed in the presence of dipping angles and waveguides within the ground [94]. Therefore, this section discusses a synthetic soil model that will be used to investigate reciprocity for specific soil structures. The synthetic soil model is implemented using the modeling tool gprMax. The soil is constructed as shown in Fig. 3.12 and replicates a borehole measurement. The boreholes are spaced 12 meters apart and have a depth of 15 meters, whereas in the figure the depth is shown from 7 meters to 15 meters. The soil has a constant permittivity of $\varepsilon_{\mathrm{r}} = 12$. A waveguide with a dipping angle and a permittivity of $\varepsilon_r = 26$ runs across the ground. This waveguide could lead to local anisotropies and thus non-reciprocal signal behavior. Since gprMax uses the finite differences time domain (FDTD) method as the solver for Maxwell's equations, the reflection behavior of electromagnetic waves at interfaces is implicitly implemented. Consequently, the simulation approach is suitable to investigate whether waveguides with dipping angles

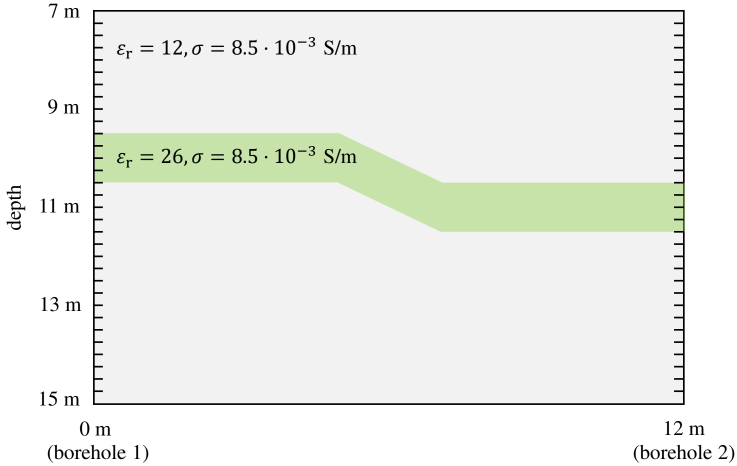

Figure 3.12: Synthetic soil model

disturb reciprocity. For the experiment, a transmitting antenna is first positioned in the left borehole at a depth of 7 m. The receiving antenna is placed in the right borehole and is moved successively from 7 m to 15 m depth in 0.25 m steps. The experiment is then rerun with the transmit antenna placed in the right borehole and the receive antennas are in the left borehole. Transmit and receive antennas are simulated as a Hertzian dipole. The transmit signal is a Gaussian wavelet with a center frequency of 100 MHz. The ground model is divided into 2.5 cm x 2.5 cm areas. This simulation setup is based on Klotzsche et al. (2014) [94], where the reciprocity of the signals is not directly apparent. First, the signals when transmitted from either Tx at 10 m depth in the left borehole to Rx at 12 m depth in the right borehole, or vice versa, are compared. The signals are identical within machine accuracy. Consequently, the signals are reciprocal (Fig. 3.13a). In the next step, the energy of the signals is calculated for all simulated receiver positions for either Tx at 10 m depth in the left borehole or at 12 m depth in the right borehole (Fig. 3.13b). The respective energy of a received signal $y(t)$ is calculated as $E = \langle y(t), y(t) \rangle$, where $\langle ., . \rangle$ is the inner product. The energies differ for different receiver positions and depending on whether the transmitter is located in the left or right borehole. Only for the two marked points the energies match exactly. These points represent the energies of the signals from Fig. 3.13a. This concise synthetic analysis shows that even special ground structures like waveguides with dipping angles do not disturb the reciprocity of the electromagnetic waves. When comparing energies for different positions of transmitting and receiving antennas, misinterpretation of reciprocity can occur if the definition of reciprocity is not clear. In this work, reciprocity describes that swapping transmitting and receiving antennas while maintaining the transmitted signal results in identical signals and identical signal propagation times between the antennas.

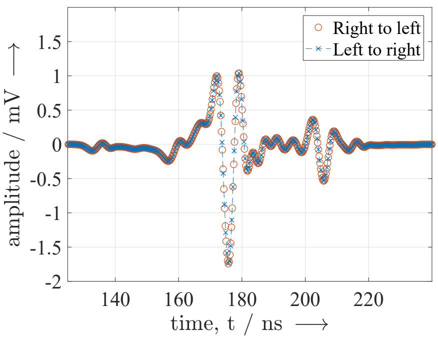

(a)

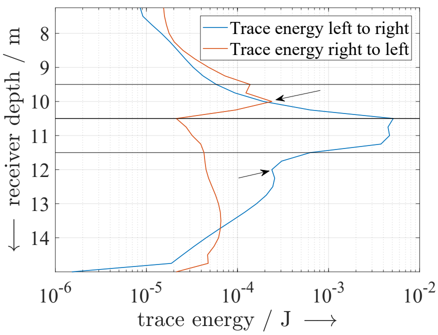

(b)

Figure 3.13: (a) Reciprocal borehole signals (b) Signal energies for multi-offset borehole signals.

This is the fundamental requirement for the presented calibration method.

3.6 Picking of arrival times

The previous considerations for an in situ calibration are based on the approach of conducting reciprocal measurements. However, besides a suitable calibration method, a robust method for picking the arrival times from the measurement signals is important. This is especially crucial for high-bandwidth signals such as the Ricker wavelet, as different frequency components can experience different phase delays. This is briefly discussed in section 5.1. Therefore, four possible methods are presented to determine the signal arrival times. Note that these four methods are by no means a complete list of possible methods. In this thesis, however, the focus is confined to the four methods presented.

Threshold

The first method used to determine arrival times for varying antenna distances is a simple threshold approach. As soon as the signal amplitude rises above a specified threshold value, the arrival time is picked. The threshold is set to $\mu + 6\nu$, where μ is the mean value and ν is the standard deviation of the noise level. The factor 6 is chosen empirically to guarantee that only the main signal exceeds the threshold. A threshold-based picking is used, e.g., by Dafflon et al. (2011) [95].

First peak

The first peak approach uses the first detected signal maximum (or minimum) and a specified offset between the first peak and the arrival time. This approach is used as the first peak has a better signal-to-noise ratio (SNR) than the value determined via the threshold method. The offset between first peak and arrival time is selected manually and requires the operator's experience [96].

Cross correlation

This approach takes advantage of the fact that the medium between the antennas can be described as an LTI system. Consequently, the received signal shape does not change even if the antenna distance changes. Thus, the time shift t_{shift} between a reference signal and newly measured signals can be calculated via the cross correlation. In this work, the measured signal in air with the largest antenna distance is used as the reference signal for each respective measurement series. Then

$$R(t_{\mathrm{shift}}) = \sum_{t=-\infty}^{\infty} x(t) \cdot y_d(t + t_{\mathrm{shift}}) \tag{3.51}$$

is used to maximize R for a given time shift t_{shift}, where x is the reference signal and y_d is the measured signal for a specific antenna distance d. The arrival time of each individual signal is determined by picking the arrival time of the reference signal, e.g., with the threshold or first peak approach and subtracting the corresponding t_{shift} from the reference arrival time. A similar approach was found to be very effective for picking arrival times of crosshole data [97].

Symmetry point

In contrast to the previous methods, where the measured data is evaluated directly, this method evaluates the estimated impulse response. For an LTI system with impulse response $h(t)$, the measured signal can be described by $y(t) = s(t) * h(t)$ with $s(t)$ as the transmit pulse, i.e., Ricker wavelet $\psi(t)$ with known f_{c} in this work. If $s(t)$ is initially unknown, it needs to be approximated. Note that $h(t)$ shall comprise the filter characteristics of the entire transmission chain consisting of Tx and Rx antennas as well as any filters in the Tx or Rx signal processing channel, respectively. Varying the distance d between Tx and Rx antennas causes only a time shift of $h(t)$ and, hence, of the received signal

$$h_d(t) = h(t - d/c)\,, \tag{3.52}$$

where c is again the speed of light in free space and $h_d(t)$ is the time shifted impulse response. In GPR setups, $h(t)$ is a band-pass, i.e., there is no transmission towards very low and very high frequencies. Further, transmit amplifier, antennas and receiver are typically designed to have linear phase, meaning that $h(t)$ is a linear phase filter within the pass band with very good approximation. Such a filter is either an even or odd function, i.e., $h(-t) = h(t)$ or $h(-t) = -h(t)$ [98]. This symmetry can be used to identify the time shift d/c. Determining $h_d(t)$ involves reverting (2.32), which means that $y(t)$ has to be deconvolved with respect to $s(t)$. According to (2.40) it follows that

$$y_d(t) = s(t) * h_d(t) \,\Delta\, Y_d(f) = S(f) \cdot H_d(f)\,. \tag{3.53}$$

For $S(f) \neq 0$, (3.53) can be divided by $S(f)$ to obtain an estimate of the channel transfer function

$$\hat{H}_d(f) = Y_d(f)/S(f)\,. \tag{3.54}$$

However, in practice this direct deconvolution suffers from noise amplification, where the amplitude of $S(f)$ becomes small. Better results are achieved by a Wiener deconvolution

$$\hat{H}_d(f) = Y_d(f)\frac{S(f)}{|S(f)|^2 + K}\,, \tag{3.55}$$

where K is used as an optimization parameter that is chosen such that $\hat{h}_d(t) \,\Delta\, \hat{H}_d(f)$ becomes a good linear phase approximation of $h_d(t)$ (here $K = 2$). After inverse Fourier transformation an estimate for $h_d(t)$ with $\hat{h}_d(t) = \hat{h}(t - d/c)$ at $t = d/c$ is obtained. The symmetry point of $\hat{h}_d(t)$ indicates the time shift caused by the transmission chain. Here, $\hat{h}_d(t)$ is an odd function (Fig. 3.14), where the symmetry point can easily be identified by determining the zero crossing between the two largest signal peaks.

For all four presented approaches, a higher temporal signal resolution increases the accuracy. Therefore, to prevent the usage of higher sampling rates, a spectral interpolation is applied to the signals before time picking according to (2.47). Furthermore, all methods except the threshold approach require an additional hand picked reference point for the arrival time to define a constant offset between, e.g., the first peak or symmetry point and the hand picked time. A direct comparison of the methods is given in Tab. 3.1.

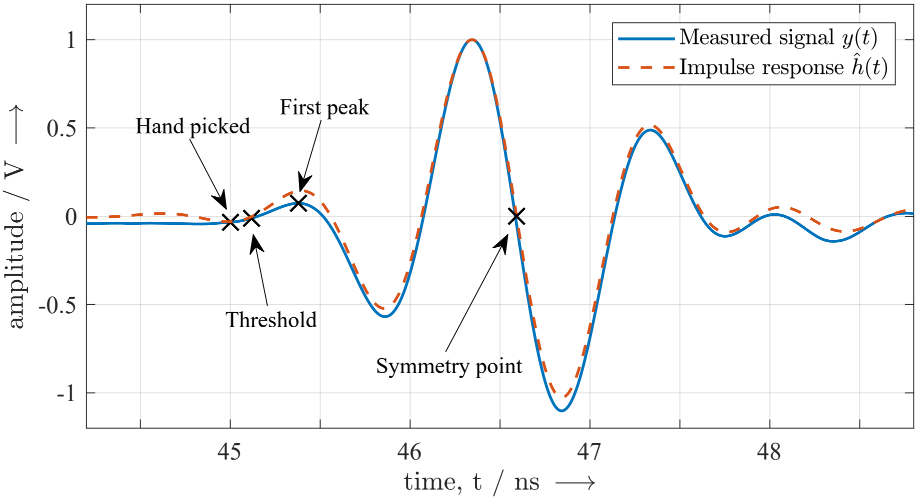

Figure 3.14: Characteristic points within signal

Table 3.1: Comparison of methods for picking arrival times.

Method	Advantages	Disadvantages
Threshold	• Usable without specified offset	• Threshold value must be specified • Lowest SNR among methods
First peak	• Higher SNR als threshold method • Easily detectable	• Constant offset required • Based on only one single point
Cross correlation	• High SNR, as the entire signal can be used	• Higher computational cost than threshold and first peak • Constant offset required
Symmetry point	• Very high accuracy for linear transfer functions • Relatively easy to detect	• Transmit pulse needs to be known precisely • Linear phase response required • Constant offset required

Chapter 4

Simplified GPR system analysis

In this chapter, the results of the analyses with the simplified system design are presented. A detailed presentation of the simplified system design has been given in sections 3.2.2 and 3.3. Two approaches can be used for the calibration of the system: (i) the pairwise calibration (section 3.3.2) and (ii) the mesh calibration (section 3.3.3). The experimental implementation of these two approaches is explained in section 4.1. The results section is divided into four parts: (i) analysis of mesh calibration for different configurations via numerical modeling, (ii) results of pairwise calibration for determining trigger offsets and instrumental delays, (iii) analysis of a coupling signal between neighboring antennas, and finally (iv) analysis of the ground influence on coupling signals as these can be used to verify requirements for the mesh calibration.

4.1 Experimental setup

4.1.1 Simulations

A simulation is utilized to analyse the feasibility and in particular the accuracy of the mesh calibration. Equations (3.16), (3.21), (3.27) and (3.28) are used as the mathematical model within the simulation to verify the correction approach. For the simulation, the matrix $\boldsymbol{B}$ in (3.16) is defined such that all possible $3000 \cdot 2999$ trigger offsets are calculated. Finally, the results are assessed by calculating the normalized root mean square ($nRMS$) of the calculated erroneous trigger offsets $\tilde{\boldsymbol{t}}_{\text{searched}}$ between any two base boards (BABs) i and j by utilizing the true trigger offsets $\boldsymbol{t}_{\text{searched}}$ as

$$nRMS_{i\,j} = \frac{1}{\eta}\sqrt{\frac{\sum(\boldsymbol{t}_{\text{searched}} - \tilde{\boldsymbol{t}}_{\text{searched}})^2}{N}}\,, \tag{4.1}$$

where η is the predefined standard deviation of random errors ξ_{Tx} and ξ_{Rx} and N is the number of simulations conducted with the same value for η. This allows to investigate how the single standard deviation η transfers to the searched trigger offsets. In this

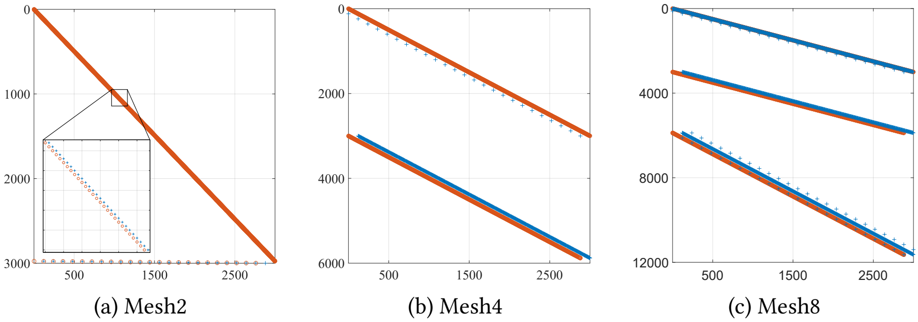

Figure 4.1: Sparse matrices according to (a) Mesh2, (b) Mesh4, and (c) Mesh8.

work, $N = 10000$ is used. In addition to the $nRMS$, the mean $nRMS$ for a fix BAB i is calculated as

$$\overline{nRMS}_i = \frac{1}{3000} \sum_{j=1}^{3000} nRMS_{i\,j}$$

to further evaluate the error propagation. Mesh2, Mesh4 and Mesh8 are used as example meshes. For each mesh, the QR decomposition is performed once, since only t_{obs} changes when solving the linear equation system according to (3.21). A visualization of the sparse matrices $\boldsymbol{A}$ of Mesh2, Mesh4 and Mesh8 is given in Fig. 4.1.

4.1.2 Measurements

The measurements presented in this chapter should be understood as preliminary tests within the design phase of the monitoring system. Therefore, to conduct reciprocal measurements, a Keysight arbitrary waveform generator (AWG) M8190A is used. The generator transmits two signals, one measurement signal, i.e., a Ricker wavelet with an amplitude of 1 V, a center frequency of $f_c = 750$ MHz and maximum frequency components below 2 GHz and a trigger signal to trigger the Rx part, here a Keysight DSAX91304A Infiniium high-performance oscilloscope. The oscilloscope samples with 4 GSa/s (gigasamples per second) to fulfill the Nyquist criterion with regard to the used Ricker wavelet and averages the signals by a factor of 64. Also, the signals are interpolated via zero-padding (2.47) to get higher timing resolutions when picking arrival times or determining time lags between signals. The generator is connected to the Tx part, for this test a simple interconnection without an active functionality, via an SMA cable with a length of 0.91 m (cable 1) and a trigger time of t_1. Secondly, another SMA cable with a length of 1.83 cm (cable 2) and a trigger time t_2 is used to connect the trigger output

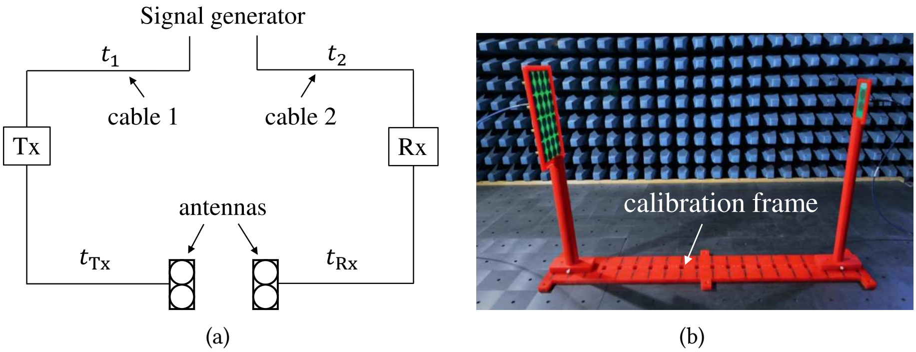

Figure 4.2: (a) Schematic measurement setup and (b) part of measurement setup in anechoic chamber.

of the generator to the oscilloscope (Fig. 4.2a). According to (3.10), the trigger offset $t_{i\,j}$ can be measured by performing reciprocal measurements. For this setup, the two SMA cables are interchanged and, thereby, model a reciprocal measurement. Additionally, a time-domain reflectometry (TDR) measurement utilizing the vector network analyzer (VNA) Keysight E5071C with the used cables is performed to implement a reference. The instrumental delays t_{Tx} and t_{Rx} are measured by performing wide angle reflection and refraction (WARR) measurements using a calibration frame (Fig. 4.2b) and (3.8). A complete WARR measurement takes about 30 minutes to collect data. For each measurement at a specific distance between the antennas, the cables 1 and 2 are interchanged to simulate reciprocal measurements. Both the antenna array and the single circular bowtie antenna are located freely in air and are mounted at a height of about 0.55 m above the ground. The antennas are then moved apart in 0.05 m steps. Despite this almost ideal measurement setup for performing reciprocal measurements, minor uncertainties in the positioning of the antennas will lead to inaccuracies in the determination of time-zero and the instrumental delays $t_{\mathrm{Tx\,Rx}}$. The positioning accuracy is estimated to be within one millimeter which corresponds to 3 ps time accuracy.

As stated in section 3.6, the accurate picking of arrival times is essential. Therefore, the results of the linear regression for each of the four described arrival time picking methods are compared in terms of their R^2 and the standard deviation of the residuals between measured and modeled arrival times at varying antenna distances, termed $\hat{s}$. Finally, the determined trigger offset $t_{1\,2}$ and instrumental delay $t_{\mathrm{Tx\,Rx}}$ are combined as in (3.1) and compared to two time-zero values determined by classical correction measurements without interchanging cables. Next, to measure the influence of the lysimeter filling on t_{p} between adjacent antennas (horizontal, vertical, diagonal) as required for the detection of systematic errors as in (3.8), a test setup as depicted in Fig. 4.3 is used.

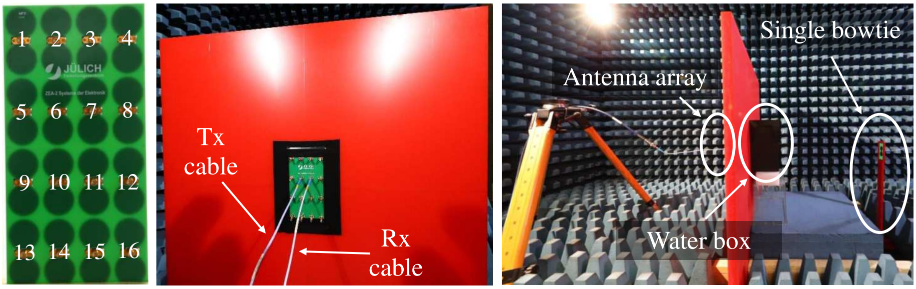

(a) (b) (c)

Figure 4.3: (a) 4x4 antenna array (b) Array taped to PVC plate (c) Side view of the test setup.

To have a realistic estimation of coupling signals, an antenna array as planned for the GPR system is used (Fig. 4.3a). This array consists of 16 circular bowtie antennas. To refer more easily to specific antennas, a number is assigned to each antenna. The size of a single bowtie antenna of 3 cm × 6 cm is derived from the required spatial resolution of the soil analysis [99]. The antenna array is taped to the polyvinyl chloride (PVC) plate of dimensions 1 m × 1 m × 0.03 m which represents the lysimeter wall (Fig. 4.3b). Two antennas are connected to the AWG and oscilloscope, respectively. An additional box made of PVC can be filled with water and placed behind the PVC plate to simulate changing material properties inside the lysimeter and, thereby, test the influence of the lysimeter filling onto coupling signals (Fig. 4.3c). A further circular bowtie antenna can be used to conduct WARR measurements in air by connecting the Rx cable to the single bowtie antenna. The experimental setup represents a reduced setup, but it contains all relevant elements of the later system, i.e., antenna size, antenna spacing and thickness of PVC wall, and thus allows a realistic estimation for the true system behaviour.

4.2 Results

4.2.1 Simulation of mesh calibration

The standard deviation of the mesh calibration is complex to analyze analytically due to dependencies between variables and is, therefore, analyzed in this section using a simulation following the considerations of section 3.3.3. Fig. 4.4 shows the *nRMS* values according to (4.1) for Mesh2, Mesh4, and Mesh8 in the range of BABs 1200 to 1560. The corresponding BABs 1200 to 1560 are placed in the middle of the lysimeter or mesh, respectively. In all three cases, the number of simulation runs is N=10000. Note that

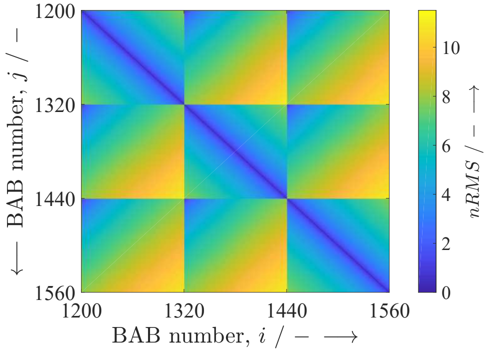

(a) Mesh2

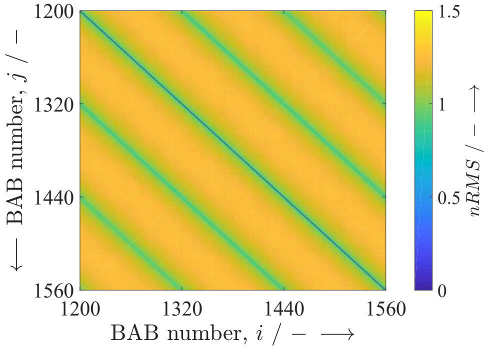

(b) Mesh4

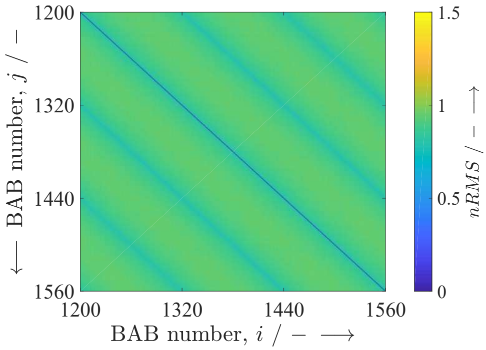

(c) Mesh8

Figure 4.4: Normalized root mean square error for (a) Mesh2, (b) Mesh4 and (c) Mesh8.

different scalings on the colorbars are used. Fig. 4.4a exhibits a clear pattern that separates the *nRMS* values into 120×120 areas. Each area represents one ring around the lysimeter. Remember that 120 BABs are placed around the lysimeter in one ring. The last BAB per ring performs a reciprocal measurement only with the left neighbor in the same ring (Fig. 3.6a). It thereby follows that to calculate the trigger offsets between the first and last BAB per ring, 119 intermediate measurements are required compared to, e.g., Mesh4 and Mesh8, where one additional measurement is performed between the first and last BAB per ring. This pattern becomes visible in Fig. 4.4a, where the *nRMS* increases with the distance between the first and last BAB per ring. Here, the term distance refers to the number of reciprocal measurements required to connect any two BABs. After each 120 steps, the *nRMS* value again decreases due to a direct vertical measurement between the two first BABs of neighboring rings. The diagonal is zero by definition ($t_{i\,i} = 0$). Furthermore, the *nRMS* values are symmetric around the diagonal, because $t_{i\,j} = -t_{j\,i}$ by definition. The overall mean *nRMS* value for Mesh2 yields 7.70. For Mesh4 and Mesh8, the observed pattern for the *nRMS* of Mesh2 does not occur due to further measurements between additional neighboring BABs (Fig. 4.4b and 4.4c). The largest distance for two BABs in one ring now exists between BABs on opposite sides of the lysimeter. The characteristic feature in Fig. 4.4b and 4.4c is that in addition to the main diagonal, further diagonal lines are visible. These lines result from further direct vertical measurements, e.g., between BABs 2 and 122 or BABs 3 and 123. Thereby, the error between the corresponding trigger offsets is reduced. The diagonal lines repeat every 120 BABs because, again, this is the number of BABs per ring. For Mesh4, the mean *nRMS* equals 1.22, indicating that the larger system of linear equations reduces the error by a factor of about 6 compared to Mesh2. This reduction is not directly evident from the observation of the covariances in Fig. 3.7 which emphasises the necessity of the simulation. For Mesh8, the mean *nRMS* is 0.93. This result shows that the standard deviation of the trigger offsets for any BABs can be lower than the initial standard deviation for a direct reciprocal measurement between two BABs. In general, the patterns of *nRMS* correspond as expected to the structures of the covariance matrices presented in section 3.3.3. To further evaluate the results, the mean nRMS $\overline{nRMS}$ is calculated and shown in Fig. 4.5. For Mesh2, a sawtooth like pattern is observable (Fig. 4.5). This results from the arrangement of reciprocal measurements between neighboring BABs, because the first BAB per ring has a smaller distance to BABs in other rings compared to the last BAB per ring, as discussed before for Fig. 4.4. For Mesh4 and Mesh8, the sawtooth pattern is removed due to additional reciprocal measurements between neighboring BABs. The $\overline{nRMS_i}$ values show that BABs in the upper and lower rings exhibit larger mean *nRMS* values. This is because BABs in the top and bottom ring perform less reciprocal measurements, i.e., three or five instead of four or eight, respectively, and thereby have an influence on the following rings. Therefore, the most significant jump for the $\overline{nRMS}$ values appears after BAB index 120 and before BAB index 2880 for Mesh4 and Mesh8, respectively. This should be considered within the full-waveform inversion (FWI), because these BABs tend to have less accurate time-zero values when using the mesh

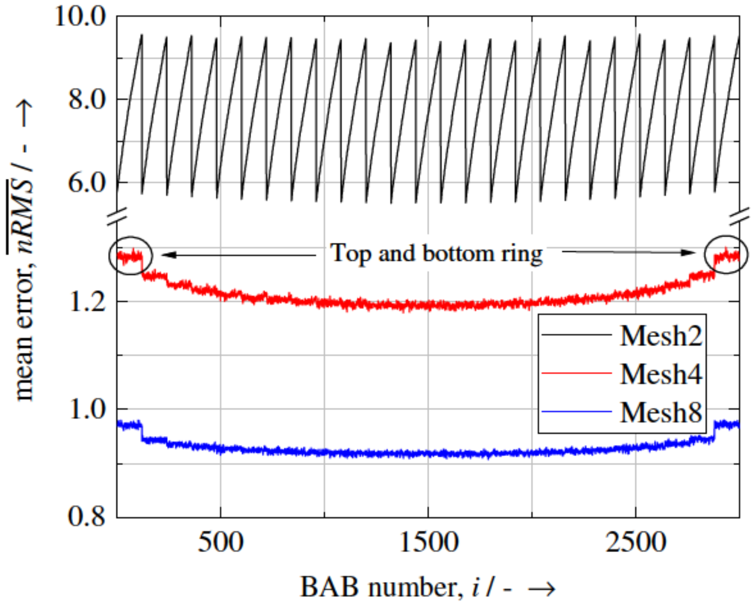

Figure 4.5: Mean $nRMS$ value $\overline{nRMS_i}$ for every column i for Mesh2, Mesh4, and Mesh8, respectively.

calibration. Note that if reciprocal measurements between BABs from the top and bottom ring were conducted, the $\overline{nRMS}$ values would not show this stepwise pattern. In principle, the construction of the system of linear equations as in (3.14) is not limited to measurements between neighboring antennas as long as reciprocity is guaranteed. As a consequence, one can use the signals through the soil together with (3.10) to solve the system of linear equations by utilizing an even larger matrix $\boldsymbol{A}$ compared to that of Mesh8. Nevertheless, the results of Mesh8 are already satisfactory and show that the standard deviation increases with less than $\sqrt{k} \cdot \eta$ for an increasing number k of intermediate BABs between any two BABs as it is the case for Mesh2. The usage of a larger linear equation system, therefore, offers significant advantages in terms of error propagation. This result states that random error variances in the low picosecond area are negligible for the calibration approach. Note that using all eight neighboring BABs of a Tx BAB as additional Rx does not increase the tomographic measurement time significantly, because the calibration measurements can be included in the actual tomographic measurement, so almost real in situ.

4.2.2 Trigger offsets and instrumental delays

After demonstrating the effectiveness of the mesh calibration via simulations in the previous section, this section presents the first measurement results for determining the trigger offsets and instrumental delays. First, the trigger offsets, or in this case the difference between trigger times t_1 and t_2 (Fig. 4.2) are determined by performing reciprocal measurements. Two measurements are performed with interchanging the cables 1 and 2 between the measurements and using (3.10) to calculate $t_{1\,2}$ via the cross correlation of the two signals. This procedure is repeated ten times, yielding a mean trigger offset of 3.928 ns and a standard deviation of 0.001 ns (Tab. 4.1). Two references are given by (i) the datasheet of the used cables and by (ii) performing TDR measurements with the two cables. The TDR measurements are repeated multiple times without any noticeable variation in the results, i.e., less than 0.1 ps, indicating a high significance. In the data sheet no information is given regarding uncertainties. Concluding, the reciprocal measurements yield a 9 ps difference for the trigger offset compared to the TDR measurements and a 4 ps difference to the datasheet. Here, it is not judged which approach is the most accurate, but it is concluded that the differences between the datasheet, TDR and reciprocal measurements are within an acceptable range for the calibration of the monitoring system. Therefore, trigger offsets are determined sufficiently accurate by performing reciprocal measurements.

Next, the four methods for determining arrival times and instrumental delays are compared. Fig. 4.6 shows normalised received signals for antenna distances of 15 cm, 45 cm and 85 cm, which are used together with measurements at additional antenna distances for the extrapolation. The results of the four methods are summarized in Tab. 4.2. All four approaches have an R^2 value of almost 0.99 and above, which illustrates the linear relationship between the arrival times for varying antenna distances. However, the values determined based on the threshold approach show the largest uncertainties regarding $\hat{s}$, as the signal amplitudes change over the distance and thus the arrival time within a signal is selected progressively later for the same threshold value (Fig. 4.6). Normalizing the signals is therefore advised. The accuracy is increased by using the first peak as

Table 4.1: Trigger offset of the used cables, determined via the datasheet, TDR and reciprocal measurements.

Datasheet / ns	TDR / ns	Reciprocal / ns
3.932	3.919 ± 0.000	3.928 ± 0.001

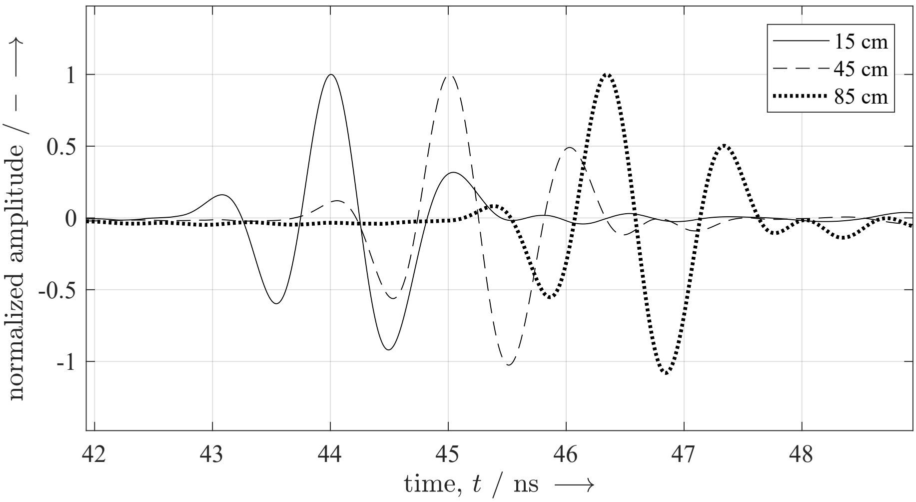

Figure 4.6: Normalized signals for varying antenna distances.

Table 4.2: Comparison of four methods for arrival time picking.

	$t_{\mathrm{Tx\,Rx}} \pm \hat{s}$ / ns	R^2 / -
Threshold	38.278 ± 0.101	0.9876
First peak	38.259 ± 0.012	0.9998
Cross corr.	38.259 ± 0.005	1.000
Symmetry point	38.236 ± 0.002	1.000

the reference point within the signals. The results obtained by the cross correlation and symmetry point approach each show a further improvement in accuracy. Additionally, to analyze the results, the residuals from the respective mean $t_{\mathrm{Tx\,Rx}}$ for the first peak, cross correlation and symmetry point approach are depicted in Fig. 4.7. Both the first peak and cross correlation approach exhibit a trend in the residuals, indicating systematic errors which are caused by antenna near field effects. The cross correlation shows a weaker trend due to an averaging effect as more data points are used for the calculation compared to the first peak method. However, the symmetry point approach shows the weakest trend for the residuals. Therefore, the symmetry point used in this approach is a good choice for a reference within the signals as this point is least influenced by near field effects. This facilitates reference measurements to determine t_0 or $t_{\mathrm{Tx\,Rx}}$. In fact, near field effects change the symmetrical impulse response to a non-symmetrical impulse response, violating the linear phase assumption of the system. Still, the symmetry point is least affected by this and is, therefore, the recommended reference point within the signals when accuracy needs to be exceptional. A similar residual behavior is observed for two additional WARR measurements. Finally, the absolute values for $t_{\mathrm{Tx\,Rx}}$ differ by up to 40 ps, causing uncertainty for $t_{\mathrm{Tx\,Rx}}$. This is because the constant offset between first peak and symmetry point is applied to all measurements, although the pulse shape alters for varying antenna distances.

According to (3.1), combining the determined trigger offset and instrumental delays yields the required t_0. Two additional WARR measurements are conducted to give a ref-

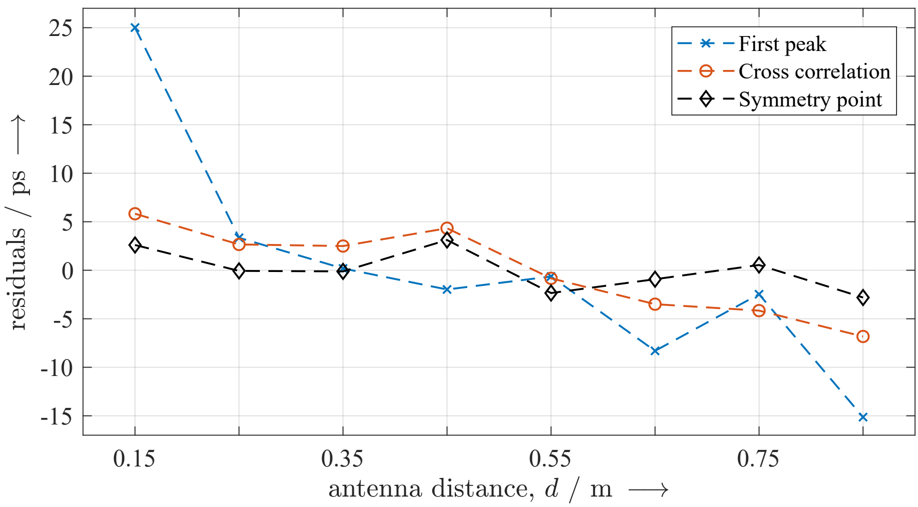

Figure 4.7: Residuals to average time-zero for different picking methods

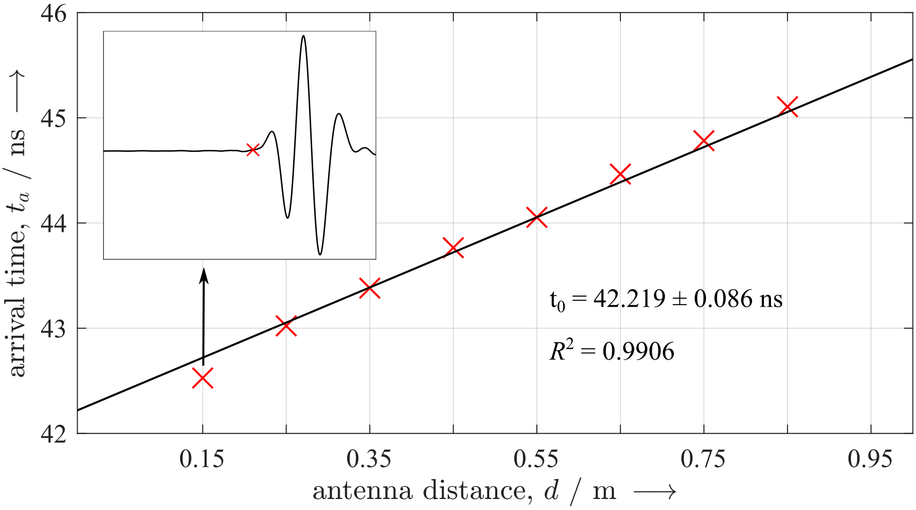

Figure 4.8: WARR measurement arrival times for varying antenna distances.

Table 4.3: Comparison of time-zero determined by classical time-zero measurements and time-zero determined by the sum of timing offset and instrumental delay.

	$t_{1\,2} + t_{\mathrm{Tx\,Rx}}$ / ns	$t_{0\,\mathrm{ref}\,1}$ / ns	$t_{0\,\mathrm{ref}\,2}$ / ns
Threshold	42.206 ± 0.101	42.219 ± 0.086	42.223 ± 0.116
First peak	42.187 ± 0.012	42.182 ± 0.011	42.184 ± 0.008
Cross correlation	42.187 ± 0.005	42.178 ± 0.003	42.187 ± 0.005
Symmetry point	42.164 ± 0.002	42.167 ± 0.002	42.164 ± 0.005

erence for t_0, termed $t_{0\,\mathrm{ref}\,1}$ and $t_{0\,\mathrm{ref}\,2}$, but this time without interchanging the cables. The amount of additional WARR measurements is limited to two as a compromise between measurement effort and information yield. The results of the classical time-zero measurements are summarized and compared to $t_0 = t_{1\,2} + t_{\mathrm{Tx\,Rx}}$ in Tab. 4.3. As an example, all arrival times including the resulting time-zero of the WARR measurement for threshold picking are shown in Fig. 4.8. The results show that decomposing the measurement of t_0 into trigger offset and instrumental delay determination is feasible. This applies to all four methods for picking arrival times as the absolute values for time-zero vary by not more than 17 ps per ring. Still, the symmetry point approach proves to be the most accurate method in terms of relative accuracies. In the following, the first peak will be the picking method of choice at it is easily applicable with sufficient accuracy. If there is insufficient accuracy in individual measurements, either the cross correlation or the symmetry point can be used. Further, the results show that absolute time-zero varies by almost up to 60 ps depending on the method used to determine arrival times. Even when excluding the threshold approach, absolute time-zeros still show a difference of more than 20 ps between cross correlation and symmetry point for the second reference WARR measurement. This can become an error source for the FWI [6]. Therefore, it is suggested to define the offset between, e.g., the symmetry point of the impulse response and the arrival time as an additional parameter within the inversion instead of solely defining this constant offset manually. Similar methods are used by, e.g., Dafflon et al. (2011) [95] and Irving et al. (2007) [97], to correct for static time shifts.

4.2.3 Mutual coupling

In the previous section it is shown that time-zero can be determined from the sum of the trigger offset and the instrumental delay. Assuming that the instrumental delay is identical for all BABs, the trigger offset between any BABs can be determined again via reciprocal measurements, independent of their position relative to each other. If, on the other hand, the instrumental delays are time-variant or unknown, no complete time-zero correction can be performed with the approach presented so far. However, equal propagation times t_p for coupling signals allow to verify and test the assumption that $t_{\mathrm{Tx\,Rx}}$ is equal for all BABs, as described in section 3.3.2. Therefore, different materials are placed behind the PVC and the impact on t_p is analyzed. Fig. 4.9 exemplifies the signal coupling between adjacent antennas, where antenna 6 (Fig. 5.2a) is used as Tx and antennas 7, 10, and 11 are used as Rx to illustrate horizontal, vertical and diagonal coupling signals, respectively. All three coupling directions (horizontal, vertical, diagonal) can in principle be used for the mesh calibration and will be analyzed for their dependency with respect to the lysimeter filling. For each Tx/Rx combination, two measurements are conducted with either air or water behind the PVC (Fig. 4.3c). This experiment is intended to provide a worst case scenario regarding possible permittivity changes of the material behind the PVC ($\varepsilon_\mathrm{air} \approx 1, \varepsilon_\mathrm{water} \approx 80$). The comparison between air and water coupling is evaluated by the time lags between the signals. Fig. 4.10 shows three examples of received signal pairs. The time lags are calculated either via the temporal difference between the first peaks of both signals (Fig. 4.11a, marked by black circles in Fig. 4.10) or their cross correlation (Fig. 4.11b). Comparing the associated signals in Fig. 4.10 gives insight into the impact of changing permittivities behind the PVC on the signals. The black circles mark the first local extrema that are used to calculate time lags. Fig. 4.10a shows that when comparing the local minima and maxima of the two signals for Rx7 (horizontal neighbor), the time points of similar peaks arrive later for the air signal, which is unexpected, and tend to shift apart for later time points. For Rx10 (vertical neighbor, Fig. 4.10b), the peaks of the air signal appear earlier than the peaks of the water signal. For Rx11 (diagonal neighbor, Fig. 4.10c), more pronounced time lags are visible before and after the maximum peak. In this case, the air signal arrives after

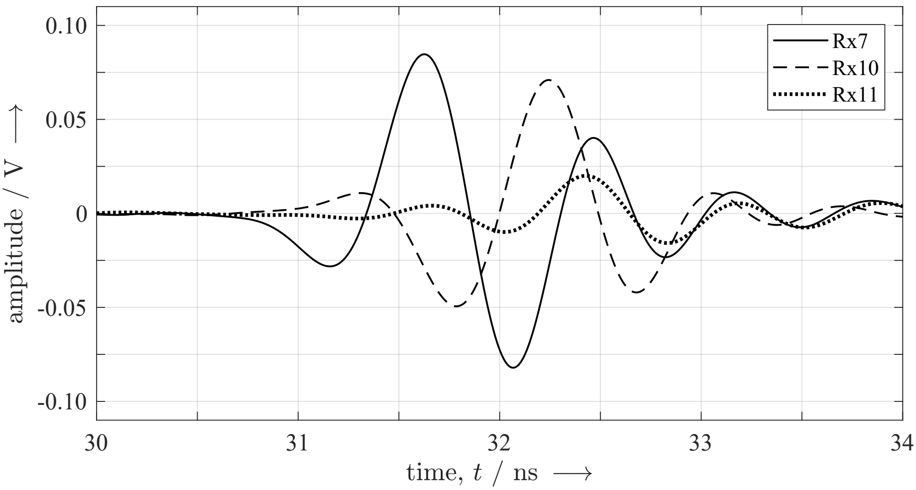

Figure 4.9: Coupling signals for varying Tx/Rx configurations.

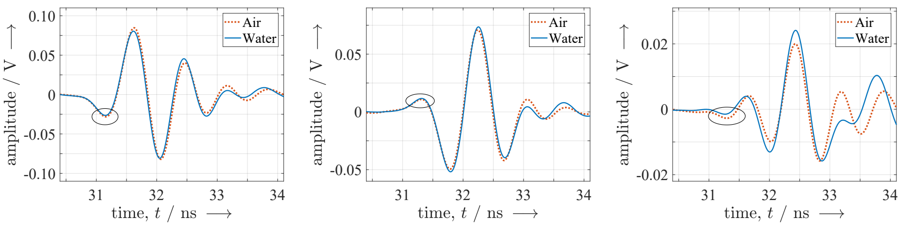

(a) Rx7 (b) Rx10 (c) Rx11

Figure 4.10: Coupling signals when either air or water is behind the PVC for antenna 6 as Tx and (a) 7 as Rx, (b) 10 as Rx, and (c) 11 as Rx.

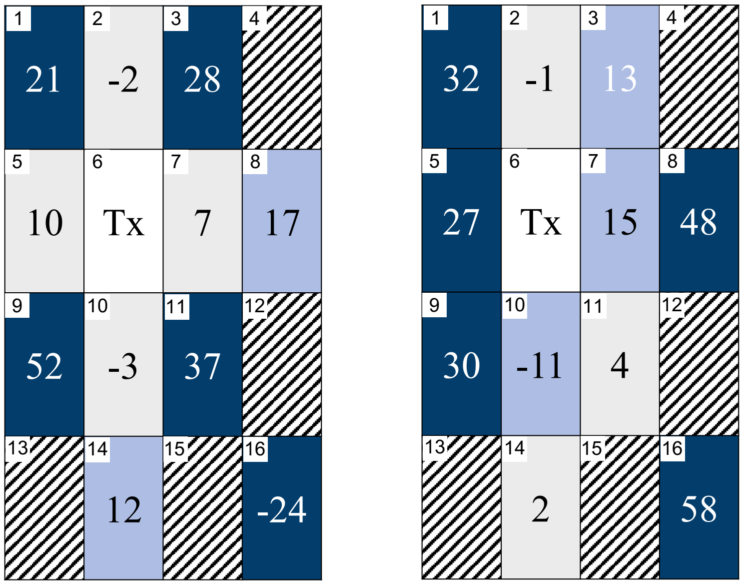

(a) First peak

(b) Cross correlation

Figure 4.11: Time lags in picoseconds between air and water measurements for varying Rx antennas.

the water signal for times earlier than the maximum peak and arrives before the water signal for the following negative peak. As a result of the changed signal shape, the cross correlation, which is used in Fig. 4.11b to calculate the time lags, should be influenced more than the first peaks. Overall, a changing material behind the PVC has an influence on the propagation of coupling signals. However, the influence varies in the course of the signal and is smaller for earlier arrival times for horizontal and vertical signals. To further illustrate this, the differences of first local extrema times and their cross correlation time shift for air and water signals are summarized in picoseconds for different Tx/Rx combinations (Fig. 4.11). No measurements were performed for the dashed rectangles. The small numbers in each box' upper left corners indicate the antenna number. The time lags indicate a smaller material impact for horizontal and vertical measurements. The material impact seems to be systematically and should be further analyzed in future work. The horizontal measurements show a time lag between air and water measurements of up to 10 ps for first peaks and 27 ps for the time lag calculated via the cross correlation. It needs to be tested whether the position of the receivers (Rx5 is located at the edge of the array) has an influence on the signals by, e.g., using a larger antenna array. For vertical measurements, the time lags are already below the determined measurement accuracy of ±4 ps for the first peaks and, therefore, make vertical coupling signals well suited for testing the instrumental delays. This does not apply to the cross correlation, as a value of -11 ps is calculated for Rx10. Diagonal coupling signals should not be used for the analysis as they show the strongest dependency on the lysimeter filling. Especially for the calculations using cross correlation, there is no clear systematic in the time lags. The signals are influenced by the material in the lysimeter, which changes the signal shape and makes the cross correlation less suitable for determining time lags than the first peaks approach.

Comparing air and water signals represents a worst case scenario regarding the material permittivities. For the later soil measurements, ε_r varies in a range between 5 and 40. Therefore, it is reasonable to assume that comparing early signal times and having more realistic material variations behind the PVC reduces the influence of the lysimeter filling onto the coupling signals even more. Then, horizontal coupling signals might be used for testing the instrumental delays in addition to vertical coupling signals. It follows that the assumption that $t_{\mathrm{Tx\,Rx}}$ is equal for all BABs can be tested, as the influence of the lysimeter filling onto coupling signals is negligible.

Fig. 4.12 relates the coupling signals and the corresponding time-zero from a further WARR measurement. It can be seen that for both horizontal and vertical coupling, the onset of the signals occurs before the actual time-zero. This is explained by the fact that the antennas are located in the respective near field and that energy traveling between the tips of the antennas arrives before energy traveling directly between their centers. This is especially true at high Tx-Rx angles [100]. Thus, the time-zero determined in the far field is not valid for the coupling measurements between neighboring antennas. If the time offset of, for example, the minimum of the coupling signal is constant to the far field time-zero, this minimum could be used to determine t_0 between neighboring antennas. Accordingly, similar to (3.5), the determination of any t_0 could be done via coupling signals. At this point, however, the potential implementation via measured signals shall only be illustrated and will not be analyzed further.

4.3 Conclusions

This chapter presents a time-zero calibration strategy for the simplified monitoring system with 3000 BABs that are placed around the lysimeter. Because the system is installed after the filling of the lysimeter, the calibration cannot be performed with known material, e.g., air, between any two antennas. For the simplified monitoring system, the BABs and especially the instrumental delays are assumed to be equal, while the trigger lines to control each BAB can be of different length. Therefore, each possible Tx/Rx combination requires a separate time-zero correction. The approach utilizes the ability of the system to use every antenna as Tx and Rx, and, thereby, allows to conduct reciprocal

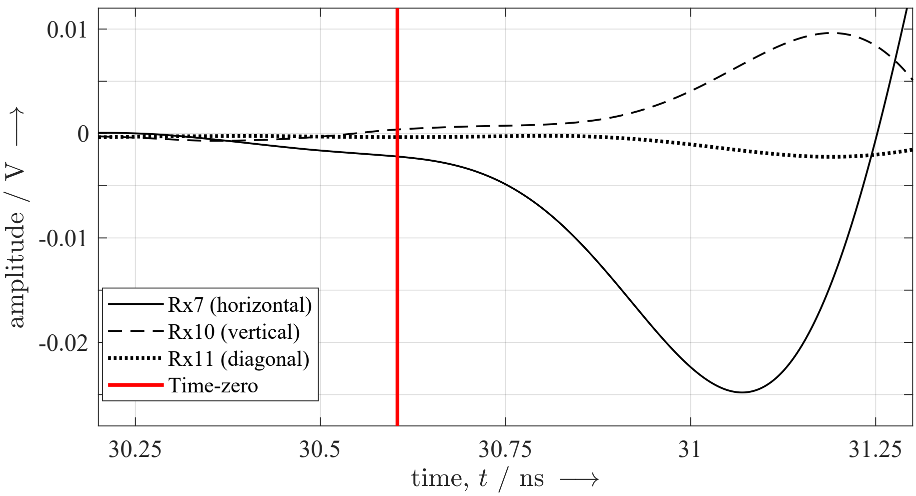

Figure 4.12: Mutual coupling and calculated time-zero.

measurements between any two antennas. This reciprocal measurement arrangement makes it possible to reduce the number of unknowns and enables the measurement of the signal propagation time between two antennas directly and uniquely regardless of the position of the antennas. This procedure is termed as pairwise calibration. Furthermore, reciprocal measurements between BABs can be combined within a superposition to calculate time-zero for any Tx/Rx combination, termed as mesh calibration. Solving a sufficiently large system of linear equations leads to the fact that the standard deviation for time-zero increases significantly slower than with $\sqrt{k}$ for an increasing distance k between two BABs. For jitter values in the low picosecond range, these time inaccuracies can, therefore, be neglected. At this point, however, no statement can be made about how large the jitter can be in the simplified system presented, as the jitter is component-dependent and no information about components was available at this point in the thesis. Also, the mesh calibration can be applied before measuring fast soil processes and, thereby, reduces the measurement time compared to the pairwise calibration. The described methods require equal or known instrumental delays within the BABs. In the following chapter, with the help of specific hardware it will be verified whether and with what reliability this condition is fulfilled. The pros and cons of the pairwise and mesh calibration are summarized in Tab. 4.4.

A prerequisite for both the pairwise and mesh calibration is that reciprocal measurements with unknown medium between antennas can be carried out and thus the trigger offsets can be determined. The results in this chapter demonstrate that conducting reciprocal measurements between BABs that are separated by some unknown medium

Table 4.4: Comparison of pairwise and mesh calibration.

Pairwise calibration	Mesh calibration
+ Single reciprocal measurement can be calibrated	+ Measurements for testing instrumental delays included + Pre-calibration for fast measurements possible
– Longer measurement time for complete tomogram	– Each BAB has to transmit and receive at least once

can be used for the calibration of such a system. The requirement is that instrumental delays are known and a method to determine these delays is presented. Then, varying trigger offsets between any BABs can be measured and used for a time-zero calibration. Additionally, it was shown that the calculation of time-zero via a decomposition into instrumental delays and trigger offset is equivalent to a standard calibration via WARR measurements.

To test the prerequisite that the instrumental delays within the BABs are equal (or known and stable), the influence of the material behind the PVC needs to be negligible for coupling signals. It was found that the influence of the material behind the PVC, or inside the lysimeter, is minimal for horizontal and vertical measurements with less than 10 ps. Therefore, the coupling signals between horizontally and vertically neighboring BABs have the potential to control the assumption that $t_{\mathrm{Tx\,Rx}}$ is equal for all BABs. The diagonal neighbors are significantly influenced by the soil and should not be used for this purpose. This result enables the use of a flexible mesh for the mesh calibration, so whenever a violation of the assumption arises, the corresponding BABs are excluded from the inversion. Further, electromagnetic simulations could be applied to gain a better understanding of the field distribution between neighboring antennas and especially between diagonal neighbors as the influence of the lysimeter filling on the coupling signals is not well understood. The time-zero correction measurement yields an accuracy of 4 ps for the reference measurement. The same accuracy is expected for the trigger lines. The final time-zero error is about $\sqrt{4^2 + 4^2} \approx 6$ ps for the pairwise calibration, which is significantly better than the required 25 ps. Note that this analysis only addresses statistical variations. The magnitude of systematic shifts due to thermal effects and BAB variations in the analog circuits will be investigated in the following chapters. However, the methods and results presented in this chapter provide an important contribution towards an automated in situ time-zero correction of the designed monitoring system. The presented approaches are not limited to the lysimeter application. In principle, the methods can be used by all measurement systems that support reciprocal measurements such that no distinct time-zero measurement setup is needed for calibration. For example, the approach could also be used in multichannel surface measurements, eliminating the need for time-consuming repeated calibration measurements of the system. In addition, the approach enables tomographic measurements via radar signals for any application where manual re-calibration is not feasible.

Chapter 5

Tile GPR system analysis

In this chapter, the calibration approach for the tile ground penetrating radar (GPR) system (section 3.4.2) is verified experimentally. After introducing the adapted measurement setup, various factors influencing the presented calibration method are investigated. The calibration approach for the tile GPR system is an extension of the pairwise calibration. It allows to calibrate any pair of antennas independent of their position without assuming equal instrumental delays.

5.1 Experimental setup

This section describes the measurement setup and data processing for verification, analysis and evaluation of the presented method. As the GPR monitoring system was at an early stage at the time of the analyses of this chapter, the digital-analog converter (DAC) and analog-digital converter (ADC) are replaced by a 2-port measurement using the vector network analyzer (VNA) Keysight E5071C. Using the VNA, the transfer function of any channel can be measured directly. This simplifies the measurement setup compared to the use of a signal generator and oscilloscope. The measured spectra are transformed to the time domain via an inverse fast fourier transformation (IFFT) and multiplication by the spectrum of the Ricker wavelet with f_c = 750 MHz and a -3 dB bandwidth between 440 MHz and 1050 MHz to get similar results as with time-domain measurements. This approach is mathematically described by

$$Y(f) = \Psi(f) \cdot H(f) \bullet\!\!-\!\!\circ\, y(t) = \psi(t) * h(t)\,, \tag{5.1}$$

where $Y(f)$, $\Psi(f)$, and $H(f)$ are the convolved data, the Ricker wavelet, and the measured impulse response in frequency domain, respectively, $\bullet\!\!-\!\!\circ$ is the (inverse) fourier transform operator, and $y(t)$, $\psi(t)$, and $h(t)$ are the corresponding data in time domain. Each frequency domain measurement is performed from 5 MHz to 3 GHz with a step size of 5 MHz to cover the relevant frequency range of the Ricker wavelet (see (2.51) and Fig. 3.11). For the IFFT a value of 0 for 0 Hz is added. These parameters correspond to a

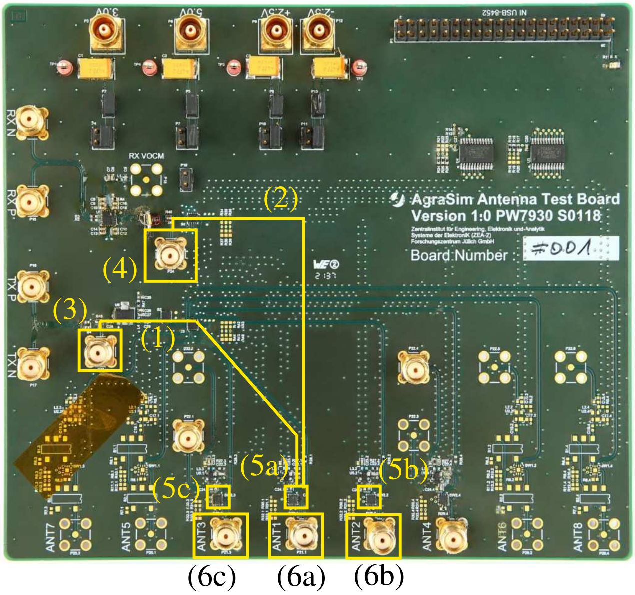

Figure 5.1: Evaluation board that contains the analog circuits of the monitoring system.

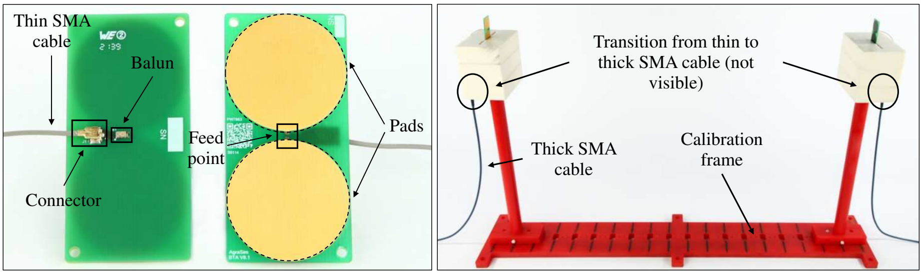

(a) (b)

Figure 5.2: (a) Single circular bowtie antennas front and back side. (b) Measurement setup for WARR and reflection measurements in air.

time domain measurement of 200 ns duration and a sampling interval of about 0.33 ns. Furthermore, the signals are extended by zero-padding (2.47) in the frequency domain such that a temporal resolution of 1.3 ps results after IFFT.

The evaluation board is used for the verification of the analog design of the monitoring system and contains all essential components of the Tx and Rx circuits (Fig. 5.1). The

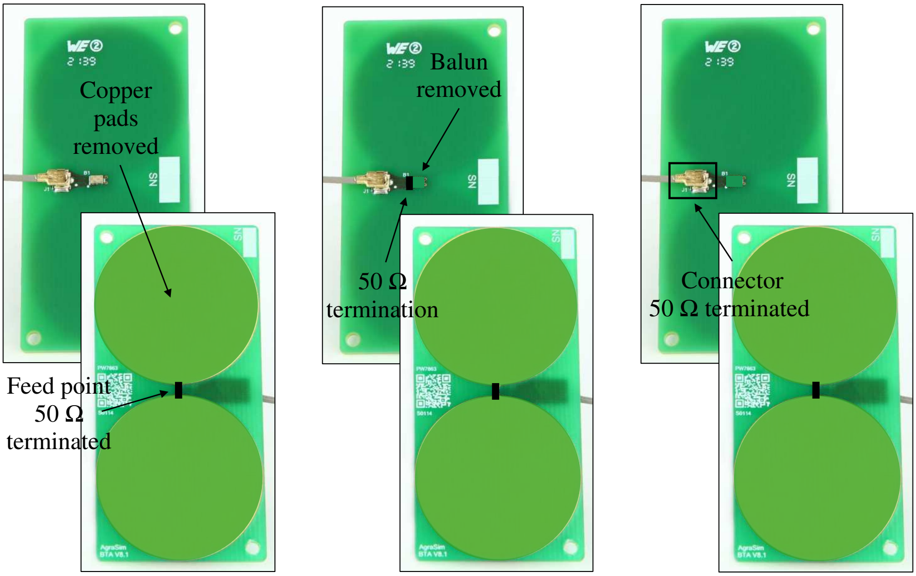

(a) (b) (c)

Figure 5.3: Different antenna versions to analyse the antenna reflections.

yellow lines and numbers in Fig. 5.1 correspond to the labels in Fig. 3.10. The ports of the VNA are calibrated with an electronic calibration kit via a short-open-load-through calibration to guarantee highly accurate measurements [101]. The calibrated ports are connected to the Tx and Rx port of the evaluation board (numbers (3) and (4) in Fig. 5.1). Tx and Rx ports are used to feed the signal in and out to the board. Each antenna port, i.e., (6a) for channel 1, (6b) for channel 2 and (6c) for channel 3, has its own SP3T switch (5a - 5c). The Tx channel (1) and Rx channel (2) from Tx port (3) or Rx port (4) to antenna port 1 (6a) are highlighted as an example (yellow lines). Other components as, e.g., amplifiers are not highlighted in this figure. The micro strip lines on the evaluation board between Tx or Rx port and the respective antenna ports (6a - 6c) are of different length and provide different Tx or Rx instrumental delays on the boards. For the measurements in this work, channels 1, 2 and 3 are used, where channel 1 is highlighted (yellow lines). For channels 2 and 3 only the corresponding SP3T switches (5b, 5c) and antenna ports (6b, 6c) are highlighted. A channel contains all components from the input port to the output port on the board. The antennas are self designed circular bowtie antennas with a pad diameter of 2.7 cm (Fig. 5.2a). On the backside of the antenna printed circuit board (PCB), the connector and a balun are positioned. To connect the antenna to the evaluation board, a 15 cm thin and flexible SMA cable is connected to the antenna PCB via a micro coaxial connector. The thin SMA cable is then connected to a longer, more rigid

SMA cable, which in turn is connected directly to the antenna port on the evaluation board (Fig. 5.2b). This combination of two different cables corresponds to the setup of the final GPR system setup.

The reflections from the antennas are a crucial part of the calibration approach derived in this work. To gain a better understanding of the antenna reflections, three antenna variants are measured in addition to an unmodified bowtie antenna (Fig. 5.3). In the first antenna variant, the feed point is terminated with 50 Ohm and the copper pads are removed (Fig. 5.3a). In the second antenna version, the balun is removed and replaced by a 50 Ohm resistor (Fig. 5.3b). In the last antenna version, the outer and inner conductors of the thin SMA cable are directly terminated (Fig. 5.3c). Thus, by comparing the reflections from the antenna variants, conclusions can be drawn about the causes of the reflections.

To verify the calibration via internal reflection measurements, a setup is selected in which individual antennas are placed in air. The air measurements are performed by mounting two single circular bowtie antennas on the calibration frame using foam blocks shown in Fig. 5.2b, where the distance between the antennas can be varied in 5 cm steps. In contrast to the first measurements presented in section 4.2.2, the antennas have a minimum distance of 60 cm to guarantee far field conditions. Further, the antennas are positioned 50 cm above the ground. For this setup, time-zero can be determined using standard methods and compared to the novel developed method. This measurement is repeated for varying antenna spacings to linearly extrapolate the arrival times for $d = 0$ to determine time-zero similar to the measurements in section 4.2.2. For the described setup, time-zero is determined for channel 1 (Tx) and channel 2 (Rx) with $t_0 = 18.975 \pm 0.003$ ns. For the internal reflection measurements, the same value must result if the arrival time of the reflected signal is determined correctly.

This setup also allows to analyze the reciprocity of the measurements. For this purpose, the transfer functions $H(\omega)$ of the Tx channels 1 and 2 are measured as an example. Only if these have a linear phase response, i.e., a constant group delay $\tau = -\delta\varphi(\omega)/\delta\omega$ with $\varphi(\omega) = \arg H(\omega)$, the envelope of the Ricker wavelet remains undistorted. This is particularly important if the temporal offset of reciprocal measurements is to be determined via a cross correlation or if a point is to be defined for finding the arrival time. The envelope of the Ricker wavelet can be approximated with the help of the Hilbert transformation $\mathcal{H}$. For this, the analytical signal is defined as $\psi_\mathrm{a}(t) = \psi(t) + j\mathcal{H}\{\frac{1}{\pi t} * \psi(t)\}$ and the instantaneous amplitude or envelope is calculated as $|\psi_\mathrm{a}(t)|$.

To test different factors influencing the calibration method, an antenna array is used in addition to the individual antennas (inlet Fig. 5.4). With a size of 4×8 this antenna array is smaller than the actual 8×8 array for each tile of the final GPR system, but still allows to analyse the influence of neighbouring antennas on the internal reflections. In addition to the influence of the array structure on the internal reflection measure-

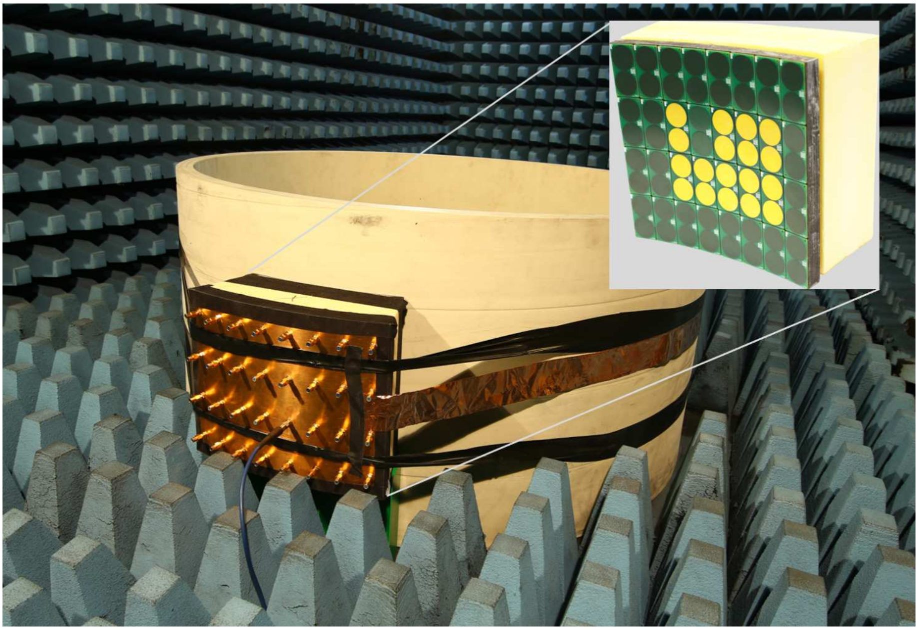

Figure 5.4: Lysimeter setup with antenna array in an anechoic chamber. Inlet shows front of antenna array.

ments, it is also quantified whether the internal reflections are influenced by whether the antenna is placed in the air or attached to the lysimeter. For this purpose, both individual antennas and the antenna array are attached to a PVC lysimeter (Fig. 5.4). To quantitatively assess the stability of the reflected and coupled signals in section 5.2.2, the instability index defined by Liu et al. (2018) [102] is used:

$$\zeta = \sqrt{\frac{\frac{1}{N}\sum_{i=K}^{M}\sum_{j=1}^{N}|y_j(t_i) - \overline{y(t_i)}|}{\sum_{i=K}^{M}|\overline{y(t_i)}|^2}}, \tag{5.2}$$

where N is the number of repeated measurements, $y_j(t_i)$ is the magnitude of the jth measurement at time t_i, K and M are the starting and ending points of the GPR wavelet, and $\overline{y(t_i)}$ is the mean magnitude of the GPR traces at time t_i.

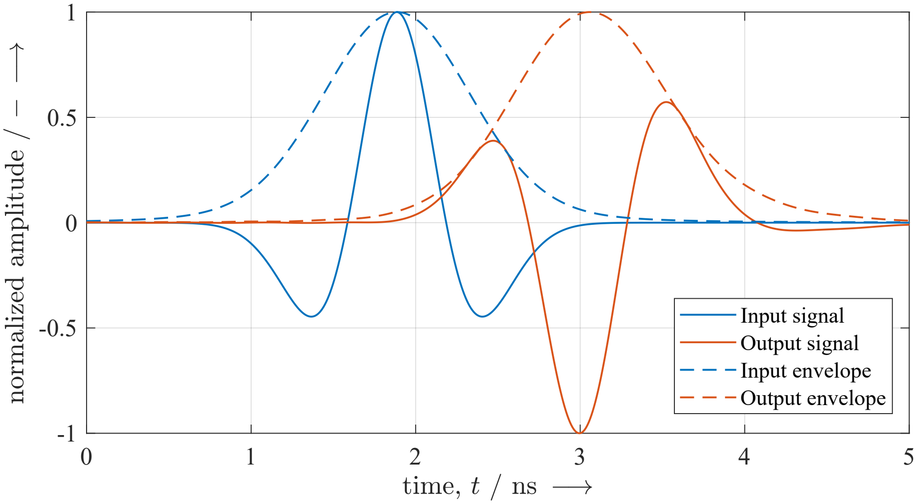

Figure 5.5: Normalized input and output signals of Tx channel with corresponding envelopes.

5.2 Results

5.2.1 Analysis of reciprocal measurements

In this section potential errors the reciprocal measurements on the time-zero determination are analyzed. According to (3.45), the reciprocal measurements contain essential information for the calibration. As long as the waveforms are identical, times of characteristic points such as the maximum amplitude can be used in (3.45). However, this only applies if the different Tx and Rx channels have constant group delays to prevent altering the signal's shape. Fig. 5.5 shows the input and output signal of the Tx channel 1 together with their instantaneous amplitudes, i.e., the envelopes. Except for an inverted output signal, the envelopes are almost the same, which indicates a linear phase response of the Tx channel. However, if the group delay of the Tx channels 1 and 2 is considered, a non-constant behaviour is seen, which results in a distortion of the input signals. The offset is caused by different micro strip lengths of the channels and is of no relevance for the reciprocity of the signals. However, the residuals of the group delay of both channels show that the variation of the group delay is not identical, resulting in differences in the amplitudes of the output signals. Thus, perfect reciprocity cannot be assumed for a reciprocal measurement between two channels.

To analyze the impact of this effect on measurements between different antenna chan-

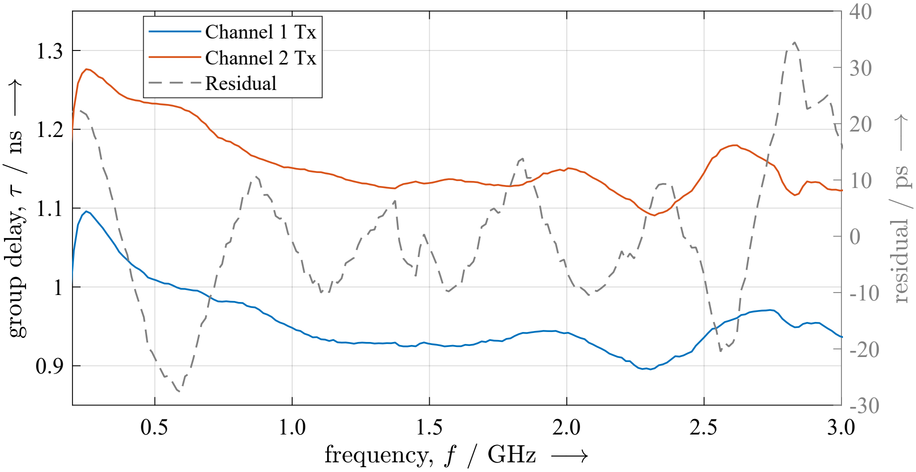

Figure 5.6: Group delay of Tx channels 1 and 2, respectively.

nels, reciprocal measurements are performed between antenna channels $1-2$, $1-3$ and $2-3$ with the setup shown in Fig. 5.2b and for varying antenna distances. Since the signals pass through different Tx and Rx channels in reciprocal measurements, it is possible that the signals of reciprocal measurements differ more than in the idealized setup in section 4.2.2. The same two antennas are used for all measurements between different channels. Fig. 5.7 shows the reciprocal signals between channels 1 and 2 for an antenna separation of 60 cm. Next, the time differences between the first three peaks, i.e., (i) $\Delta t_{\text{peak 1}}$, (ii) $\Delta t_{\text{peak 2}}$ and (iii) $\Delta t_{\text{peak 3}}$, and (iv) the time shift t_{shift} that maximizes the cross correlation $R(t_{\text{shift}})$ between the signals are calculated. The cross correlation is used as it exhibits the highest signal-to-noise ratio (SNR) amongst the calculated values. Only for identical waveforms the same values for all four differences would result. For channel combinations $1-2$ and $1-3$, the time differences between the second and third peak are almost identical to the calculated cross correlation (Tab. 5.1). Using the first peak, the time difference is about 2 to 3 ps smaller. For channel combination $2-3$, the

Table 5.1: Time differences of 1st, 2nd and 3rd peak of reciprocal signals. For further comparison, the calculated cross correlation is given.

channels	$\Delta t_{\text{peak 1}}$ / ps	$\Delta t_{\text{peak 2}}$ / ps	$\Delta t_{\text{peak 3}}$ / ps	$\max_t R(t)$ / ps
1 - 2	-64.9 ± 2.8	-67.2 ± 0.6	-67.6 ± 0.4	-67.0 ± 0.4
1 - 3	80.2 ± 10.6	83.5 ± 2.3	83.7 ± 1.4	83.5 ± 1.4
2 - 3	147.8 ± 1.8	149.7 ± 0.7	151.0 ± 0.7	152.5 ± 0.4

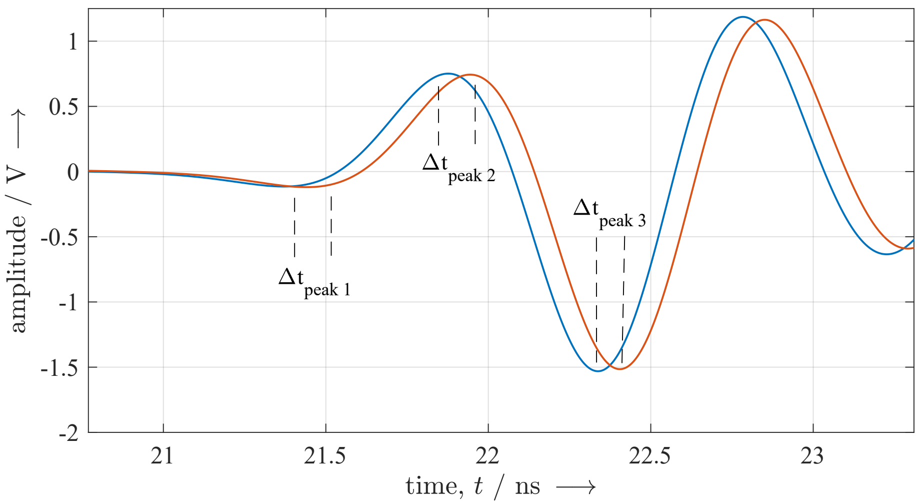

Figure 5.7: Reciprocal signals for two measurements between channels 1 and 2 with 60 cm antenna spacing.

differences are larger with up to about 5 ps between the first peak and the cross correlation. Regardless of the channel combination, the uncertainties are largest when using the first peaks, whereas the third peaks and the cross correlation give similar results regarding accuracy. This is probably because the higher standard deviation of $\Delta t_{\text{peak 1}}$ indicates a lower SNR for the first peak, and second, there is a systematic deviation of approximately 3 ps compared to the other three differences. However, the maximum difference between the time differences is less than 5 ps, so the first peak is also sufficiently accurate for the calibration approach. Furthermore, the measurements show that the channels do not have constant group delays as otherwise the waveforms would remain the same and consequently there would be no variation in the time differences of different reference points. In the following, the times of the maximum amplitudes within the signals are used for the comparison of reciprocal measurements and for the calculation of time-zero, as these are easy to detect and provide similarly accurate results as the cross correlation.

5.2.2 Analysis of internal reflections

In this section, the error contribution of the internal reflection measurements to the presented time-zero calibration approach is analyzed. First, the cross-coupled signals for the SP3T in Tx and Rx mode are examined (Fig. 5.8). As expected, the first coupling (from about 4 ns to 8 ns) has a higher amplitude than the second coupling (from about

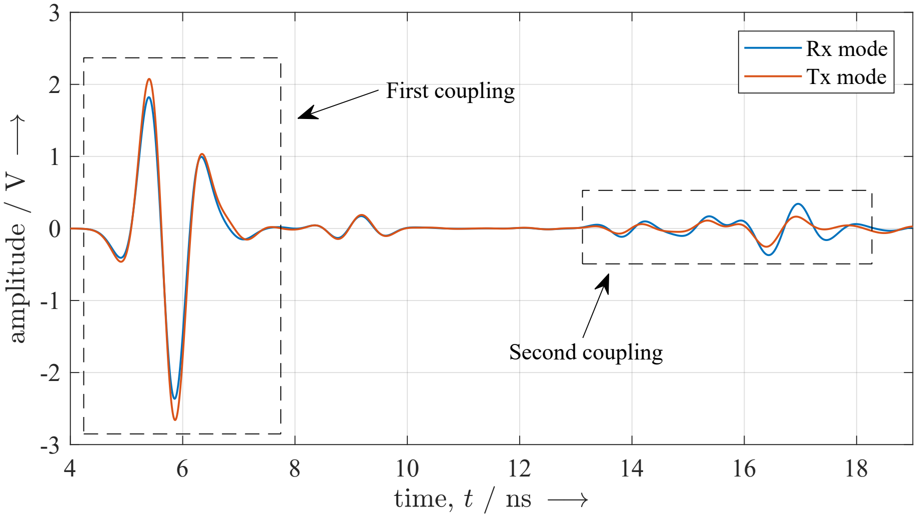

Figure 5.8: First and second coupling for channel 1 in Tx and Rx mode.

13 ns to 18 ns). The signal component at about 9 ns originates from a reflection on the evaluation board and is not relevant for the further analysis. The first coupling has higher signal amplitudes in Tx mode compared to Rx mode because the switch has a lower isolation between the circuits in Tx mode (Fig. 3.11). It follows that the second coupling in Tx mode has a smaller amplitude, since initially more energy is coupled into the Rx channel during the first coupling. To better understand the second coupling, the three antenna variants plus a normal bowtie antenna are measured at this point. To obtain a high spatial resolution, the VNA is operated at its maximum bandwidth of 5 MHz to 26 GHz. Fig. 5.9 shows the resulting scattering measurements transformed to time domain and illustrates that reflections are caused by (i) the transition of the thick SMA cable to the thin antenna cable, (ii) the connector on the antenna PCB, (iii) the balun and (iv) the antenna feed point and antenna pads. These reflections form the combined second coupling that is shown in Fig. 5.8. The amplitude noise of the second coupling in Tx and Rx mode and for the air measurements for channel 1 is shown in Fig. 5.10. The graph shows the mean value (solid line) and the standard deviation (pale error band) for each measurement point with $n = 16$ measurements. The arrows mark a reference point within the coupling, here the minimum, that will be used in section 5.2.3. For the Tx mode, the amplitude noise shows the highest values in the range from 22 ns to 24 ns. The second coupling in Rx mode, on the other hand, is stable over the entire range. Around the minimum, which serves as the reference point for calculating (3.45), both switch modes exhibit stable signals with low amplitude noise. The same investigations were repeated for channels 2 and 3 with measurements in air and with the antennas taped

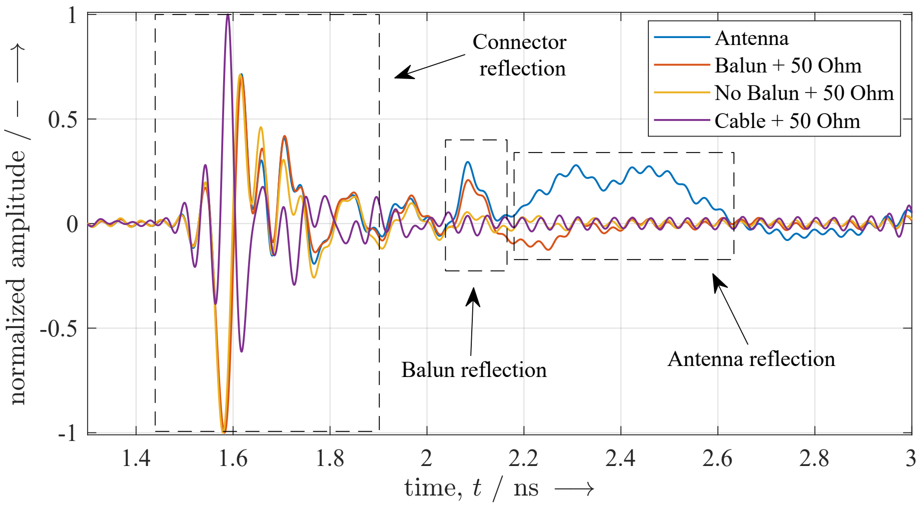

Figure 5.9: Antenna reflections for different configurations.

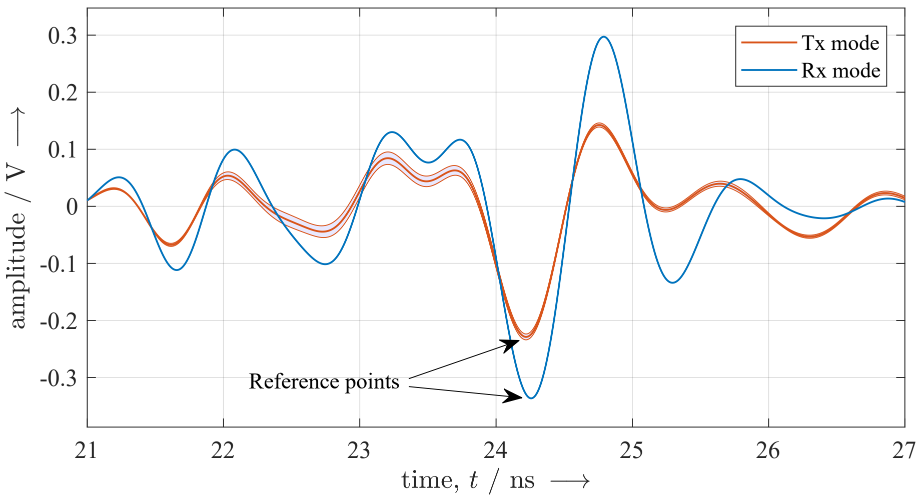

Figure 5.10: Measurement uncertainty for multiple measurements in Tx and Rx mode with channel 1 and antenna placed in air.

to the lysimeter (Tab. 5.2). All measurements show more stable signals in Rx mode, but around the reference point stable signals could always be observed independent of the switch mode. The more unstable noise behavior in Tx mode and especially in the area

Table 5.2: Instability for internal reflection measurements with channels 1, 2 and 3 in Tx and Rx mode.

	Channel 1		Channel 2		Channel 3	
	Tx	Rx	Tx	Rx	Tx	Rx
ζ_{air} / %	8.91	0.44	1.85	0.68	9.20	3.76
$\zeta_{\text{lysimeter}}$ / %	5.18	0.58	0.18	0.22	5.40	2.51

Table 5.3: Timing offset t_{offset} for Tx and Rx mode to identify the arrival time of the antenna feed point reflection.

channels	$t_{0\,\text{ref}}$ / ns	R^2 / -	$\bar{t}_{\text{offset Tx}}$ / ns	$\bar{t}_{\text{offset Rx}}$ / ns
1 - 2	18.927 ± 0.002	1.0000	1.497 ± 0.000	1.552 ± 0.001
1 - 3	18.826 ± 0.003	1.0000	1.522 ± 0.006	1.559 ± 0.001
2 - 3	19.034 ± 0.003	1.0000	1.493 ± 0.001	1.548 ± 0.001

before the minimum has no obvious reason and would have to be investigated further in the future. In principle, both switch modes are suitable candidates for the internal reflection measurements and will be further analyzed and compared in section 5.2.3.

5.2.3 Determination of time-zero

As described in section 3.4.2 and shown in section 5.2.2, the antenna feed point reflection is superimposed by further reflections from components close to or on the antenna PCB. The approach described by (3.48), (3.49) and (3.50) is used for channel combinations $1-2$, $1-3$, and $2-3$, respectively. A distinction is made between the offsets for Tx and Rx mode. In addition, the $t_{0\,\text{ref}}$ determined via a wide angle reflection and refraction (WARR) measurement including the associated R^2 value is given for each channel combination to provide an accuracy estimate. The calculated $\bar{t}_{\text{offset}}$ differ by up to 11 ps in Rx mode and up to 29 ps in Tx mode for the different channel combinations, respectively. The average of all calculated offsets from a total of 24 measurements (8 per channel combination) is calculated with $\hat{t}_{\text{offset Tx}} = 1.504 \pm 0.016$ ns and $\hat{t}_{\text{offset Rx}} = 1.553 \pm 0.006$ ns. These accuracy values already include the errors caused by the time-zero reference and the violation of the reciprocity criterion. Thus, both systematic and random errors are included in the resulting data. It should be noted that the accuracy results are calculated based on the three available antenna channels. For the actual system, these measurements should be repeated with more channel combinations to obtain a higher statistical significance.

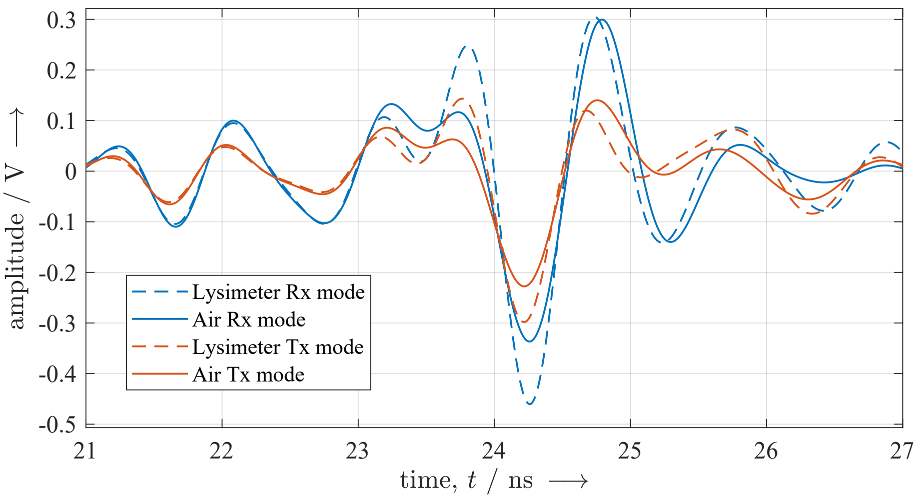

Figure 5.11: Comparison between reflection and coupling measurements with antenna either in air or taped to the lysimeter.

5.2.4 Material influence on reflections

This section describes the influence on the second couplings introduced by the lysimeter wall. This influence is analyzed by taping the antennas to the outer wall of a lysimeter. First, the reflected signals at channel 1 are compared with the antenna (i) in air and (ii) at the lysimeter for Tx and Rx mode (Fig. 5.11). The first signal components between 21 ns and 23 ns are almost identical, since these signal components are caused by reflections at the cables and these components are not influenced by the lysimeter. For the following signal components after 23 ns, the signals show differences. The antenna feed point reflection is more clearly separated from the reflections caused by connectors and the balun. In addition, the lysimeter reflection shows oscillating signal components after 26 ns, which are probably caused by multiple reflections within the 3 cm thick lysimeter wall.

To verify that the universal offset $\hat{t}_{\mathrm{offset}}$ for Tx and Rx mode, respectively, is still valid for measurements at the lysimeter, measurements are made with two antennas on opposite sides of the lysimeter and time-zero is calculated using (3.45) with either $\hat{t}_{\mathrm{offset\,Tx}} = 1.505$ ns or $\hat{t}_{\mathrm{offset\,Rx}} = 1.553$ ns. The antennas are connected successively to the three antenna ports. For comparison, the channel dependent offsets $\bar{t}_{\mathrm{offset\,Tx}}$ and $\bar{t}_{\mathrm{offset\,Rx}}$ (Tab. 5.3 last two columns) of the respective channel combinations are used additionally to the universal $\hat{t}_{\mathrm{offset\,Tx}}$ and $\hat{t}_{\mathrm{offset\,Rx}}$. The measurements are repeated 10 times for each channel combination. Theoretically, the same time-zero should result for the lysimeter mea-

Table 5.4: Error for time-zero when using either the universal $\hat{t}_{\text{offset}}$ or the channel specific $\overline{t}_{\text{offset}}$ in Tx and Rx mode, respectively.

channels	$\hat{\epsilon}_{\text{Tx}}$ / ps	$\overline{\epsilon}_{\text{Tx}}$ / ps	$\hat{\epsilon}_{\text{Rx}}$ / ps	$\overline{\epsilon}_{\text{Rx}}$ / ps
$1-2$	-7	0	4	5
$1-3$	13	-6	12	6
$2-3$	2	13	11	16

surements as for the air measurements. The respective average errors for time-zero, i.e., $\hat{\epsilon}_{\text{Tx}}$, $\overline{\epsilon}_{\text{Tx}}$, $\hat{\epsilon}_{\text{Rx}}$ and $\overline{\epsilon}_{\text{Rx}}$ when using $\hat{t}_{\text{offset Tx}}$, $\overline{t}_{\text{offset Tx}}$, $\hat{t}_{\text{offset Rx}}$ and $\overline{t}_{\text{offset Rx}}$, respectively, are summarized in Tab. 5.4. For channel combinations $1-2$ and $1-3$, the errors are lowest when using the channel specific $\overline{t}_{\text{offset}}$. Only for the channel combination $2-3$ the error is higher when utilizing the channel specific offset instead of the universal offset. Consequently, in almost all measurements the calculated time-zero for the respective channel combinations changes after the antennas are attached to the lysimeter. This suggests either an actual change in time-zero, which can be corrected by the internal reflection measurements, or a systematic error caused by the lysimeter. Probably the errors are caused by a combination of these two possibilities. When the universal $\hat{t}_{\text{offset}}$ is used for the calibration, the errors become larger as expected except for channel combination $2-3$. A possible reason for that are measurement inaccuracies in the lysimeter measurements caused, for example, by loose connections between SMA cables. In summary, using the universal offsets results in maximum time-zero errors of 13 ps in Tx mode and 12 ps in Rx mode provided that time-zero has not changed. In the following, a pure systematic error of 13 ps caused by the lysimeter is assumed as a worst-case estimate. On average, the Tx mode provides more accurate results than the Rx mode. To reduce the systematic error caused by the lysimeter, the WARR measurements can be performed directly with PVC placed in front of the antennas. This allows $\hat{t}_{\text{offset}}$ to be optimised for the lysimeter measurements. The influence of the lysimeter filling on coupling signals between neighbouring antennas was analyzed in section 4.2.3 and is less than 10 ps for small antenna spacing. Therefore, the lysimeter filling is expected to have a small influence on the second coupling.

5.2.5 Influence of antenna position

This section concludes the analysis of influencing factors on the internal reflections by examining the influence introduced by the antenna array on the internal reflection measurements. For this purpose, reflection and coupling measurements were exemplary performed with six antennas of the antenna array. The used antennas are marked in the inset of Fig. 5.12, i.e. antennas 8, 13, 20, 21, 25 and 32. The antennas were connected

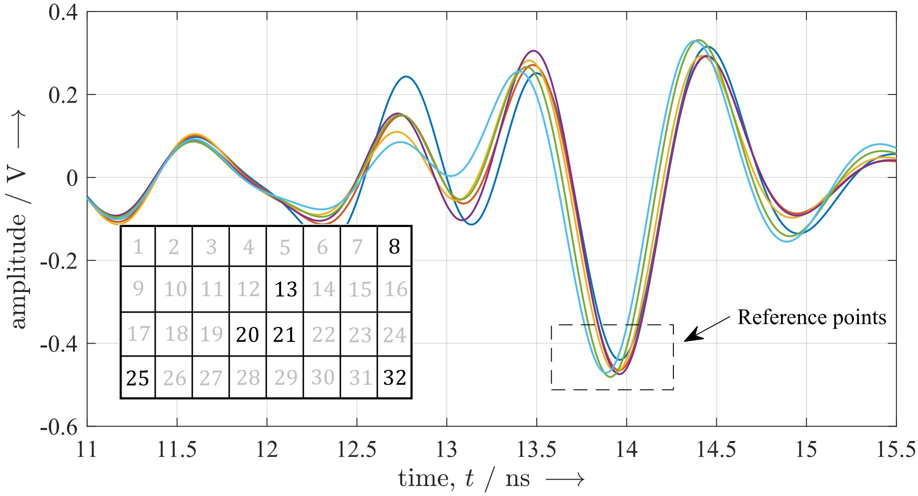

Figure 5.12: Second coulings for antennas at different positions within the antenna array.

to channel 1 at the evaluation board, respectively, to exclude channel related dependencies. The reflections from different antennas show variations in the signal amplitudes and phases. To assess whether these differences are caused by the antennas themselves or by the respective position in the array, measurements were carried out in which the antennas were removed from the array and attached individually to the lysimeter. Then, the time points of the signal's minima for antennas 8, 25 and 32 were compared for antenna positioning in the array and positioning alone at the lysimeter (Tab. 5.5). The time offset of the minima is up to 77 ps for antennas 8 and 32 in Rx mode within the array. However, this offset is almost the same when the antennas are removed from the array and positioned at the lysimeter individually, so the difference is due to tolerances in the antenna manufacturing. Nevertheless, the offsets for antennas 8 and 32 differ by 14 ps for the array and single measurement in Rx mode. In Tx mode the differences are smaller with a maximum error of 8 ps. In general, the minima occur later for the array measurements than for the individual antenna measurements. Consequently, the arrangement as an antenna array has an influence on the reflections. The differences between the reflections are mainly caused by the antennas tolerances. This also shows that despite careful preparation of the antennas, fabrication related differences occur. This underlines the relevance of the presented in situ calibration. As in section 5.2.4, the array measurements yield more accurate results for the internal reflection measurements in Tx mode.

To sum up, reciprocal measurements are performed to correct non-uniform trigger

Table 5.5: Time differences of minima within the measured signals for antennas 8, 25 and 32. Minimas are compared for (i) antennas placed at the lysimeter individually and (ii) antennas placed within the antenna array.

	Tx			Rx		
	8 - 25	8 - 32	25 - 32	8 - 25	8 - 32	25 - 32
Single / ps	42	57	15	44	63	19
Array / ps	41	64	23	52	77	25
Error / ps	-1	7	8	8	14	6

times of the base boards (BABs). The magnitude of the error induced by reciprocal measurements was investigated. It was found that this error was limited to a maximum of 5 ps, whereas in most cases the error was below 3 ps. Additionally, reflecting signals are required for the complete calibration. To analyze the behavior of the reflecting signals, measurements were first performed with individual antennas in air. It was observed that the relevant reflection from the antenna feed point is superimposed by other reflections, caused by the cable connector on the antenna PCB, among others. To identify the antenna reflection, a constant time offset was determined with the help of a classical calibration approach. The analysis of this offset shows that a universal offset can be determined with an accuracy of ± 16 ps in Tx mode and ± 6 ps in Rx mode. Further, the influence of the lysimeter itself on the antenna reflections is estimated to be 13 ps. Finally, effects caused by the individual antennas were investigated. The largest deviation of up to 65 ps is caused antenna fabrication variations. The arrangement of individual antennas within the antenna arrays has an influence of up to 14 ps.

5.3 Conclusions

In this chapter, the developed calibration method for the tile GPR monitoring system was applied and evaluated. This calibration method is mainly based on the combination of reciprocal measurements and so-called internal reflection measurements. It was observed that the reflected signals are most stable when the Tx-Rx switch is in Rx mode. However, operating the switch in Tx mode reduces the influence of the lysimeter and the individual antennas on the proposed calibration approach. Also, the measurement procedure for the internal reflection measurements is faster to execute when the switches are in Tx mode as the measurement of internal reflections can be integrated into the actual tomography measurements. When internal reflections would be measured with the switch in Rx mode, every DAC would have to generate twice the amount of signals leading roughly to a doubling of measurement time. Therefore it is adviced to perform the internal reflection measurements with the switch in Tx mode. The analysis of the reciprocity of the antenna channels has shown that the different channels do not have constant group delay times and therefore cause altering waveforms. However, these changes are minimal and have a negligible influence on the accuracy of the calibration. Measurements show that an in situ calibration approach that can identify variations in the measurement setup up to the antennas is essential. Assuming completely identical array channels up to the antennas with identical instrumental delays leads to errors of up to 64 ps in Tx mode. This error can be reduced to 8 ps by the presented calibration. In addition, the lysimeter also has an influence on the internal reflections, which is estimated at a maximum of 13 ps. In total, this results in a worst-case systematic error for time-zero of 8 ps +13 ps = 21 ps. However, the lysimeter influence could be reduced by initially performing WARR measurements with PVC placed in front of the antennas. The method is thus able to calibrate the multichannel GPR monitoring system in situ for arbitrary transmitter-receiver combinations with sufficient accuracy. The additional effort for the calibration measurements is minimal, since the reflection and coupling measurements can be directly integrated into the actual measurement of the soil and, in particular, the existing antenna setup can directly be used without any mechanical modifications to perform the calibration. Note that the given accuracy does not contain errors due to imperfect synchronization between channels, which will be investigated in chapter 6. If the universal offset is also included in the full-waveform inversion as an additional parameter, it is also possible to increase the time-zero accuracy even further. The presented approach has the potential to be used within every GPR system that utilizes antennas which can operate in transmit and receive mode.

Chapter 6

Verification at prototype system

This chapter concludes the experimental part of this thesis with analyses of the current state of the ground penetrating radar (GPR) monitoring system. First, the setup with all relevant components is presented in section 6.1. Furthermore, the temporal stability of the system is analyzed. A distinction is made between jitter, drift and phase ambiguities, where phase ambiguities are caused by the resynchronization of the clocks. Afterwards, a number of measurements from the previous chapter 5 is repeated with the current setup, whereby measurements are now carried out between two base boards (BABs) including synchronization, triggering, and final hardware components such as digital-analog converters (DACs) and analog-digital converters (ADCs). This way, the performance of the calibration can be determined under real conditions.

6.1 Experimental Setup

The current prototype setup consists of a trigger source and trigger distribution board that together imitate the functionality of the main module (MAM) and two prototypes of the final BABs (Fig. 6.1). The trigger source is responsible for generating signals for synchronizing and triggering the two BABs while the trigger distribution board distributes the generated signals to the BABs. A MAM interface is placed between the trigger distribution board and the BABs, respectively, which is needed for the preparation of the synchronization and trigger signals. In the final setup, the trigger source, trigger distribution and MAM interface will be integrated directly into the MAM. The DACs on the BABs are programmed to generate a waveform, with the waveform stored in a text file. In section 6.2 a predistorted Ricker wavelet is used. The wavelet was adapted so that an ideal Ricker wavelet arrives at the ADC after passing through the Tx and Rx channels. Previously, a Ricker wavelet was always assumed to be the transmitted signal. This results in slight changes in the measured signal shapes compared to chapters 4 and 5. In the final system predistortion will also be used to optimize signal-to-noise ratio. DACs and ADCs generate and sample signals at 4 GSa/s. In the prototype system, the ADC can hold data of up to 4 μs in its memory and the DAC can generate signals with a length of

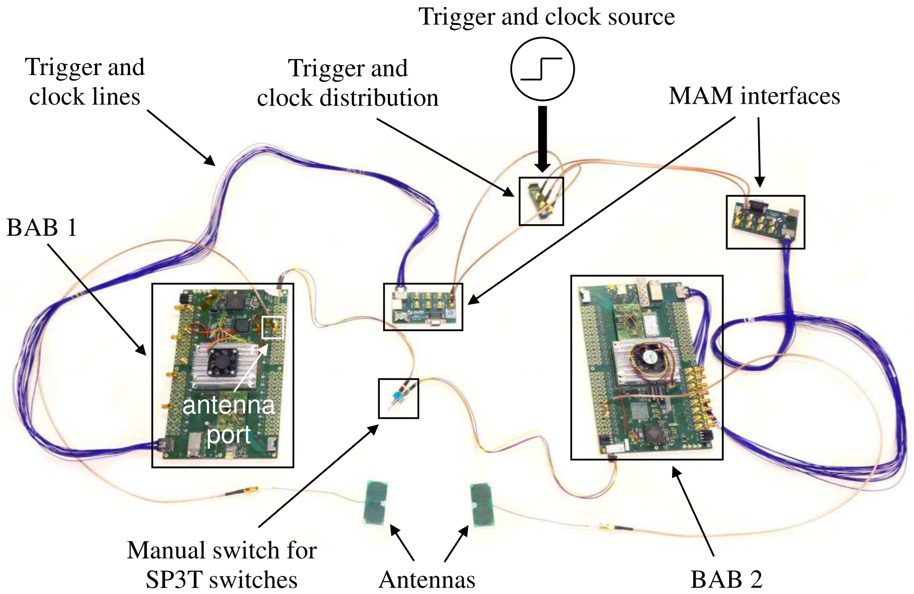

Figure 6.1: Experimental setup composed of trigger source, trigger distribution, MAM interfaces and BABs.

128 ns. The ADCs have not yet been amplitude calibrated, so the results section shows the measured ADC counts instead of voltages. The sampled signals are interpolated to have a final timing resolution of 1 ps. In the preliminary version of the BABs, neither the SP8T nor the SP3T switches are programmable. Therefore, the SP8T switches are set such that the measurement is always made with antenna channel 57. The respective SP3Ts of channel 57 per board are manually switched between Tx and Rx mode via a manual switch. In addition to the SP3Ts and SP8Ts, the programmable gain amplifier (PGA) in the Rx circuit cannot be programmed. Instead, the PGA is bypassed, which results in 26 dB of gain missing in the signal chain. This is not necessarily a problem for the measurements in this work and is only mentioned here, as the PGA is relevant only for the measurements with soil between the antennas to guarantee sufficient signal amplitudes. For the measurements in sections 6.2.2 and 6.2.3, the circular bowtie antennas are used and each measurement is repeated 64 times and averaged. In contrast to the measurements in chapter 5, the internal reflection measurements are always performed with the SP3T in Tx mode. This way, the data acquisition time can be reduced significantly, as the internal reflection measurements and the transmission measurements between two antennas can be carried out simultaneously. The clock (CLK) distribution from the MAM to two exemplary BAB is shown in Fig. 6.2. The system first receives an external 25 MHz clock, which is multiplied within a first clock generation block in

the MAM via two phase-locked loops (PLLs) first to 125 MHz and then to 2.5 GHz. The following frequency divider outputs the original clock frequency of 25 MHz, whereby passing through the clock generation block reduces the jitter in the clock signal. To be able to connect the 13 BABs of the lowest ring to the MAM in a star configuration in the final system, the first clock generation block is followed by two further clock generation blocks (clock generation 2.1 and clock generation 2.2 in Fig. 6.2), since each frequency divider (Freq. Div. in 6.2) has only seven clock outputs. At the input of both BABs, the 25 MHz CLK is again fed into a clock generation block, which multiplies the clock to 250 MHz and operates the radio frequency (RF) PLL. The RF PLL finally multiplies the clock frequency to 12 GHz, which is reduced to 4 GHz by a final frequency divider. The DAC and ADC are operated with these 4 GHz. Due to the interconnection of the BABs in the final GPR monitoring system, i.e., star configuration from the MAM to the 13 BABs in the lowest ring and then in a chain to the BABs in the top ring, different cable lengths result for CLK and trigger signals for different BABs. Consequently, the CLKs and triggers reach the different BABs with time delays and lead to trigger offsets. In addition, the trigger offsets can vary due to the resynchronization of the system and drift over time. Synchronization is necessary to stabilize and lock the CLKs on the BABs. Both factors, resynchronization and drift, are analyzed in section 6.2.1. The in situ calibration has the potential to eliminate the need to compensate for clock and trigger times. The prototype setup simulates two BABs positioned on the lowest ring at the lysimeter within the star configured trigger distribution.

6.2 Results

6.2.1 Temporal stability

In previous measurements with the current prototype setup, the temporal short-term stability, i.e., jitter, was examined (Fig. 6.3). A distinction is made between jitter within the BAB (intra) and between two BABs (inter). To measure the intra BAB jitter, the antenna port of channel 57 on BAB 1 was connected to the antenna port of channel 59 on BAB 1 via an SMA cable. The SP8Ts were hard-wired to allow this measurement. For the measurement of the inter BAB jitter, antenna port 57 of BAB 1 was connected to antenna port 57 of BAB 2 via an SMA cable. Then, for intra and inter BAB jitter estimations, a cosine with a fixed frequency in the range of 78 MHz to 1.3 GHz was generated at the DAC, passed the respective Tx and Rx channels and the phase deviation from the expected phase is calculated. The measurements show that the jitter for inter BAB measurements is always lower than for intra BAB measurements. The jitter is smaller than 50 ps for inter BAB measurements for frequencies larger than 300 MHz. Especially in the range close the center frequency of the Ricker wavelet of 750 MHz,

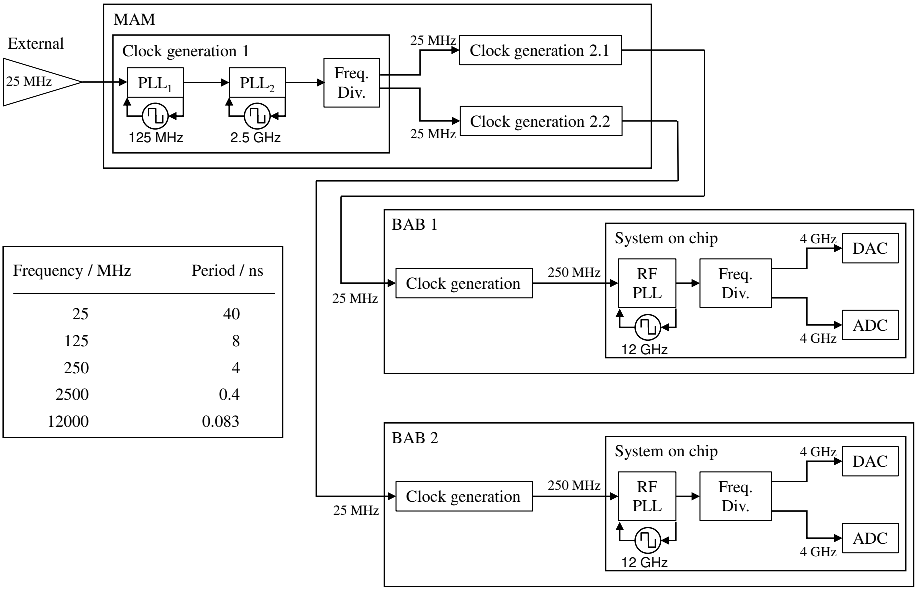

Frequency / MHz	Period / ns
25	40
125	8
250	4
2500	0.4
12000	0.083

Figure 6.2: Clock distribution on MAM and BABs.

the jitter is small with about 25 ps. This allows the jitter for transmission measurements to be easily reduced to the single-digit picosecond range by stacking. The jitter for the intra BAB measurements, i.e., for the internal reflection measurements, is only slightly higher in the frequency range around 750 MHz and thus guarantees precise measurements. The jitter is dominated by amplitude noise [103] and it is expected that the amplitude noise will be lower in subsequent versions of the BABs. Consequently, the jitter can be neglected for the calibration. While jitter can be reduced by stacking and does not significantly affect the time-zero calibration, the long-term temporal stability of the system must be investigated. Long-term temporal stability is influenced by potential drifts of the CLKs and by instabilities of the synchronization. To measure both influencing factors, the antenna ports of the BABs are connected via an SMA cable. For the measurement of the drift, the BABs are synchronised once at the beginning of the measurement series and the CLKs are then left to run freely. A measurement is taken every 10 minutes over 24 hours, with 10 signals being averaged for each measurement. To determine the influence of resynchronization, both BABs are resynchronised before each measurement, which causes the PLLs to lose their previously locked status and have to be re-locked. Here, a resynchronization is carried out every 5 minutes for 3 hours. In both cases, the times of the zero crossings before the maximum amplitude are compared. Zero crossings are used as the measurements with the current setup are influenced by signal leakage between clock and signal channels and the zero crossings

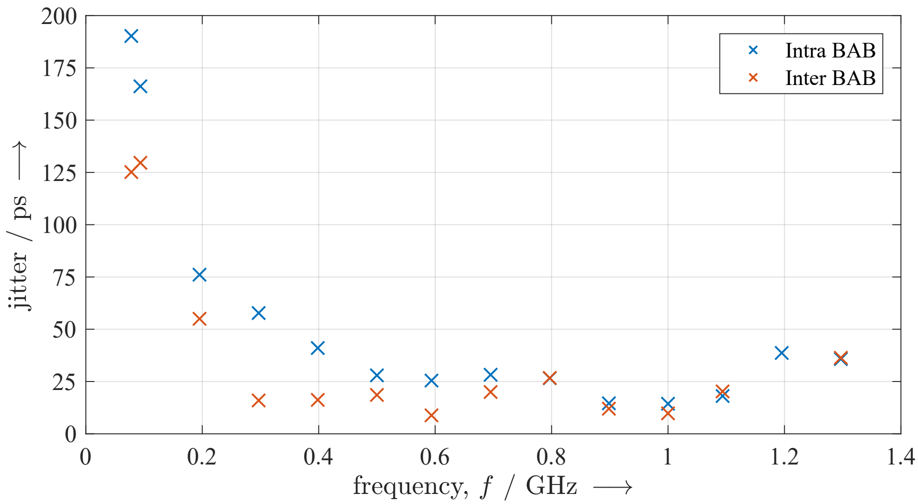

Figure 6.3: Jitter on a single BAB (intra) and between two BABs (inter). Adapted from [103].

are only slightly influenced by this leakage. The results are shown in Fig. 6.4. Note that different absolute times result for resynchronization (Fig. 6.4a) and drift (Fig. 6.4b) as the SMA cable connecting the BABs was changed between the two studies. The signal times vary by more than 3 ns for multiple resynchronizations. Here it is noticeable that the times vary in each case by multiples of 83 ps, which corresponds to the period of the RF PLL ($1/(12\text{GHz}) = 83$ ps). Consequently, resynchronization leads to phase ambiguities within the RF PLLs, which must be determined separately for each resynchronization. This measurement shows that a new calibration of the system after each switch-on or switch-off is essential to achieve the required time-zero accuracy. The drift measurements show that the signals can shift in time by more than 80 ps over a period of 24 hours. Even without the major influence of resynchronization, errors greater than the required 25 ps accuracy would occur if the system is initially calibrated and stable time conditions are afterwards assumed.

6.2.2 Transmission and internal reflection measurements

Wide angle reflection and refraction (WARR) measurements are conducted at eight distances between the antennas to obtain a reference for time-zero (Fig. 6.5). The antennas are mounted on the calibration frame as in chapter 5. The first direct air signal is followed by oscillations even after removing harmonic signal components at multiples of 250 MHz (the ADC clock frequency). These harmonics probably couple over to the Rx

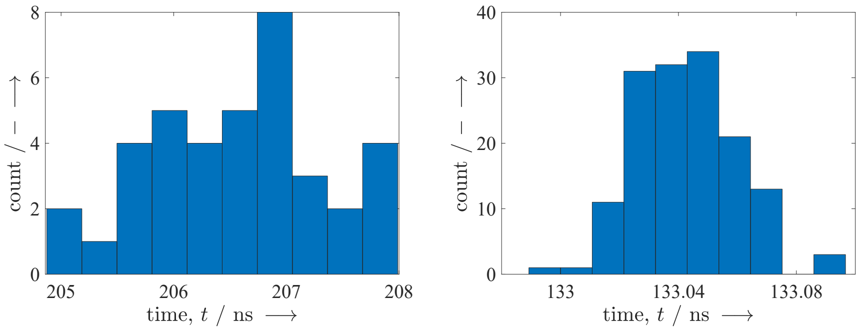

(a) Resynchronization (b) Drift

Figure 6.4: Times of zero crossings (a) for 38 BAB resynchronizations and (b) over 24 hours with measurements every 10 minutes and without resynchronization.

channel via close microstrip lines. This will be corrected by design in the next BAB version. Nevertheless, the Ricker wavelets are detectable for different antenna distances. Thus, the setup can be used to verify the calibration approach and to establish a time-zero reference. When analysing the internal reflections, both the first coupling and the second coupling are considered. The first coupling is measured for both BABs on the same channel 57 (Fig. 6.6). Nevertheless, there are differences in the arrival times for BAB 1 and BAB 2 of more than 1.3 ns. This supports the argument that it cannot be assumed that the instrumental delays within the BABs, i.e., $t_{\mathrm{Tx\,Rx\,1}}$ for BAB 1 and $t_{\mathrm{Tx\,Rx\,2}}$ for BAB 2, are identical for equal channels. So far it has been shown in section 5.2.5 that the antennas cause manufacturing-related and assembly-related instrumental delay differences of up to 77 ps. Due to the additional components such as FPGAs, PLLs, DACs and ADCs an error of more than 1 ns finally results if equal instrumental delays would be assumed. In addition, the signal amplitudes differ by up to 30%. This difference could be caused by slight bug-fixes on the BABs, each of which was made to make the prototype system functional. In the next revision of the BABs, this difference should no longer appear, but will be investigated again. Further, the second coupling for the setup from chapter 5 and the current prototype setup are compared. To achieve better comparability, both signals are normalised and shifted in time. Due to the pre-distorted Ricker wavelet, differences occur in the second couplings. The signal components caused by the connectors and balun overlap destructively and are less clearly visible than in the previous setup. This results in a clearer reflection of the antenna feed point and antenna pads. However, the arrival time of the antenna feed point reflection cannot be detected without a previous calibration.

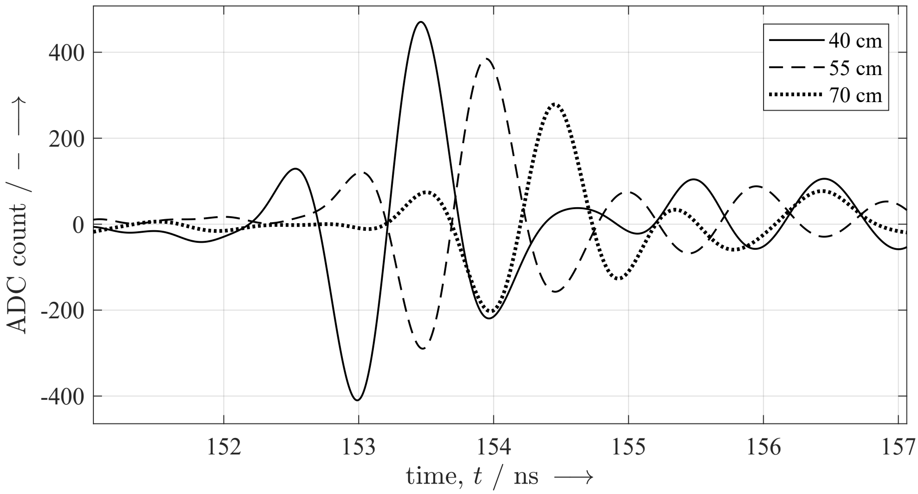

Figure 6.5: Three exemplary signals of a WARR measurement.

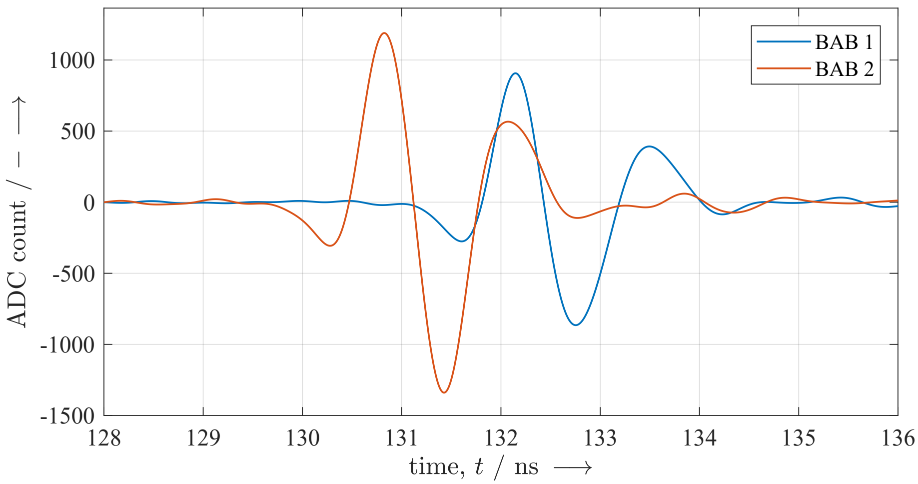

Figure 6.6: First coupling measured for channel 57 on both BABs.

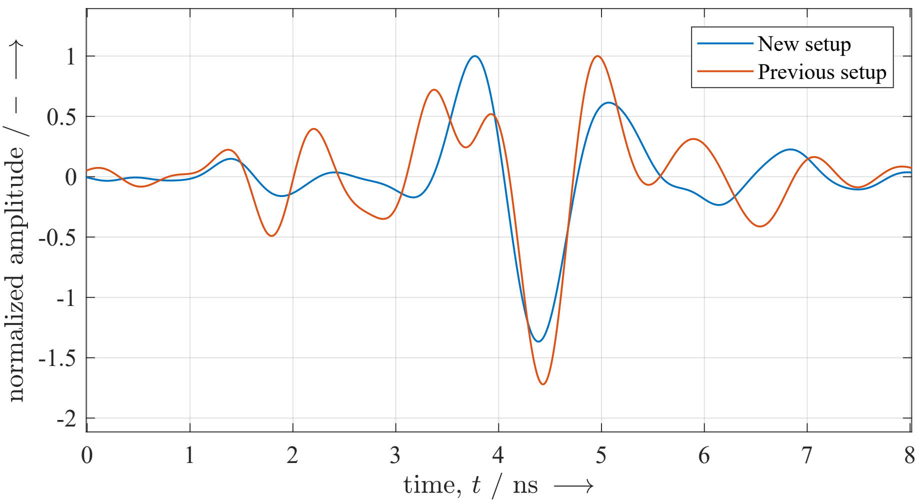

Figure 6.7: Comparsion of normalized second coupling for previous setup and prototype setup.

6.2.3 Time-zero estimation

Finally, the final time-zero accuracy is evaluated. First, a WARR measurement is performed to obtain a reference for time-zero. Time-zero is determined for the case that BAB 1 transmits and BAB 2 receives, as well as for the case that BAB 2 transmits and BAB 1 receives. From the reference WARR measurement it follows that

$$t_{0\,1\,2} = 142.173 \pm 0.012\ \text{ns}, \qquad R^2 = 0.9991$$
$$t_{0\,2\,1} = 142.209 \pm 0.017\ \text{ns}, \qquad R^2 = 0.9984\,.$$

The trigger lines between the trigger distribution, the MAM interfaces and the BABs are compensated in length. From the measurement of the internal reflections in section 6.2.2 it is already known that the instrumental delays per BAB, i.e., $t_{\text{Tx}\,\text{Rx}\,1}$ for BAB 1 and $t_{\text{Tx}\,\text{Rx}\,2}$ for BAB 2, can vary by more than one nanosecond (Fig. 6.6). Furthermore, the analysis of the repeated synchronization (Fig. 6.4) shows that the signal arrival times can vary by more than 3 ns.

Further, for the calibrated offsets for both time-zero measurements from (3.48), it follows that

$$t_{\text{offset}\,1} = 1.808 \pm 0.004\ \text{ns}$$
$$t_{\text{offset}\,2} = 1.808 \pm 0.006\ \text{ns}\,.$$

For both time-zero measurements, identical offsets result to identify the arrival time of the antenna feed point reflection in the second coupling. Thus, $t_{\mathrm{offset}} = 1.808$ ns is used for the further analyses. To further quantify the accuracy of the in situ calibration approach, four additional WARR measurements are performed and time-zero is determined for each WARR measurement and BAB. The time-zeros from the already described WARR measurement with $t_{0\,1\,2} = 142.173$ ns and $t_{0\,2\,1} = 142.209$ ns serve as a reference ($\mathrm{M_{ref}}$). The four additional WARR measurements were performed 19 hours (M1), 42 hours (M2), 45 hours (M3) and 76 hours (M4) after $\mathrm{M_{ref}}$. The CLKs of both BABs are synchronised once before $\mathrm{M_{ref}}$ and the CLKs are then left to run independently for M1 and M2. Before measurement M3 the CLKs are resynchronised and run independently again for the remaining two WARR measurements (M3, M4). This measurement procedure thus includes both the drifting of the CLKs over several days and larger timing changes due to the resynchronization. Both cases can also occur in the real system at the lysimeter. The in situ time-zero calibration must be able to correct for such changes in time-zero. The time-zeros determined by the in situ calibration are denoted by $\hat{t}_{0\,1\,2}$ and $\hat{t}_{0\,2\,1}$. The results are shown in Fig. 6.8. Shifted times are shown for all measurements, where all times are shifted by the reference time-zero from the WARR calibration, i.e., by $t_{0\,1\,2}$ when BAB 1 receives and by $t_{0\,2\,1}$ when BAB 2 receives. Absolute values of $t_{0\,1\,2}$ and $t_{0\,2\,1}$ are additionally given for each measurement. By shifting the times, the comparability of all measurements is simplified. For each of the five WARR measurements, the individual measurements at eight different antenna distances are considered and statistically evaluated. The blue cross in each boxplot indicates the reference time-zero determined by the WARR calibration, the red circle indicates the shifted time-zero determined by the in situ calibration, i.e., $\hat{t}_{0\,1\,2} - t_{0\,1\,2}$ for BAB 1 and $\hat{t}_{0\,2\,1} - t_{0\,2\,1}$ for BAB 2. The maximum difference between WARR calibrated and in situ calibrated time-zeros is 4 ps. For BAB 1, $t_{0\,1\,2}$ remains constant within 5 ps for the first three measurements $\mathrm{M_{ref}}$, M1 and M2. $t_{0\,2\,1}$ changes by 10 ps between $\mathrm{M_{ref}}$ and M2. After resynchronization, $t_{0\,1\,2}$ and $t_{0\,2\,1}$ change by 1.253 ns and 1.082 ns, respectively. For M3, the differences between $t_{0\,1\,2}$ and $t_{0\,2\,1}$ are larger with 207 ps. A closer look at M3 reveals that for both BABs the internal reflections are shifted in time, whereby the respective shift is different (1.358 ns for BAB 1, 0.970 ns for BAB 2). The main reason for the changing instrumental delays are PLLs that eventually require different numbers of clock cycles to stabilize the phase of the CLKs after a resynchronization. However, the changed time-zeros can be determined with an accuracy of 4 ps via the in situ calibration.

Finally, the standard calibration and the in situ calibration are further compared. For this purpose, the exact time-zeros are determined for all 80 individual measurements (eight per WARR measurement, five WARR measurements, two BABs) via $t_0 = t_{\mathrm{a}} - d/v$ and used as reference values. Then, for each individual measurement, time-zero is determined either via the WARR calibrated time-zero or from the in situ calibration and the respective residuals are analyzed (Fig. 6.9). For both calibration methods the maximum error is smaller than 25 ps. The in situ calibration results in a maximum error of 22 ps

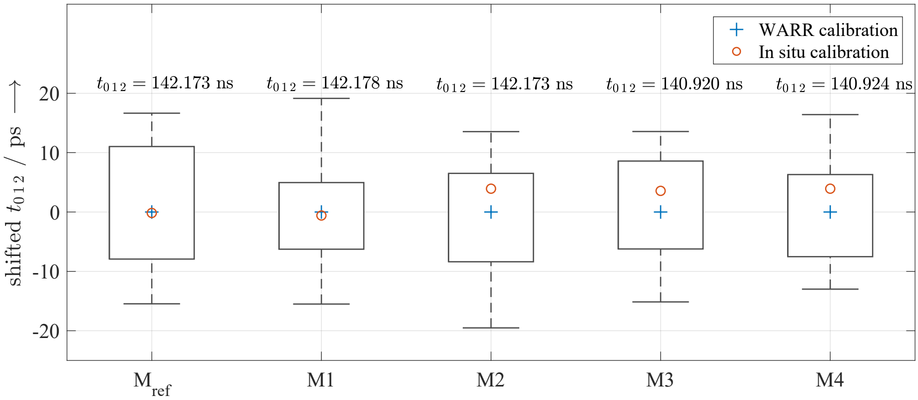

(a)

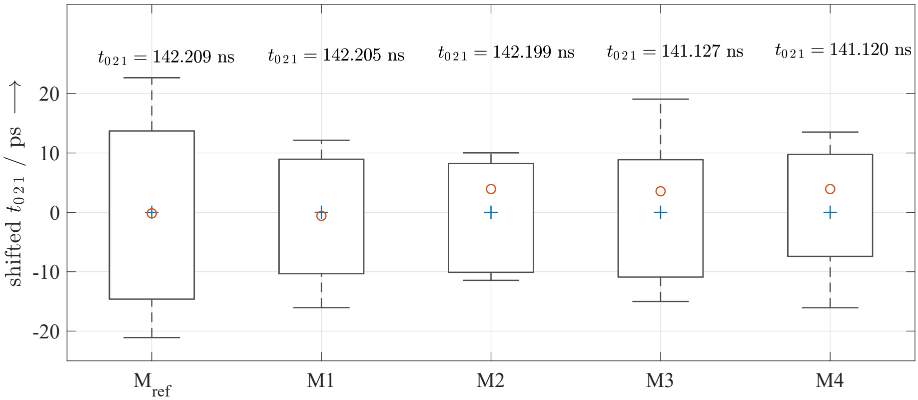

(b)

Figure 6.8: Standard calibration and in situ calibration for (a) BAB 1 and (b) BAB 2.

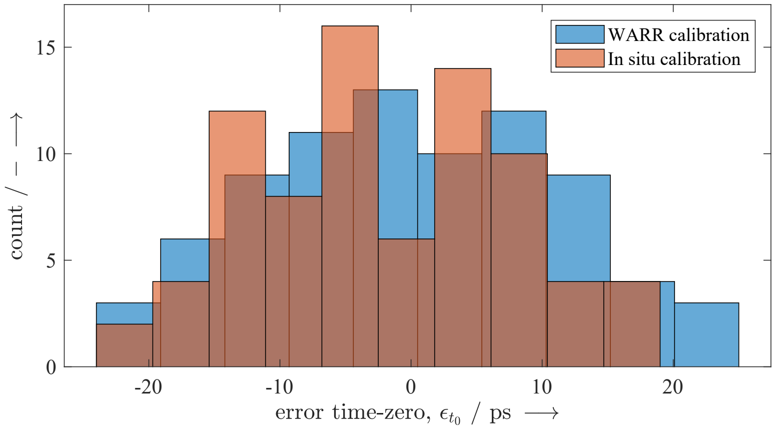

Figure 6.9: Errors for time-zero when using the standard WARR calibration and the novel in situ calibration.

and a standard deviation of ± 10 ps. The residuals of the WARR calibration approximate a normal distribution with its distribution center shifted by 4 ps compared to the in situ calibration. This may be due to the uniquely determined offset that is used for all measurements. An adaptive method for adjusting this offset during operation of the system is therefore recommended. This could be done, for example, by introducing the offset as a free parameter in the full-waveform inversion. If these 4 ps prove to be constant over further measurements, t_{offset} can be adjusted directly. Nevertheless, time-zero can be determined very accurately for all 80 individual measurements. The in situ calibration thus provides similarly accurate results as the WARR calibration, but does not require a known medium between the antennas.

6.3 Conclusions

In this chapter, the developed in situ calibration is evaluated using a prototype system. This prototype system contains all essential components of the planned final system, including synchronization and triggering of individual BABs. First, the temporal stability of the prototype system was investigated. A distinction is made between jitter, drift and phase ambiguities due to resynchronization. The jitter is low with about 25 ps for the Ricker wavelet and can be reduced by repeating measurements and averaging the data. In addition, it is shown that resynchronization can lead to changes in the timings of up to 4 ns that need to be corrected. These changes are caused by phase ambiguities within the RF PLLs. Resynchronization is performed every time the system is restarted. A direct comparison of standard calibration via WARR measurements and the developed in situ calibration shows that the accuracy of the in situ calibration is the same as for the standard method (± 11 ps for WARR calibration, ± 10 ps for in situ calibration). The higher accuracy of the in situ calibration potentially follows from the fact that the positioning accuracy of the antennas in the individual measurements has no influence on the calibration accuracy as in the WARR calibration. The differences between standard calibration and in situ calibration are limited to 4 ps for all measurements. For the in situ calibration, no known medium is required between the antennas, so that an accurate recalibration of the final GPR monitoring system is always guaranteed in operational use at the lysimeter.

Chapter 7

Summary and Outlook

7.1 Summary

The temporal calibration of ground penetrating radar (GPR) systems is essential for successful data processing and consequently for the investigation of soil processes. This is especially true for a newly developed multichannel GPR monitoring system with 2500 antennas for which standard calibration procedures cannot be used. Therefore, the aim of this work was to develop and analyse possible approaches for the temporal calibration of the GPR multichannel monitoring system. To derive the final calibration method, a simplified monitoring system was first considered, in which assumptions were made regarding the instrumental delays within the system. It was shown that the superposition of reciprocal measurements, termed as mesh calibration, leads to a significant reduction of measurement noise. Reciprocal measurements between all neighbouring antennas result in a normalised standard deviation of the noise that is consistently smaller than the standard deviation of a single measurement. With the largest possible mesh, which connects all channels via reciprocal measurements, the standard deviation can be reduced to such an extent that it has a negligible influence on the calibration. However, the same or known instrumental delays are assumed for all channels by the presented mesh calibration. By making assumptions regarding the signal coupling between neighbouring antennas, this assumption can be tested during operation, but any differences cannot be corrected.

For the more realistic tile GPR system, additional internal reflection measurements are introduced besides the reciprocal measurements. With these internal reflection measurements it is possible to resolve the requirement of equal instrumental delays for the calibration. This is important for the planned system, as the tile structure of the GPR system is planned with several antennas per digital-analog converter (DAC) and analog-digital converter (ADC) with different mircostrip lines and cables. In addition, the delay caused by phase-locked loops (PLLs) within the base boards (BABs) may vary after the system is switched on and off, requiring recalibration of the system. The internal reflection measurements are made possible by a small mismatch of the antenna impedances and limited isolation between the SP3T ports that are used to switch the antennas between Tx and Rx mode. For wide angle reflection and refraction (WARR) measurements in air between varying antenna channels, the in situ calibration via reciprocal and internal reflection measurements achieves an accuracy of ±16 ps in SP3T Tx mode and ±6 ps in Rx mode. All measurements were performed on an evaluation board that represents the analogue paths of the final GPR system consisting of switches, baluns and amplifiers. The evaluation board was supplemented with laboratory equipment for signal generation and data acquisition, in particular a vector network analyzer. Systematic errors due to the mounting of the antennas at the lysimeter and the positioning of the antennas in the array can be estimated in Tx mode with 21 ps. In general, the Tx mode proves to be more stable, as the internal reflections are less affected by changing external influences. In addition, the Tx mode has the advantage that the internal reflection measurements can be integrated into the actual tomography measurements of the soil by activating the respective ADC for measuring the internal reflections. This saves measurement time compared to measurements in Rx mode.

Finally, the in situ calibration was tested on a prototype system. The prototype system essentially consists of two operational BABs, which supplement the evaluation board from the previous experiments with the final DACs, ADCs, PLLs, synchronisation and triggering. Thus, the prototype system contains all essential components of the final system and can be used for the final evaluation of the in situ calibration. First, the temporal stability of the prototype system was evaluated based on jitter, temporal drifts and time jumps. While jitter and drift are negligible, time jumps of up to 3 ns are caused by the resynchronisation of the BABs, which are transferred to changes of time-zero. Furthermore, a series of five WARR measurements per BAB was performed to directly compare time-zero obtained from the standard calibration and the in situ calibration. The analysis of the errors for time-zero of all single measurements shows that the in situ calibration determines time-zero with a maximum error of 22 ps. At the same time, the corrected time-zeros have a bias of 4 ps and a standard deviation of ± 10 ps. For these measurements, the antennas were positioned neither at the lysimeter nor in the array. The systematic error of up to 21 ps from the measurements with the evaluation board can therefore also result for the prototype system, where the overall systematic error would be up to 25 ps.

7.2 Outlook

After showing in this work that the presented in situ calibration works within a prototype system comprised of the final hardware, the next step is to carry out measurements with the GPR monitoring system on soil samples with subsequent inversion of the measurement data. For comparison purposes, time-zero should be determined with classical methods via separate measurements and additionally via the presented in situ calibration and the resulting inversion results should be compared. The inversion can first be performed with raybased methods or directly with the suffisticated full-waveform inversion (FWI). If it turns out that the calibration must be performed more accurately, possibilities can be sought to determine exactly one instrumental Tx or Rx delay per BAB, since the superposition of reciprocal measurements between BABs can then be used to decrease errors introduced by random noise. In addition, extended temperature studies should be made to identify temperature dependencies. These are important because (i) different temperature profiles prevail on the BABs for the different channels and (ii) heating and cooling of the lysimeter itself could have an influence on the calibration and especially the internal reflection measurements.

Regarding the FWI, further possibilities exist to improve the calibration. It could be tested whether the offset of the reflected signals to be determined can be included in the inversion as a parameter to be optimised. The offset previously determined by measurements would then serve as the starting value. For the inversion, the offset must be identical for all measurements, which means that only one additional parameter is added to the inversion. This could reduce systematic errors observed for the measurements with the evaluation board and the prototype system. The same applies to the determination of the arrival times of the transmitted signals. Currently, manually determined shifts relative to characteristic points within the Ricker wavelet are still used. The FWI offers the potential that this shift can be taken as an additional parameter to be optimised. This way, the individual influence of the GPR operator on the inversion accuracy could be further reduced. The method for determining arrival times can also be further optimised. In this work, a new approach was presented via the calculation of the impulse response and symmetry properties. This approach should be tested with real tomography data. Especially the internal reflection measurements offer further application possibilities besides the use within the temporal calibration. For example, the source wavelet estimation, which is crucial for FWI, can use the internal reflections to find even better estimates for the source wavelet and optimise it for each individual antenna. Thus, an in situ amplitude calibration would also be performed. In addition, faulty antennas or antenna channels can be detected directly via the internal reflections and, if necessary, excluded from the inversion.

Also, the application of the presented in-situ calibration should be considered for other systems. In commercial systems, to the best of our knowledge, specific transmitters and receivers are used instead of switchable antennas. With a redesign and switchable antennas, borehole measurements, for example, could be carried out much faster, as no re-calibration would have to be carried out at frequent time intervals. GPR manufacturers should therefore consider whether a redesign towards transceivers with switchable antenna modes is worthwhile, as the calibration of the systems can be simplified significantly and improved compared to manual calibrations. This allows more measurement time for the actual soil investigations, while at the same time increasing the accuracy of the calibration.

Bibliography

[1] B. C. O'Neill et al. "The roads ahead: Narratives for shared socioeconomic pathways describing world futures in the 21st century". In: *Global Environmental Change* 42 (Jan. 2017), pp. 169–180. DOI: 10.1016/j.gloenvcha.2015.01.004.

[2] H. Valin et al. "The future of food demand: understanding differences in global economic models". In: *Agricultural Economics* 45.1 (Dec. 2013), pp. 51–67. DOI: 10.1111/agec.12089.

[3] B. L. Bodirsky et al. "The ongoing nutrition transition thwarts long-term targets for food security, public health and environmental protection". In: *Scientific Reports* 10.1 (Nov. 2020). DOI: 10.1038/s41598-020-75213-3.

[4] J. Fanzo, A. L. Bellows, M. L. Spiker, A. L. Thorne-Lyman, and M. W. Bloem. "The importance of food systems and the environment for nutrition". In: *The American Journal of Clinical Nutrition* 113.1 (Nov. 2020), pp. 7–16. DOI: 10.1093/ajcn/nqaa313.

[5] H. M. Jol. *Ground Penetrating Radar: Theory and Applications. theory and applications*. Ed. by H. Jol. ELSEVIER Science, Dec. 11, 2008, p. 524. ISBN: 978-0-444-53348-7.

[6] A. Klotzsche, F. Jonard, M. C. Looms, J. van der Kruk, and J. A. Huisman. "Measuring Soil Water Content with Ground Penetrating Radar: A Decade of Progress". In: *Vadose Zone Journal* 17.1 (2018). DOI: 10.2136/vzj2018.03.0052.

[7] J. L. Davis and A. P. Annan. "Ground-Penetrating Radar for high-resolution mapping of soil and rock stratigraphy". In: *Geophysical Prospecting* 37 (1989), pp. 531–551.

[8] J. A. Huisman, S. S. Hubbard, J. D. Redman, and A. P. Annan. "Measuring Soil Water Content with Ground Penetrating Radar: A Review". In: *Vadose Zone Journal* 2.4 (Nov. 2003), pp. 476–491. DOI: 10.2136/vzj2003.4760.

[9] C. Paz, F. J. Alcala, J. M. Carvalho, and L. Ribeiro. "Current uses of ground penetrating radar in groundwater-dependent ecosystems research". In: *Science of the Total Environment* 595 (Oct. 2017), pp. 868–885. DOI: 10.1016/j.scitotenv.2017.03.210.

[10] X. Liu, X. Dong, and D. I. Leskovar. "Ground penetrating radar for underground sensing in agriculture: a review". In: *International Agrophysics* 30.4 (Oct. 2016), pp. 533–543. DOI: 10.1515/intag-2016-0010.

[11] M. Yang, G. Wang, R. Lazin, X. Shen, and E. Anagnostou. “Impact of planting time soil moisture on cereal crop yield in the Upper Blue Nile Basin A novel insight towards agricultural water management”. In: *Agricultural Water Management* (2021).

[12] C. Riefolo, A. Belmonte, R. Quarto, F. Quarto, S. Ruggieri, and A. Castrignanò. “Potential of GPR data fusion with hyperspectral data for precision agriculture of the future”. In: *Computers and Electronics in Agriculture* 199 (Aug. 2022), p. 107109. DOI: 10.1016/j.compag.2022.107109.

[13] J. D. Bolten, W. T. Crow, X. Zhan, T. J. Jackson, and C. A. Reynolds. “Evaluating the Utility of Remotely Sensed SoilMoisture Retrievals for Operational AgriculturalDrought Monitoring”. In: *IEEE Journal of selected topics in applied earth observations and remote sensing* 3.1 (Mar. 1, 2010).

[14] D. D. Benedetto, F. Montemurro, and M. Diacono. “Mapping an Agricultural Field Experiment by Electromagnetic Induction and Ground Penetrating Radar to Improve Soil Water Content Estimation”. In: *Agronomy* 9.10 (Oct. 2019), p. 638. DOI: 10.3390/agronomy9100638.

[15] X. Xu, S. Peng, W. Xiao, and Y. Yu. “Measuring soil layer thickness in land rearrangement with GPR data”. In: *Measurement Science and Technology* 25.7 (May 2014), p. 075802. DOI: 10.1088/0957-0233/25/7/075802.

[16] M. Nakhkash and M. Mahmood-Zadeh. “Water leak detection using ground penetrating radar”. In: *Proceedings of the Tenth International Conference on Grounds Penetrating Radar, 2004. GPR 2004.* 2004.

[17] S.-Y. Hyun, Y.-S. Jo, H.-C. Oh, S.-Y. Kim, and Y.-S. Kim. “The laboratory scaled-down model of a ground-penetrating radar for leak detection of water pipes”. In: *Measurement Science and Technology* 18.9 (July 2007), pp. 2791–2799. DOI: 10.1088/0957-0233/18/9/008.

[18] A. D. Coster et al. “Towards an improvement of GPR-based detection of pipes and leaks in water distribution networks”. In: *Journal of Applied Geophysics* 162 (Mar. 2019), pp. 138–151. DOI: 10.1016/j.jappgeo.2019.02.001.

[19] H. Vereecken, J. W. Hopmans, A. Schnepf, and M. Javaux. “Modeling Soil Processes: Review, Key Challenges, and New Perspectives”. In: *Vadose Zone Journal* 15.5 (May 2016). DOI: 10.2136/vzj2015.09.0131.

[20] G. C. Topp, J. L. Davis, and A. P. Annan. “Electromagnetic Determination of Soil and Water Content: Measurements in Coaxial Transmission Lines”. In: *WATER RESOURCES RESEARCH* 16.3 (1980), pp. 574–582.

[21] K. Roth, R. Schulin, H. Flühler, and W. Attinger. “Calibration of time domain reflectometry for water content measurement using a composite dielectric approach”. In: *Water Resources Research* 26.10 (Oct. 1990), pp. 2267–2273. DOI: 10.1029/WR026i010p02267.

[22] M. Dobson, F. Ulaby, M. Hallikainen, and M. El-rayes. "Microwave Dielectric Behavior of Wet Soil-Part II: Dielectric Mixing Models". In: *IEEE Transactions on Geoscience and Remote Sensing* GE-23.1 (Jan. 1985), pp. 35–46. DOI: 10.1109/TGRS.1985.289498.

[23] F. Lavoué, R. Brossier, L. Métivier, S. Garambois, and J. Virieux. "Two-dimensional permittivity and conductivity imaging by full waveform inversion of multioffset GPR data: a frequency-domain quasi-Newton approach". In: *Geophysical Journal International* 197.1 (Jan. 2014), pp. 248–268. DOI: 10.1093/gji/ggt528.

[24] M. C. Looms et al. "Mapping sand layers in clayey till using crosshole ground-penetrating radar". In: *GEOPHYSICS* 83.1 (Jan. 2018), A21–A26. DOI: 10.1190/geo2017-0297.1.

[25] G. P. Tsoflias and M. W. Becker. "Ground-penetrating-radar response to fracture-fluid salinity: Why lower frequencies are favorable for resolving salinity changes". In: *GEOPHYSICS* 73.5 (Sept. 2008), J25–J30. DOI: 10.1190/1.2957893.

[26] T. Saarenketo and T. Scullion. "Road evaluation with ground penetrating radar". In: *Journal of Applied Geophysics* 43 (2000), pp. 119–138.

[27] D. S. Hammond, L. Chapman, and J. E. Thornes. "Parameterizing road construction in route-based road weather models: can ground-penetrating radar provide any answers?" In: *Measurement Science and Technology* 22.5 (Mar. 2011), p. 057001. DOI: 10.1088/0957-0233/22/5/057001.

[28] A. Ihamouten et al. "Full-waveform inversion using a stepped-frequency GPR to characterize the tack coat in hot-mix asphalt (HMA) layers of flexible pavements". In: *NDT and E International* 95 (2018), pp. 17–25.

[29] J. Hugenschmidt and R. Mastrangelo. "GPR inspection of concrete bridges". In: *Cement & Concrete Composites* 28 (2006), pp. 384–392.

[30] K. Dinh, N. Gucunski, and T. Zayed. "Automated visualization of concrete bridge deck condition from GPR data". In: *NDT & E International* 102 (Mar. 2019), pp. 120–128. DOI: 10.1016/j.ndteint.2018.11.015.

[31] L. B. Ciampoli, A. Calci, and F. D'Amico. "Railway Ballast Monitoring by GPR: A Test-Site Investigation". In: *MDPI remote sensing* (2019).

[32] I. Catapano, A. Affinito, L. Bertolla, J. L. Porsani, and F. Soldoviero. "Oil spill monitoring via microwave tomography enhanced GPR surveys". In: *Journal of Applied Geophysics* 108 (2014), pp. 95–103.

[33] Y. N. S. Wijewardana, A. T. Shilpadi, M. I. M. Mowjood, K. Kawamoto, and L. W. Galagedara. "Ground-penetrating radar (GPR) responses for sub-surface salt contamination and solid waste: modeling and controlled lysimeter studies". In: *Environment Monitoring Assess* 189.2 (Jan. 2017). DOI: 10.1007/s10661-017-5770-4.

[34] B. Sai and L. Ligthart. "GPR Phase-Based Techniques for Profiling Rough Surfaces and Detecting Small, Low-Contrast Landmines Under Flat Ground". In: *IEEE Transactions on Geosciense and Remote Sensing* 42.2 (Feb. 2, 2004), pp. 318–326. DOI: 10.1109/tgrs.2003.817204.

[35] S. Lameri, F. Lombardi, P. Bestagini, M. Lualdi, and S. Tubaro. "Landmine detection from GPR data using convolutional neural networks". In: *2017 25th European Signal Processing Conference (EUSIPCO)*. IEEE, Aug. 2017. DOI: 10.23919/EUSIPCO.2017.8081259.

[36] U. Wollschläger, H. Gerhards, Q. Yu, and K. Roth. "Multi-channel ground-penetrating radar to explore spatial variations in thaw depth and moisture content in the active layer of a permafrost site". In: *The Cryosphere* 4.3 (Aug. 2010), pp. 269–283. DOI: 10.5194/tc-4-269-2010.

[37] Y. Wang, Z. Fu, X. Lu, S. Qin, H. Wang, and X. Wang. "Imaging of the Internal Structure of Permafrost in the Tibetan Plateau Using Ground Penetrating Radar". In: *Electronics* 9.1 (Dec. 2019), p. 56. DOI: 10.3390/electronics9010056.

[38] J. Kunz and C. Kneisel. "Glacier–Permafrost Interaction at a Thrust Moraine Complex in the Glacier Forefield Muragl, Swiss Alps". In: *Geosciences* 10.6 (May 2020), p. 205. DOI: 10.3390/geosciences10060205.

[39] E. Forte, H. M. French, R. Raffi, I. Santin, and M. Guglielmin. "Investigations of polygonal patterned ground in continuous Antarctic permafrost by means of ground penetrating radar and electrical resistivity tomography: Some unexpected correlations". In: *Permafrost and Periglacial Processes* 33.3 (June 2022), pp. 226–240. DOI: 10.1002/ppp.2156.

[40] E. Slob, M. Sato, and G. Olhoeft. "Surface and borehole ground-penetrating-radar developments". In: *GEOPHYSICS* 75.5 (Sept. 2010), 75A103–75A120. DOI: 10.1190/1.3480619.

[41] K. Wu et al. "A new drone-borne GPR for soil moisture mapping". In: *Remote Sensing of Environment* 235 (Dec. 2019), p. 111456. DOI: 10.1016/j.rse.2019.111456.

[42] H. Liu, X. Xie, and M. Sato. "Accurate thickness estimation of a backfill grouting layer behind shield tunnel lining by CMP measurement using GPR". In: (June 2012). DOI: 10.1109/ICGPR.2012.6254848.

[43] X. Feng, M. Sato, Y. Zhang, C. Liu, F. Shi, and Y. Zhao. "CMP Antenna Array GPR and Signal-to-Clutter Ratio Improvement". In: *IEEE Geoscience and Remote Sensing Letters* 6.1 (Jan. 2009), pp. 23–27. DOI: 10.1109/LGRS.2008.2006634.

[44] N. Diamanti, E. J. Elliott, S. R. Jackson, and A. P. Annan. "The WARR Machine: System Design, Implementation and Data". In: *Journal of Environmental and Engineering Geophysics* 24.4 (4 Dec. 2018), pp. 469–487. DOI: 10.2113/JEEG23.4.469.

[45] M. Sato and R. Thierbach. "Analysis of a borehole radar in cross-hole mode". In: *IEEE Transactions on Geoscience and Remote Sensing* 29.6 (1991), pp. 899–904. DOI: 10.1109/36.101368.

[46] A. Binley, P. Winship, R. Middleton, M. Pokar, and J. West. "High-resolution characterization of vadose zone dynamics using cross-borehole radar". In: *Water Resources Research* 37.11 (Nov. 2001), pp. 2639–2652. DOI: 10.1029/2000WR000089.

[47] S. Liu, X. Wang, Q. Lu, H. Li, Y. Wang, and L. Deng. "Dam Leakage Detection by Borehole Radar: A Case-History Study". In: *Remote Sensing* 11.8 (Apr. 2019), p. 969. DOI: 10.3390/rs11080969.

[48] H. Qin, Z. Wang, Y. Tang, and T. Geng. "Analysis of Forward Model, Data Type, and Prior Information in Probabilistic Inversion of Crosshole GPR Data". In: *Remote Sensing* 13.2 (Jan. 2021), p. 215. DOI: 10.3390/rs13020215.

[49] A. Klotzsche, H. Vereecken, and J. van der Kruk. "Review of crosshole ground-penetrating radar full-waveform inversion of experimental data: Recent developments, challenges, and pitfalls". In: *GEOPHYSICS* 84.6 (Nov. 2019), H13–H28. DOI: 10.1190/geo2018-0597.1.

[50] A. Tarantola. "Inversion of seismic reflection data in the acoustic approximation". In: *GEOPHYSICS* 49.8 (Aug. 1984), pp. 1259–1266. DOI: 10.1190/1.1441754.

[51] J. R. Ernst, H. Maurer, A. G. Green, and K. Holliger. "Full-Waveform Inversion of Crosshole Radar Data Based on 2-D Finite-Difference Time-Domain Solutions of Maxwell's Equations". In: *IEEE Transactions on Geoscience and Remote Sensing* 45.9 (Sept. 2007), pp. 2807–2828. DOI: 10.1109/TGRS.2007.901048.

[52] G. A. Meles, J. van der Kruk, S. A. Greenhalgh, J. R. Ernst, H. Maurer, and A. G. Green. "A New Vector Waveform Inversion Algorithm for Simultaneous Updating of Conductivity and Permittivity Parameters From Combination Crosshole/Borehole-to-Surface GPR Data". In: *IEEE Transactions on Geoscience and Remote Sensing* 48.9 (Sept. 2010), pp. 3391–3407. DOI: 10.1109/TGRS.2010.2046670.

[53] A. Klotzsche, J. van der Kruk, G. A. Meles, J. Doetsch, H. Maurer, and N. Linde. "Full-waveform inversion of cross-hole ground-penetrating radar data to characterize a gravel aquifer close to the Thur River, Switzerland". In: *Near Surface Geophysics* 8.6 (Aug. 2010), pp. 635–649. DOI: 10.3997/1873-0604.2010054.

[54] A. Klotzsche, J. van der Kruk, N. Linde, J. Doetsch, and H. Vereecken. "3-D characterization of high-permeability zones in a gravel aquifer using 2-D crosshole GPR full-waveform inversion and waveguide detection". In: *Geophysical Journal International* 195.2 (Aug. 2013), pp. 932–944. DOI: 10.1093/gji/ggt275.

[55] N. Gueting et al. "High resolution aquifer characterization using crosshole GPR full-waveform tomography: Comparison with direct-push and tracer test data". In: *Water Resources Research* 53.1 (Jan. 2017), pp. 49–72. DOI: 10.1002/2016WR019498.

[56] Z. Zhou et al. "3D aquifer characterization of the Hermalle-sous-Argenteau test site using crosshole ground-penetrating radar amplitude analysis and full-waveform inversion". In: *GEOPHYSICS* 85.6 (Nov. 2020), H133–H148. DOI: 10.1190/geo2020-0067.1.

[57] N. J. Cassidy. "Ground Penetrating Radar Data Processing, Modelling and Analysis". In: *Ground Penetrating Radar Theory and Applications.* Elsevier, 2009. Chap. 2, pp. 141–176. DOI: 10.1016/B978-0-444-53348-7.00005-3.

[58] E. L. Babcock, A. P. Annan, and J. H. Bradford. "Cable Effects in Ground-Penetrating Radar Data and Implications for Quantitative Amplitude Measurements". In: *Journal of Environmental and Engineering Geophysics* 21.3 (Sept. 2016), pp. 99–104. DOI: 10.2113/JEEG21.3.99.

[59] G. R. Olhoeft. "Maximizing the information return from ground penetrating radar". In: *Journal of Applied Geophysics* 43.2-4 (Mar. 2000), pp. 175–187. DOI: 10.1016/s0926-9851(99)00057-9.

[60] T. G. Savelyev, A. G. Yarovoy, and L. P. Ligthart. "Weighted near-field focusing in an array-based GPR". In: *Radio Science* 43.4 (June 2008), n/a–n/a. DOI: 10.1029/2007RS003791.

[61] A. P. Annan. "Ground Penetrating Radar: Principles, Procedures & Applications". In: *Ground Penetrating Radar: Principles, Procedures & Applications.* Sensors & Software Incorporated, 2003. Chap. 1, p. 278. DOI: 10.1190/1.9781560801719.ch11.

[62] H. Gerhards, U. Wollschläger, Q. Yu, P. Schiwek, X. Pan, and K. Roth. "Continuous and simultaneous measurement of reflector depth and average soil-water content with multichannel ground-penetrating radar". In: *GEOPHYSICS* 73.4 (July 2008), J15–J23. DOI: 10.1190/1.2943669.

[63] R. Yelf. "Where is True Time Zero? 21-24 June 2004, Delft University of Technology, Delft, The Netherlands". In: *Proceedings of the Tenth International Conference on Ground Penetrating Radar; 21-24 June, 2004, Delft, The Netherlands.* IEEE, 2004. ISBN: 90-9017959-3.

[64] J. Schmalholz, H. Stoffregen, A. Kemna, and U. Yaramanci. "Imaging of Water Content Distributions inside a Lysimeter using GPR Tomography". In: *Vadose Zone Journal* 3.4 (Nov. 2004), pp. 1106–1115. DOI: 10.2113/3.4.1106.

[65] M. S. Kaufmann, A. Klotzsche, H. Vereecken, and J. van der Kruk. “Simultaneous multichannel multi-offset ground-penetrating radar measurements for soil characterization”. In: *Vadose Zone Journal* 19.1 (Jan. 2020). DOI: 10.1002/vzj2.20017.

[66] S. Radzevicius. “Least-squares curve fitting for velocity and time zero”. In: *2015 8th International Workshop on Advanced Ground Penetrating Radar (IWAGPR)*. IEEE, July 2015. DOI: 10.1109/IWAGPR.2015.7292677.

[67] K. Viriyametanont, S. Laurens, G. Klysz, J.-P. Balayssac, and G. Arliguie. “Radar survey of concrete elements: Effect of concrete properties on propagation velocity and time zero”. In: *NDT & E International* 41.3 (Apr. 2008), pp. 198–207. DOI: 10.1016/j.ndteint.2007.10.001.

[68] M. Oberröhrmann, A. Klotzsche, H. Vereecken, and J. van der Kruk. “Optimization of acquisition setup for cross-hole: GPR full-waveform inversion using checkerboard analysis”. In: *Near Surface Geophysics* 11.2 (Sept. 2012), pp. 197–209. DOI: 10.3997/1873-0604.2012045.

[69] I. Giannakis, F. Zhou, C. Warren, and A. Giannopoulos. “On the Limitations of Hyperbola Fitting for Estimating the Radius of Cylindrical Targets in Non-Destructive Testing and Utility Detection”. In: *IEEE Geoscience and Remote Sensing Letters* 19 (2022), pp. 1–5. DOI: 10.1109/LGRS.2022.3195947.

[70] D. Hoven, A. Mester, H. Vereecken, and A. Klotzsche. “Evaluation of starting model approaches and effective source wavelet variations for high-frequency GPR full-waveform inversion”. In: *GEOPHYSICS* 88.2 (Nov. 2022), pp. 1–65. DOI: 10.1190/geo2021-0683.1.

[71] H. Stoffregen, T. Zenker, and G. Wessolek. “Accuracy of soil water content measurements using ground penetrating radar: comparison of ground penetrating radar and lysimeter data”. In: *Journal of Hydrology* 267.3-4 (Oct. 2002), pp. 201–206. DOI: 10.1016/s0022-1694(02)00150-6.

[72] M. Hannes et al. “A comprehensive filtering scheme for high-resolution estimation of the water balance components from high-precision lysimeters”. In: *Hydrology and Earth System Sciences* 19.8 (Aug. 2015), pp. 3405–3418. DOI: 10.5194/hess-19-3405-2015.

[73] T. Pütz et al. “TERENO-SOILCan: a lysimeter-network in Germany observing soil processes and plant diversity influenced by climate change”. In: *Environmental Earth Sciences* 75.18 (Sept. 2016). DOI: 10.1007/s12665-016-6031-5.

[74] X. Xu, S. Peng, Y. Xia, and W. Ji. “The development of a multi-channel GPR system for roadbed damage detection”. In: *Microelectronics Journal* 45 (2014), pp. 1542–1555.

[75] A. Viberg, C. Gustafsson, and A. Andrén. “Multi-Channel Ground-Penetrating Radar Array Surveys of the Iron Age and Medieval Ringfort Bårby on the Island of Öland, Sweden”. In: *Remote Sensing* 12.2 (Jan. 2020), p. 227. DOI: 10.3390/rs12020227.

[76] M. Garcia-Fernandez, Y. A. Lopez, and F. L.-H. Andres. “Airborne Multi-Channel Ground Penetrating Radar for Improvised Explosive Devices and Landmine Detection”. In: *IEEE Access* 8 (2020), pp. 165927–165943. DOI: 10.1109/ACCESS.2020.3022624.

[77] J. P. Hoffman, D. Perkovic, S. Shaffer, L. Veilleux, and E. Peral. “Digital calibration of TR modules for real-time digital beamforming SweepSAR architectures”. In: *2012 IEEE Aerospace Conference*. IEEE, Mar. 2012. DOI: 10.1109/AERO.2012.6187084.

[78] M. Harter, J. Hildebrandt, A. Ziroff, and T. Zwick. “Self-Calibration of a 3-D-Digital Beamforming Radar System for Automotive Applications With Installation Behind Automotive Covers”. In: *IEEE Transactions on Microwave Theory and Techniques* 64.9 (Sept. 2016), pp. 2994–3000. DOI: 10.1109/tmtt.2016.2593731.

[79] D.-C. Kim, S.-J. Park, T.-W. Kim, L. Minz, and S.-O. Park. “Fully Digital Beamforming Receiver With a Real-Time Calibration for 5G Mobile Communication”. In: *IEEE Transactions on Antennas and Propagation* 67.6 (June 2019), pp. 3809–3819. DOI: 10.1109/TAP.2019.2902712.

[80] M. Jäger, R. Scheiber, and A. Reigber. “Robust, Model-Based External Calibration of Multi-Channel Airborne SAR Sensors Using Range Compressed Raw Data”. In: *Remote Sensing* 11.22 (Nov. 2019), p. 2674. DOI: 10.3390/rs11222674.

[81] H. M. Aumann, A. J. Fenn, and F. G. Willwerth. “Phased array antenna calibration and pattern prediction using mutual coupling measurements”. In: *IEEE Transactions on Antennas and Propagation* 37.7 (July 1989), pp. 844–850. DOI: 10.1109/8.29378.

[82] C. Shipley and D. Woods. “Mutual coupling-based calibration of phased array antennas”. In: *Proceedings 2000 IEEE International Conference on Phased Array Systems and Technology (Cat. No.00TH8510)*. IEEE, 2000. DOI: 10.1109/past.2000.859012.

[83] D. Bekers, R. van Dijk, and F. van Vliet. “Mutual-coupling based phased-array calibration: A robust and versatile approach”. In: *2013 IEEE International Symposium on Phased Array Systems and Technology*. IEEE, Oct. 2013. DOI: 10.1109/array.2013.6731903.

[84] D. Fleisch. *A Student’s Guide to Maxwell’s Equations*. Cambridge University Press, 2008, p. 144. ISBN: 9780521877619.

[85] K. Takahashi, J. Igel, H. Preetz, and S. Kuro. "Basics and Application of Ground-Penetrating Radar as a Tool for Monitoring Irrigation Process". In: *Problems, Perspectives and Challenges of Agricultural Water Management*. InTech, Mar. 2012. DOI: 10.5772/29324.

[86] M. Mansuripur and D. P. Tsai. "New perspective on the reciprocity theorem of classical electrodynamics". In: *Optics Communications* 284.3 (Feb. 2011), pp. 707–714. DOI: 10.1016/j.optcom.2010.09.077.

[87] R. Unbehauen. *Systemtheorie 1*. Oldenbourg, 2002, p. 583. ISBN: 978-3-486-25999-5.

[88] T. Westermann. *Mathematik für Ingenieure*. Springer Berlin Heidelberg, 2011. DOI: 10.1007/978-3-642-12760-1.

[89] H. Luke. "The origins of the sampling theorem". In: *IEEE Communications Magazine* 37.4 (Apr. 1999), pp. 106–108. DOI: 10.1109/35.755459.

[90] M. Skolnik. *Radar Handbook*. McGraw-Hill Education Ltd, Mar. 1, 2008. 1328 pp. ISBN: 978-0-07-148547-0. URL: https://www.ebook.de/de/product/6621098/m_skolnick_radar_handbook.html.

[91] Forschungszentrum Jülich. *The Plant Time Machine - Climate change meets soil research*. Online; accessed 11.08.2023. 2023. URL: https://www.fz-juelich.de/en/news/archive/feature-stories/the-plant-time-machine (visited on 08/11/2023).

[92] B. Xu and M. Noel. "On the completeness of data sets with multielectrode systems for electrical resistivity survey". In: *Geophysical Prospecting* 41.6 (Aug. 1993), pp. 791–801. DOI: 10.1111/j.1365-2478.1993.tb00885.x.

[93] C. C. Paige and M. A. Saunders. "LSQR: An Algorithm for Sparse Linear Equations and Sparse Least Squares". In: *ACM Transactions on Mathematical Software* 8.1 (Mar. 1982), pp. 43–71. DOI: 10.1145/355984.355989.

[94] A. Klotzsche, J. van der Kruk, J. Bradford, and H. Vereecken. "Detection of spatially limited high-porosity layers using crosshole GPR signal analysis and full-waveform inversion". In: *Water Resources Research* 50.8 (Aug. 2014), pp. 6966–6985. DOI: 10.1002/2013wr015177.

[95] B. Dafflon, J. Irving, and W. Barrash. "Inversion of multiple intersecting high-resolution crosshole GPR profiles for hydrological characterization at the Boise Hydrogeophysical Research Site". In: *Journal of Applied Geophysics* 73.4 (Apr. 2011), pp. 305–314. DOI: 10.1016/j.jappgeo.2011.02.001.

[96] K. Havas. "High resolution imaging of soilproperties inside a lysimeter usingGPR full-waveform inversion". MA thesis. IDEA League, Aug. 8, 2019.

[97] J. D. Irving, M. D. Knoll, and R. J. Knight. “Improving crosshole radar velocity tomograms: A new approach to incorporating high-angle traveltime data”. In: *GEOPHYSICS* 72.4 (July 2007), J31–J41. DOI: 10.1190/1.2742813.

[98] E. Ifeachor and B. Jervis. *Digital Signal Processing (2nd Edition)*. Prentice Hall, 2001, p. 933. ISBN: 978-0201596199.

[99] A. Mester et al. “Small broadband antennas for multi-channel GPR monitoring system”. In: *80. Jahrestagung der Deutschen Geophysikalischen Gesellschaft*. Mar. 25, 2020. URL: https://dgg2020.smart-abstract.com/sessionplanner/#/event/16786 (visited on 05/20/2021).

[100] J. D. Irving and R. J. Knight. “Effect of antennas on velocity estimates obtained from crosshole GPR data”. In: *GEOPHYSICS* 70.5 (Sept. 2005), K39–K42. DOI: 10.1190/1.2049349.

[101] A. Rumiantsev and N. Ridler. “VNA calibration”. In: *IEEE Microwave Magazine* 9.3 (June 2008), pp. 86–99. DOI: 10.1109/mmm.2008.919925.

[102] H. Liu et al. “Quantitative Stability Analysis of Ground Penetrating Radar Systems”. In: *IEEE Geoscience and Remote Sensing Letters* 15.4 (Apr. 2018), pp. 522–526. DOI: 10.1109/LGRS.2018.2801827.

[103] I. Bekman et al. “Clock synchronization for a multidevice data acquisition system of a ground penetrating radar”. In: *SEI Tagung 2023*. Apr. 17, 2023.

[104] L. Steinbeck, A. Mester, E. Zimmermann, A. Klotzsche, and S. van Waasen. “In situ time-zero correction for a ground penetrating radar monitoring system with 3000 antennas”. In: *Measurement Science and Technology* 33.7 (Apr. 2022), p. 075904. DOI: 10.1088/1361-6501/ac632b.

[105] L. Steinbeck, A. Mester, E. Zimmermann, A. Klotzsche, and S. van Waasen. “Calibration of a Stationary Multichannel GPR Monitoring System Using Internal Reflection Measurements”. In: *IEEE Transactions on Geoscience and Remote Sensing* 61 (2023), pp. 1–10. DOI: 10.1109/TGRS.2023.3275191.

[106] L. Steinbeck, A. Mester, S. Heinen, E. Zimmermann, A. Klotzsche, and S. van Waasen. “Calibration concept for a GPR monitoring system and methods for arrival time picking”. In: *2021 11th International Workshop on Advanced Ground Penetrating Radar (IWAGPR)*. IEEE, Dec. 2021. DOI: 10.1109/IWAGPR50767.2021.9843174.

[107] L. Steinbeck, A. Mester, E. Zimmermann, C. Roth, A. Klotzsche, and S. van Waasen. “Utilizing internal signal reflections for an in situ calibration of a GPR monitoring system”. In: *19th International Conference on Ground Penetrating Radar*. 2022.

[108] L. Steinbeck, A. Mester, C. Roth, E. Zimmermann, A. Klotzsche, and S. van Waasen. "Evaluation of Internal Signal Reflections for an in Situ Calibration of a Ground Penetrating Radar Monitoring System". In: *IGARSS 2022 - 2022 IEEE International Geoscience and Remote Sensing Symposium*. IEEE, July 2022. DOI: `10.1109/IGARSS46834.2022.9884631`.

[109] L. Steinbeck, A. Mester, E. Zimmermann, A. Klotzsche, and S. van Waasen. "In situ calibration concepts for stationary multichannel GPR monitoring systems". In: *83. Jahrestagung der Deutschen Geophysikalischen Gesellschaft*. 2023.

[110] L. Steinbeck, A. Mester, E. Zimmermann, and A. Klotzsche. *EP4113155 (A1) Verfahren zur zerstörungsfreien Untersuchung einer Probe mit einer Radar-, insbesondere Geo-Radar-Einrichtung, Radar-Einrichtung, Computerprogramm und Computerprogrammprodukt*. 2021.

Publications related to this work

Parts of this doctoral thesis have been published. The following list gives an overview of current publications in which parts of this doctoral thesis have been published.

Journal paper

L. Steinbeck, A. Mester, E. Zimmermann, A. Klotzsche, and S. van Waasen. "In situ time-zero correction for a ground penetrating radar monitoring system with 3000 antennas". In: *Measurement Science and Technology* 33.7 (Apr. 2022), p. 075904. DOI: 10.1088/1361-6501/ac632b

L. Steinbeck, A. Mester, E. Zimmermann, A. Klotzsche, and S. van Waasen. "Calibration of a Stationary Multichannel GPR Monitoring System Using Internal Reflection Measurements". In: *IEEE Transactions on Geoscience and Remote Sensing* 61 (2023), pp. 1–10. DOI: 10.1109/TGRS.2023.3275191

Conferences

A. Mester, L. Peters, L. Jokhovets, I. Flammia, A. Klotzsche, E. Zimmermann, J. van den Boom, J. A. Huisman, H. Vereecken, and S. van Waasen. "Small broadband antennas for multi-channel GPR monitoring system". In: *80. Jahrestagung der Deutschen Geophysikalischen Gesellschaft*. Mar. 25, 2020. URL: https://dgg2020.smart-abstract.com/sessionplanner/#/event/16786 (visited on 05/20/2021)

L. Steinbeck, A. Mester, S. Heinen, E. Zimmermann, A. Klotzsche, and S. van Waasen. "Calibration concept for a GPR monitoring system and methods for arrival time picking". In: *2021 11th International Workshop on Advanced Ground Penetrating Radar (IWAGPR)*. IEEE, Dec. 2021. DOI: 10.1109/IWAGPR50767.2021.9843174

L. Steinbeck, A. Mester, E. Zimmermann, C. Roth, A. Klotzsche, and S. van Waasen. "Utilizing internal signal reflections for an in situ calibration of a GPR monitoring system". In: *19th International Conference on Ground Penetrating Radar*. 2022

L. Steinbeck, A. Mester, C. Roth, E. Zimmermann, A. Klotzsche, and S. van Waasen.

"Evaluation of Internal Signal Reflections for an in Situ Calibration of a Ground Penetrating Radar Monitoring System". In: *IGARSS 2022 - 2022 IEEE International Geoscience and Remote Sensing Symposium.* IEEE, July 2022. DOI: 10.1109/IGARSS46834.2022.9884631

L. Steinbeck, A. Mester, E. Zimmermann, A. Klotzsche, and S. van Waasen. "In situ calibration concepts for stationary multichannel GPR monitoring systems". In: *83. Jahrestagung der Deutschen Geophysikalischen Gesellschaft.* 2023

Patent application

L. Steinbeck, A. Mester, E. Zimmermann, and A. Klotzsche. *EP4113155 (A1) Verfahren zur zerstörungsfreien Untersuchung einer Probe mit einer Radar-, insbesondere Geo-Radar-Einrichtung, Radar-Einrichtung, Computerprogramm und Computerprogrammprodukt.* 2021

Curriculum Vitae

Personal data

Name	Leon Steinbeck (born Peters)
Date of birth	01.05.1996 in Geilenkirchen
Nationality	German

Professional Experience

10/19-09/23	**Doctoral Researcher**, Central Institute of Engineering, Electronics and Analytics - Electronic Systems (ZEA-2), Forschungszentrum Jülich GmbH, Jülich, Germany
10/22-12/22	**Guest Researcher**, Microwave and Radar Institute, German Aerospace Center, Oberpfaffenhofen, Germany
09/17-08/19	**Scientific Assistant**, Central Institute of Engineering, Electronics and Analytics - Electronic Systems (ZEA-2), Forschungszentrum Jülich GmbH, Jülich, Germany
09/14-08/17	**Mathematical-technical Software Engineer**, Central Institute of Engineering, Electronics and Analytics - Electronic Systems (ZEA-2), Forschungszentrum Jülich GmbH, Jülich, Germany

Education

10/19-09/23	**Doctoral Student**, Faculty of Engineering, University Duisburg-Essen, Duisburg, Germany
10/17-08/19	**M.Sc. Technomathematics**, FH Aachen, Campus Jülich, Germany
09/14-09/17	**B.Sc. Scientific Programming**, FH Aachen, Campus Jülich, Germany

Band / Volume 625
On a multi-spectral method for measuring aerosol properties, suitable for operation on iagos passenger aircraft
P. Weber (2024), ca 123 pp
ISBN: 978-3-95806-746-2

Band / Volume 626
Modellierung der flächendifferenzierten Grundwasserneubildung für Schleswig-Holstein
Endbericht
I. McNamara, B. Tetzlaff, T. Wolters, F. Wendland (2024), 96 pp
ISBN: 978-3-95806-748-6

Band / Volume 627
Modeling orographic gravity waves from source to termination to improve parameterization schemes in climate models
S. Rhode (2024), xii, ii, 138 pp
ISBN: 978-3-95806-750-9

Band / Volume 628
Abscheidung kolumnarer Wärmedämmschichten mittels Suspensionsplasmaspritzen (SPS) und Plasma Spray – Physical Vapor Deposition (PS-PVD) Prozess
J. Joeris (2024), vii, 133 pp
ISBN: 978-3-95806-752-3

Band / Volume 629
Structure and properties of electrochemical interfaces from first principles simulations
R. Tesch (2024), xvi, 161 pp
ISBN: 978-3-95806-753-0

Band / Volume 630
Elucidation of Barocaloric Effect in Spin Crossover Compounds
H. Shahed (2024), x, 261 pp
ISBN: 978-3-95806-758-5

Band / Volume 631
Computational Investigation of Solvation Phenomena at Metal-Electrolyte Interfaces
O. Cheong (2024), xvii, 142 pp
ISBN: 978-3-95806-759-2

Band / Volume 632
Senkung zukünftiger Stickoxid- und Partikelemissionen in Nordrhein-Westfalen durch den Einsatz alternativer Energieträger und Antriebe
J. L. Breuer (2024), vii, 339 pp
ISBN: 978-3-95806-760-8

Band / Volume 633
Development of Model-Based Correction Methods for Temperature-Dependent Electromagnetic Induction (EMI) Measurement Errors in Soil Conductivity Estimations
T. M. Tchantcho Amin (2024), xx, 100 pp
ISBN: 978-3-95806-761-5

Band / Volume 634
Investigation and implementation of improved and degradation-tolerant fuel electrodes for solid oxide cells
A. Schwiers (2024), VI, 163, XIII pp
ISBN: 978-3-95806-762-2

Band / Volume 635
In Situ Time Calibration for Stationary Multichannel GPR Monitoring Systems
L. Steinbeck (2024), xvi, 98, xxxi pp
ISBN: 978-3-95806-767-7

Weitere ***Schriften des Verlags im Forschungszentrum Jülich*** unter
http://wwwzb1.fz-juelich.de/verlagextern1/index.asp

Energie & Umwelt / Energy & Environment
Band / Volume 635
ISBN 978-3-95806-767-7

Mitglied der Helmholtz-Gemeinschaft

JÜLICH
Forschungszentrum